

Fourier spectral computation of geometrically confined two-dimensional flows

Citation for published version (APA):

Keetels, G. H. (2008). *Fourier spectral computation of geometrically confined two-dimensional flows*. [Phd Thesis 1 (Research TU/e / Graduation TU/e), Applied Physics and Science Education]. Technische Universiteit Eindhoven. <https://doi.org/10.6100/IR634990>

DOI:

[10.6100/IR634990](https://doi.org/10.6100/IR634990)

Document status and date:

Published: 01/01/2008

Document Version:

Publisher's PDF, also known as Version of Record (includes final page, issue and volume numbers)

Please check the document version of this publication:

- A submitted manuscript is the version of the article upon submission and before peer-review. There can be important differences between the submitted version and the official published version of record. People interested in the research are advised to contact the author for the final version of the publication, or visit the DOI to the publisher's website.
- The final author version and the galley proof are versions of the publication after peer review.
- The final published version features the final layout of the paper including the volume, issue and page numbers.

[Link to publication](#)

General rights

Copyright and moral rights for the publications made accessible in the public portal are retained by the authors and/or other copyright owners and it is a condition of accessing publications that users recognise and abide by the legal requirements associated with these rights.

- Users may download and print one copy of any publication from the public portal for the purpose of private study or research.
- You may not further distribute the material or use it for any profit-making activity or commercial gain
- You may freely distribute the URL identifying the publication in the public portal.

If the publication is distributed under the terms of Article 25fa of the Dutch Copyright Act, indicated by the "Taverne" license above, please follow below link for the End User Agreement:

www.tue.nl/taverne

Take down policy

If you believe that this document breaches copyright please contact us at:

openaccess@tue.nl

providing details and we will investigate your claim.

FOURIER SPECTRAL COMPUTATION OF
GEOMETRICALLY CONFINED
TWO-DIMENSIONAL FLOWS

Copyright © 2008 G.H. Keetels
Cover design by Paul Verspaget Grafische Vormgeving-Communicatie
Printed by Universiteitsdrukkerij TU Eindhoven, Eindhoven, The Netherlands

CIP-DATA LIBRARY TECHNISCHE UNIVERSITEIT EINDHOVEN

Keetels, Gerardus Hubertus

Fourier spectral computation of geometrically confined two-dimensional flows /
by Gerardus Hubertus Keetels. – Eindhoven: Technische Universiteit Eindhoven,
2008. – Proefschrift.

ISBN 978-90-386-1278-2

NUR 928

Trefwoorden: turbulentie / turbulente stromingen / vloeistofwervels / grenslagen/
wandeffecten / numerieke simulaties

Subject headings: 2D turbulence / confined flow / computational fluid dynamics
/ spectral methods / immersed boundary methods / wall effects / boundary layers

FOURIER SPECTRAL COMPUTATION
OF GEOMETRICALLY CONFINED
TWO-DIMENSIONAL FLOWS

PROEFSCHRIFT

ter verkrijging van de graad van doctor aan de
Technische Universiteit Eindhoven, op gezag van de
Rector Magnificus, prof.dr.ir. C.J. van Duijn, voor een
commissie aangewezen door het College voor
Promoties in het openbaar te verdedigen
op dinsdag 3 juni 2008 om 16.00 uur

door

Gerardus Hubertus Keetels

geboren te Waalwijk

Dit proefschrift is goedgekeurd door de promotoren:

prof.dr. H.J.H. Clercx

en

prof.dr.ir. G.J.F. van Heijst

This project has been funded by the Dutch Foundation
for Fundamental Research on Matter (FOM).



To my grandparents

Contents

1	The no-slip boundary: a source of vorticity	9
1.1	Mathematical formulation	9
1.1.1	Equations of motion for 2D flows	9
1.1.2	Integral quantities	11
1.2	KBL scaling	14
1.3	Vorticity production at no-slip walls	18
1.4	Vortex-wall interaction	21
1.4.1	Dipole-wall collision	23
1.5	Alternative scaling relations for boundary-layer vorticity	27
1.5.1	Alternative scaling model	27
1.5.2	Validation	29
1.5.3	Finite pressure assumption	30
2	Numerical method	33
2.1	Introduction	33
2.2	Volume-penalization	35
2.2.1	The model equation	35
2.2.2	Convergence and regularity	36
2.3	Numerical methods	37
2.3.1	Fourier-Galerkin with an explicit treatment of Darcy drag	37
2.3.2	Fourier collocation with an implicit treatment of Darcy drag	39
2.3.3	Coherent vortex simulation	41
2.3.4	Chebyshev spectral methods	43
2.4	Recovery of higher-order accuracy of Fourier schemes	44
3	Convergence study of a normal dipole-wall collision	47
3.1	Dipole-wall collision benchmark computation	48
3.1.1	Setup and initial condition	48
3.1.2	Chebyshev-Fourier and Chebyshev benchmark computations	49
3.2	Convergence analysis of Fourier schemes	50
3.2.1	Gibbs oscillations	51
3.2.2	Truncation error	52

3.2.3	Long-time integrations and global quantities	55
3.3	Convergence analysis of Coherent Vortex Simulation (CVS)	56
3.3.1	Visualization	56
3.3.2	Grid adaptation	58
3.3.3	Error analysis	60
3.3.4	Penalization parameter and reduction of wavelet coefficients	62
3.4	Penalization error	63
3.5	Conclusions and discussion	65
4	Convergence study of an oblique dipole-wall collision	69
4.1	Geometry error	69
4.2	Oblique dipole-wall collisions	72
4.3	Conclusion and discussion	74
5	Quasi-stationary states in a circular geometry	77
5.1	Statistical mechanics and the minimum-entropy principle	77
5.2	Setup of the simulations	80
5.3	Initialization without angular momentum	81
5.4	Initialization with angular momentum	85
5.5	Metastable minimum-entropy branch	87
5.A	Appendix: Selective decay	91
5.B	Appendix: Minimum-entropy principle on a circular domain	95
6	Spin-up in an elliptic geometry	105
6.1	Introduction	105
6.2	Angular momentum production	106
6.3	Numerical method	108
6.4	Decaying 2D turbulence in elliptic geometries	110
6.5	Conclusion	115
6.A	Appendix: angular momentum in an elliptic geometry	116
7	Spin-up at high Reynolds numbers in a square geometry	121
7.1	Introduction	121
7.2	Setup of the simulations	122
7.3	Confined 2D decaying turbulence	123
7.4	Appendix: a note on the characteristic time-scale	131
8	Forced 2D turbulence on a bounded domain	133
8.1	Setup of the simulations	134
8.2	Statistically steady state	135
8.3	Structure functions and self-similarity	138
8.4	Second-order moments	139
8.5	Intermittency and extended self-similarity	141
8.6	Enstrophy transfer	144

CONTENTS	3
9 Conclusions and prospects	147
Summary	158
Dankwoord	163
Curriculum Vitae	165

Introduction

Two-dimensional turbulence?

The term “two-dimensional (2D) turbulence” seems to be in conflict with our daily experience with turbulent flow phenomena, which obviously evolve in all three spatial directions. Like for example the smoke plumes emerging from a chimney on a windy day, the distribution of sugar in a cup of tea or the flow in the wake of a truck on the highway. The evening news presents, on the other hand, satellite images that show cloud formations and associated flow patterns that are extended on a horizontal length scale of thousands of kilometers. The characteristic vertical length scales of these flows are, however, orders of magnitude smaller typically a few kilometers. This implies a strong geometrical confinement, as a matter of fact, a single page of this thesis is already too thick to illustrate the aspect-ratio of the atmospheric fluid layer. As a consequence vertical velocities are strongly suppressed. Also the flows in the oceans exhibit strong geometrical confinement. Additional mechanisms can further suppress vertical motion in large-scale geophysical flows. Both the atmosphere and ocean have on average a stable density stratification where dense fluid is situated near the bottom with lighter fluid layers on top of it. This means that if a heavy fluid parcel moves up into a layer with smaller density it will experience a net downward force whereas a light fluid parcel that moves downwards will be pushed upwards by the denser fluid. A third mechanism is related to the rotation of the earth. According to the Taylor-Proudman theorem the velocity in a rotating system becomes independent of the axial coordinate (parallel to the rotation vector). Due to the absence of vertical velocities at the surface this results in a horizontal orientation of the velocity without variation in the vertical direction *i.e.* a column-like organization of the flow.

Two-dimensional turbulence may be seen as a conceptual model to describe large-scale geophysical flows. The net effect of essentially 3D flow phenomena is then represented by a simplified approach. For example, the complicated interaction with the surface of the earth or seabed is modelled by a simple friction term. Also large-scale baroclinic instabilities or small-scale convective systems that could drive large scale atmospheric flow may be incorporated by simple forcing protocols. Obviously this approach has a lot of limitations, especially for forecasting purposes.

On the other hand, the 2D approach with parametrization is useful to understand certain flow phenomena in either a qualitative or a statistical sense. See for example the analysis of Lindborg [64] who verified that it is possible to explain statistical correlation between certain length scales in the atmosphere by a two-dimensional turbulence approach. Another geophysical example is the study of Humi [42] on the Antarctic boundary layer. It was observed that 2D flow develops in different independent layers due to an extremely stable density stratification. The zonal band structure observed in the atmosphere of the planet Jupiter can also be explained by a 2D approach with a linear variation in the background rotation known as the β -plane approximation.

Also in the oceans there are convincing manifestations of two-dimensional flow. It is well-known that many vortex-like structures emerge due to interaction of the currents with the continental shelves. See for example the work of Goni *et al.* [34] on the formation of Algulhas rings near Cape of Good Hope. Another manifestation of bounded two-dimensional turbulence in geophysical flows is the formation of vortex arrays in the Gulf of Aden or the Adriatic Sea [29]. Similar vortex arrays are found in laboratory experiments in stably stratified fluids confined in rectangular tanks and in 2D decaying turbulence simulations in a rectangular domain with no-slip walls, see Maassen *et al.* [67]. In the context of geophysical flows the no-slip boundary condition can be seen as a simplified boundary condition for a large-scale (2D) model.

The phenomenology between 2D and 3D turbulence is strikingly different. In 3D flows eddies tend to break up into smaller eddies. At the smallest scales of motion the kinetic energy of the eddies will be dissipated by the action of viscous forces. This process, first recognized by Richardson in 1922, has become known as the “direct energy cascade” of 3D turbulence. Important theoretical effort on the statistical characterization of the direct energy cascade is assembled in a series of classical papers written by Kolmogorov in 1941. A complete deductive theory of turbulent flow based on first principles is still missing. However, by adopting a number of phenomenological assumptions about the isotropy, spatial homogeneity, similarity of spatial scaling and the energy dissipation rate of the flow, Kolmogorov succeeded to postulate a heuristic theory for 3D turbulence, that successfully predicts the values of several statistical objects in 3D turbulence.

Later Kraichnan, Batchelor and Leith (KBL) applied a similar phenomenological approach to 2D turbulence. It was predicted that if kinetic energy is injected on the small scales in two-dimensional flows it is transported towards the largest scales of motion. This is called the “inverse energy cascade” to mark the difference with the direct energy cascade of 3D turbulence. Furthermore, KBL-theory predicts that a another cascade can co-exist with the inverse energy cascade. This cascade is known as the “direct enstrophy cascade“ of 2D turbulence. It transfers the enstrophy, which is a measure of the total amount of vorticity of the flow, from the large scales towards the smallest scales of motion where viscous dissipation dominates. Many numerical and experimental techniques have been employed to test the sta-

tistical scaling of the inverse energy cascade and direct enstrophy cascade proposed by KBL. The first direct numerical simulation (DNS) of forced 2D turbulence was performed by Lilly [63] in order to verify the simultaneous existence of both cascades. His simulations are performed on a periodic square domain, which means that all the values of the flow variables at the boundary of the domain should be equal to the values at the opposite boundary. This specific setup is chosen such that Fourier spectral methods could be applied, which allows a very accurate representation of the flow variables. Furthermore, it was believed that flow in a periodic box is a reliable representation of flow on an infinitely extended domain such that finite-size effects and additional complications due to the presence of solid boundaries are avoided. His results confirmed the KBL-picture but the numerical resolution in those days was relatively poor. Only very recently Boffetta [11] conducted a high-resolution computation that convincingly showed that both cascades can exist simultaneously. It is interesting to note that both Lilly [63] and Boffetta [11] used the Fourier spectral technique. There has been an enormous increase in available computer resources in the time span between both studies. The number of Fourier modes employed by Lilly was 64^2 modes whereas Boffetta used a luxurious number of 16384^2 Fourier modes.

The KBL-scaling arguments are often compared with data obtained from various experiments, in soap films [12, 49, 90], thin fluid layers [84, 102, 103], homogeneously stratified fluids or two-layer fluids [65–67], and in rotating containers (see the review by Hopfinger and van Heijst [41]). This comparison is, however, not straightforward since in all these experiments the flow actually behaves quasi-2D, although most reports hardly address this issue. Furthermore, all the experiments involve solid (lateral) boundaries. In particular, the presence of lateral domain boundaries can dramatically change the evolution of both forced and decaying 2D flows [16, 20, 40, 67, 72].

It is interesting to mention that the ITER fusion chamber, which is being developed in Cadarache, France, can also be seen as a quasi-2D turbulence “experiment”. Inside the toroidal chamber of a fusion reactor the motion of the plasma perpendicular to the magnetic field lines becomes quasi-2D as a result of the Lorentz force. Akin the role of the Coriolis force in the suppression of the variation of the velocity in the axial direction the Lorentz force tends to remove the variation of the velocity along the magnetic field lines, which results in planer-like motion of the plasma. An important drawback to make a fusion device operational is the heat loss at the side-walls of the chamber, which results in a strong erosion of the wall plates. This thesis does not concern magnetohydrodynamics (MHD), nevertheless a thorough understanding of the effect of walls on fluid turbulence might be useful to acquire understanding of wall-bounded MHD problems, as well.

In the geophysical context a study on the effect of lateral side-walls on 2D turbulence is important to gain understanding of large-scale turbulent flows in the oceans, which are bounded by the continental shelves.

Outline

In this thesis the effects of no-slip boundaries on 2D turbulence are studied in different geometries. In Chapter 1 the 2D turbulence concept will be specified in further detail. The role of no-slip boundaries on the production of vorticity will be examined by considering previously reported results on individual dipole-wall collision problems. In Chapter 2 several numerical schemes are formulated to solve the 2D Navier-Stokes equations with no-slip boundary conditions. We mainly focus on the Fourier spectral schemes combined with an immersed boundary technique, since this approach is used throughout the thesis. Chapter 3 and 4 concern the validation of the numerical method by means of challenging benchmark problems. In Chapter 5 the end-states of decaying 2D turbulence in a circular geometry are considered. Chapter 6 contains a study on the influence of the shape of the geometry on the spontaneous production of angular momentum. In Chapter 7 it is analyzed whether the spin-up phenomenon is confined to a particular range of Reynolds number or is also of crucial importance for the development of significantly higher Reynolds number flow. The small-scale vorticity statistics in the bulk of bounded 2D flow is studied in Chapter 8.

Chapter 1

The no-slip boundary: a source of vorticity

1.1 Mathematical formulation

1.1.1 Equations of motion for 2D flows

Consider an incompressible fluid of density ρ , in a domain $\Omega \in \mathbb{R}^2$, which evolves according to the Navier-Stokes equations

$$\partial_t \mathbf{u} + (\mathbf{u} \cdot \nabla) \mathbf{u} + \frac{1}{\rho} \nabla p - \nu \Delta \mathbf{u} = \frac{1}{\rho} \mathbf{f} \quad \text{in} \quad \Omega \times [0, T] \quad (1.1)$$

and the continuity condition

$$\nabla \cdot \mathbf{u} = 0 \quad \text{in} \quad \Omega \times [0, T], \quad (1.2)$$

where $\mathbf{u} = (u(\mathbf{x}, t), v(\mathbf{x}, t))$ is the Eulerian velocity, $p = p(\mathbf{x}, t)$ the scalar kinetic pressure, ν the kinematic viscosity and $\mathbf{f} = \mathbf{f}(\mathbf{x}, t)$ denotes the amount of external force per unit area. The complexity of the flow is controlled by the Reynolds number $\text{Re} = UW/\nu$, where U represents a typical velocity and W a typical length scale. The Reynolds number is a measure of the relative strength of the convective versus the viscous terms. The flow domain in this thesis is bounded by a steady impermeable wall, which implies that the velocity component normal to the wall equals zero. Furthermore, it is assumed that at the steady side walls the tangential velocity component vanish due to frictional effects between the viscous fluid and the wall. The combination of these boundary conditions on each component of the velocity defines the *no-slip* boundary condition, which read for a steady geometry,

$$\mathbf{u}(\mathbf{x}, t) = 0 \quad \mathbf{x} \in \partial\Omega, \quad t \in [0, T], \quad (1.3)$$

which is essentially a Dirichlet boundary condition for \mathbf{u} . Note that Eq. (1.1) contains second-order derivatives, so two boundary conditions are required for the

existence of a unique solution.

On a square bounded geometry

$$\mathcal{D} = \{ \mathbf{x} \in \mathbb{R}^2 \mid -W \leq x \leq W, -W \leq y \leq W \},$$

it is also possible to define *periodic boundary* conditions, which means that the value of the solution at the boundary $x = -W$ equals the value at the boundary $x = W$. The same periodicity holds for the boundaries at $y = W$ and $y = -W$. The formulation is completed by appending the initial condition

$$\mathbf{u}(\mathbf{x}, 0) = 0 \quad \mathbf{x} \in \Omega. \quad (1.4)$$

For convenience the Navier-Stokes equations in velocity-pressure or primitive variables (1.1) can be rewritten in velocity-vorticity formulation by taking the curl of Eq. (1.1) and applying some vector identities to arrive at

$$\partial_t \omega + (\mathbf{u} \cdot \nabla) \omega - \nu \Delta \omega = q \quad \text{in} \quad \Omega \times [0, T], \quad (1.5)$$

where

$$\omega = (\nabla \times \mathbf{u}) \cdot \mathbf{e}_z = \partial_x v - \partial_y u \quad (1.6)$$

is the scalar vorticity and

$$q = \frac{1}{\rho} (\nabla \times \mathbf{f}) \cdot \mathbf{e}_z,$$

is the z -component of the curl of the external forcing. Note that the velocity-vorticity formulation is scalar-valued in two dimensions. The boundary conditions on $\partial\Omega$ for the velocity-vorticity formulation are defined in terms of the velocity since no physical boundary condition is *a priori* available in terms of the vorticity. Note that it is of course possible to obtain the value of the vorticity at the boundary for a given velocity field by considering the vorticity definition (1.6) at the boundary.

In some cases it is also convenient, by virtue of the continuity condition (1.2), to introduce a stream function ψ according to

$$u = \partial_y \psi, \quad v = -\partial_x \psi.$$

The vorticity and stream function are then related by a Poisson equation,

$$\omega = -\nabla^2 \psi \quad \text{in} \quad \Omega. \quad (1.7)$$

The velocity-vorticity equation (1.5) can now be written as

$$\partial_t \omega + J(\omega, \psi) - \nu \Delta \omega = q \quad \text{in} \quad \Omega \times [0, T], \quad (1.8)$$

where $J(\omega, \psi)$ denotes the Jacobian,

$$J(f, g) = \partial_x f \partial_y g - \partial_x g \partial_y f.$$

To solve (1.8) the boundary conditions have to be formulated in terms of the stream function. Appropriate boundary conditions for the stream function are also required to solve the Poisson problem (1.7), such that the vorticity and stream function are uniquely related. An impermeable boundary can be modelled by taking a constant value for the stream function at the boundary, for convenience

$$\psi = 0 \quad \mathbf{x} \in \partial\Omega, \quad t \in [0, T].$$

A no-slip boundary where also the velocity component tangential to the domain boundary is zero yields a Neumann condition for the stream function,

$$\partial_{\mathbf{n}}\psi = 0 \quad \mathbf{x} \in \partial\Omega, \quad t \in [0, T],$$

where $\partial_{\mathbf{n}}$ denotes the derivative perpendicular to the boundary, $\partial_{\mathbf{n}} = (\mathbf{n} \cdot \nabla)$. It is still an unsolved problem to determine an unique and regular solution to Navier-Stokes initial-boundary value problem. The existence of the solutions in both 2D and 3D has only be shown in a weak sense. This means that the Navier-Stokes equations (1.1) and the continuity condition (1.2) only hold in terms of the moment against an infinitely differentiable and solenoidal set of functions *i.e.* the solution is not determined in a point-wise sense. For a precise definition of the weak solutions belonging to the Navier-Stokes equations one can consult *e.g.* Galdi [33]. In particular for the 2D Navier-Stokes problem it is shown that a weak solution is uniquely defined within a certain functional class. Furthermore, it has as much space-time regularity as allowed by the initial condition, see also Carbou and Fabrie [14]. For 3D flow only partial space-time regularity results have been obtained so far.

1.1.2 Integral quantities

Important aspects of two-dimensional turbulence in a confined domain with no-slip boundaries can be recovered by studying integral quantities. The first quantity is the total kinetic energy per unit density defined as

$$E = \frac{1}{2} \int_{\Omega} |\mathbf{u}|^2 dA = \frac{1}{2} \|\mathbf{u}\|_2^2 \quad (1.9)$$

where $\|g\|_2 = (g, g)^{1/2}$ denotes the L_2 -norm. The evolution equation for $E(t)$ can straightforwardly be derived by considering the Navier-Stokes equations in either velocity-pressure or velocity-vorticity form and reads,

$$\frac{dE}{dt} = (\mathbf{f}, \mathbf{u}) - 2\nu Z \quad (1.10)$$

where $(\mathbf{f}, \mathbf{u}) = \int_{\Omega} \mathbf{f} \cdot \mathbf{u} dA$ and Z denotes the total enstrophy of the flow,

$$Z = \frac{1}{2} \|\omega\|_2^2. \quad (1.11)$$

By considering the Navier-Stokes equations in velocity-vorticity formulation it can be derived that the enstrophy evolves according to,

$$\frac{dZ}{dt} = \nu \oint_{\partial\Omega} \omega(\mathbf{n} \cdot \nabla)\omega ds - 2\nu P + (\omega, q) = T_1 + T_2 + T_3, \quad (1.12)$$

where P denotes the total palinstrophy of the flow defined as

$$P = \frac{1}{2} \|\nabla\omega\|_2^2. \quad (1.13)$$

The term T_1 demonstrates that enstrophy can be produced at no-slip boundaries. This is a crucial difference compared with flow in a square periodic box, where T_1 is essentially zero. The other term T_2 represents the dissipation of enstrophy and is present in the case of periodic boundaries as well. The last term T_3 describes the production of enstrophy by the external forcing. For inviscid flow the energy and enstrophy are conserved quantities. It is often conjectured that the simultaneous conservation of energy and enstrophy for inviscid unforced $2D$ flows explains the dramatic contrast between $2D$ and $3D$ flows. Note, however, that viscous flow in the limit of $\nu \rightarrow 0$ not necessarily recovers inviscid dynamics with $\nu = 0$.

It is seen in Eq. (1.12) that the palinstrophy can be related to the dissipation of enstrophy. Therefore, it is necessary to derive the evolution equation for the palinstrophy. Differentiation of the Navier-Stokes equations in the velocity-vorticity formulation yields an equation for the rate of change of the spatial gradients of the vorticity,

$$\frac{D}{Dt} \left[\frac{\partial\omega}{\partial x_i} \right] = -\frac{\partial u_j}{\partial x_i} \frac{\partial\omega}{\partial x_j} + \nu \frac{\partial^2}{\partial x_j^2} \left(\frac{\partial\omega}{\partial x_i} \right) + \frac{\partial q}{\partial x_i} \quad (1.14)$$

where for convenience the index notation is applied for the vectors $\mathbf{u} = (u_1, u_2)$ and $\mathbf{x} = (x_1, x_2)$. The evolution equation of the palinstrophy is then readily obtained,

$$\frac{dP}{dt} = R_1 + R_2 + R_3 + R_4 \quad (1.15)$$

where

$$\begin{aligned} R_1 &= -\left(\frac{\partial u_j}{\partial x_i} \frac{\partial\omega}{\partial x_j}, \frac{\partial\omega}{\partial x_i} \right), \\ R_2 &= \nu \oint_{\partial\Omega} \nabla\omega \cdot (\mathbf{n} \cdot \nabla)\nabla\omega ds, \\ R_3 &= -\nu \left(\frac{\partial^2\omega}{\partial x_i \partial x_j}, \frac{\partial^2\omega}{\partial x_i \partial x_j} \right), \\ R_4 &= \left(\frac{\partial q}{\partial x_i}, \frac{\partial\omega}{\partial x_i} \right). \end{aligned}$$

The term R_1 represents the rate of amplification of vorticity gradients. This process is considered as the physical mechanism of the direct enstrophy cascade, which transfers vorticity towards the smallest scales of motion. By reverting the indices i, j it is straightforward to show that R_1 can be expressed in terms of the rate of strain tensor $\mathbf{S} = \frac{1}{2}(\nabla\mathbf{u} + \nabla\mathbf{u}^t) = \frac{1}{2}(\frac{\partial u_i}{\partial x_j} + \frac{\partial u_j}{\partial x_i})$, yielding,

$$R_1 = \left(S_{ij}, \frac{\partial\omega}{\partial x_i} \frac{\partial\omega}{\partial x_j} \right). \quad (1.16)$$

This demonstrates that it is essentially alignment between the rate of strain tensor and the vorticity gradients that can result in a non-linear production of palinstrophy. If the production of palinstrophy by non-linear dynamics is proportional to the Reynolds number it can result in a non-vanishing dissipation term T_2 in the enstrophy balance (1.12). This observation is the key element of the fundamental scaling arguments of the enstrophy inertial range proposed by Batchelor [5]. The term R_2 in Eq. (1.15), which is absent for periodic boundaries, describes the production of palinstrophy at the domain boundaries. The term R_3 represents the dissipation of palinstrophy in the bulk of the flow due to viscous dissipation. Palinstrophy production due to interaction with the external forcing is described by the term R_4 .

An important quantity for fluids on a bounded domain is the angular momentum with respect to the center of the Cartesian coordinate frame for convenience denoted by $\mathbf{r} = (x, y)$.

$$L = \int_{\Omega} (\mathbf{r} \times \mathbf{u}) \cdot \mathbf{e}_z dA = \int_{\Omega} (xv - yu) dA. \quad (1.17)$$

By inserting the Navier-Stokes equations in velocity-pressure form into the definition of the angular momentum it is obtained that,

$$\frac{dL}{dt} = \frac{1}{\rho} \oint_{\partial\Omega} p \mathbf{r} \cdot d\mathbf{s} + \nu \oint_{\partial\Omega} \omega (\mathbf{r} \cdot \mathbf{n}) ds. \quad (1.18)$$

Since the angular momentum can be rewritten in terms of the vorticity,

$$L = -\frac{1}{2} \int_{\Omega} r^2 \omega dA,$$

it is also possible to derive the alternative expression by using the vorticity equation,

$$\frac{dL}{dt} = -\frac{1}{2} \nu \oint_{\partial\Omega} r^2 (\mathbf{n} \cdot \nabla \omega) ds + \nu \oint_{\partial\Omega} \omega (\mathbf{r} \cdot \mathbf{n}) ds. \quad (1.19)$$

It can be deduced that the first terms on the right-hand side of (1.18) and (1.19) have to balance since the second term on the right-hand side of both expressions is identical. A natural assumption is that the pressure at the boundary will reach a finite value in the limit of infinite Reynolds numbers. This implies that the product $\nu \frac{\partial\omega}{\partial n}$ should be finite as well for vanishing viscosity.

1.2 KBL scaling

First the scaling for 3D turbulence proposed by Kolmogorov will be discussed very briefly, followed by a more extended introduction of the scaling theory for 2D turbulence which was formulated in the spirit of the pioneering work of Kolmogorov, by Kraichnan, Batchelor and Leith (KBL) [5, 52, 58] around 1970.

In Kolmogorov theory it is conjectured that 3D flow contains a finite length scale l_d proportional to $(\nu^3/\mathcal{E})^{1/4}$ where \mathcal{E} is the kinetic energy dissipation. For large length scales it is assumed that viscous dissipation is negligible compared with the non-linear transfer rates of energy towards smaller scales. It is convenient to consider turbulence in terms of wave numbers instead of length scales. This is achieved by performing a Fourier transform, which can be defined in a periodic box in dimension d (with $d = 2$ or 3),

$$\mathbf{u}(\mathbf{x}, t) = \sum_{\mathbf{k}} \hat{\mathbf{u}}_{\mathbf{k}}(t) \exp(i\mathbf{k} \cdot \mathbf{x}), \quad \text{with} \quad \mathbf{k} \in \frac{\pi}{W} \mathbb{Z}^d$$

where W denotes the half-width of a periodic box in \mathbb{R}^d . The continuous Fourier expansion coefficients $\hat{\mathbf{u}}_{\mathbf{k}}(t)$ are defined as,

$$\hat{\mathbf{u}}_{\mathbf{k}}(t) = \frac{1}{(2W)^d} \int \mathbf{u}(\mathbf{x}, t) \exp(-i\mathbf{k} \cdot \mathbf{x}) d\mathbf{x}. \quad (1.20)$$

The amount of energy between wave numbers k and $k + dk$ equals $E(k)dk$, where $E(k)$ is the energy spectrum

$$E(k) = \frac{W}{\pi} \sum_{k < |\mathbf{k}| < k+dk} |\hat{\mathbf{u}}_{\mathbf{k}}|^2. \quad (1.21)$$

Note that the dimension of the energy spectrum is $[E(k)] = m^3/s^2$ whereas the dimension of the energy transfer rate is $[\mathcal{E}] = m^2/s^3$, since it represents the transfer of kinetic energy between the wave number bands.

Kolmogorov assumed that the energy spectrum in the inertial range is completely determined by the transfer rate of kinetic energy and the wave number. It is further assumed that all the kinetic energy is dissipated at high wave numbers $k > k_d$ with $k_d = 2\pi/l_d$. On dimensional grounds it can then be derived that the energy spectrum in the inertial range scales according to,

$$E(k) = C_0 \mathcal{E}^{2/3} k^{-5/3} \quad \text{for} \quad k_f < k < k_d \quad (1.22)$$

where C_0 represents the Kolmogorov constant.

Later Kraichnan, Batchelor and Leith [5, 52, 58] applied a similar phenomenological approach to 2D turbulence. Based on the observation that the non-linear terms conserve energy and enstrophy simultaneously, see Eqs. (1.10) and (1.12), it was suggested to consider both the non-linear transfer rate of energy \mathcal{E} and enstrophy χ . On dimensional grounds the transfer rates can be related according to

$$\chi = C_1 k^2 \mathcal{E}. \quad (1.23)$$

The concept of Kolmogorov is that the transfer of energy across a length scale in the inertial range does not depend on the wave number. To fulfill that both the enstrophy and energy transfers are wave number independent the constant C_1 in (1.23) should be zero. Kraichnan [52] conjectured that if it is assumed that the energy and enstrophy are injected at a certain wave number k_f an inverse energy cascade develops that transfers energy towards large scales. In the inverse energy cascade it is assumed that the transfer of enstrophy is negligible and the spectrum is determined by the energy transfer \mathcal{E} and wave number k . On dimensional grounds the spectrum becomes

$$E(k) = C_2 \mathcal{E}^{2/3} k^{-5/3} \quad \text{for} \quad k < k_f, \quad (1.24)$$

where C_2 is the Kraichnan-Kolmogorov constant. Simultaneously, a direct cascade of enstrophy develops where the energy transfer is negligible and the spectrum can be scaled with the down-scale enstrophy transfer rate χ

$$E(k) = C_3 \chi^{2/3} k^{-3} \quad \text{for} \quad k_f < k < k_d, \quad (1.25)$$

where k_d represents the wave number that corresponds with the smallest scales of motion $l_d \propto (\nu^3/\chi)^{1/6}$. A schematic representation of the dual cascade picture is given in Fig. 1.1. The energy transfers towards progressively larger scales or lower wave numbers, whereas the enstrophy transfers down-scale or to higher wave numbers until viscous dissipation becomes dominant. Batchelor [5] proposed a similar

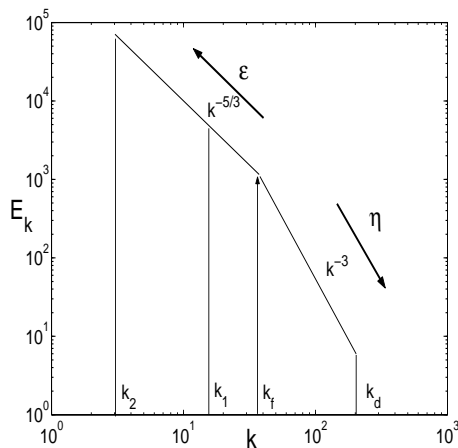


Figure 1.1 – Schematic representation of an inverse energy cascade for $k < k_f$ and a direct enstrophy cascade in the range $k_f < k < k_d$, k_1 is the lowest wave number at time t_1 and k_2 it the lowest wave number at time t_2 with $t_2 > t_1$.

scaling for the energy spectrum at high wave numbers for the case of freely evolving or decaying turbulence.

At this point we have to be more specific about the definition of the energy and enstrophy transfer rates. For forced flow we have to consider ensemble averages for example of the form,

$$\langle g(\mathbf{u}) \rangle = \int g(\mathbf{u}) d\mu(\mathbf{u}) \quad (1.26)$$

where $\mu(\mathbf{u})$ denotes the probability measure of \mathbf{u} . Usually it is tactically assumed that it is legitimate to adopt the dynamical system concept of ergodicity such that ensemble averages can be replaced by time averages

$$\lim_{T \rightarrow \infty} \frac{1}{T} \int_0^T f(\mathbf{u}) dt = \langle f(\mathbf{u}) \rangle. \quad (1.27)$$

To achieve a statistically steady state on a periodic domain it can be derived from Eq. (1.10) that the energy input of the forcing has to balance the viscous dissipation, thus $\langle (\mathbf{f}, \mathbf{u}) \rangle = 2\nu \langle Z \rangle$. It is believed, however, that viscous forces in the inverse energy cascade are not able to balance the energy input by the forcing in general [9]. Therefore, the theoretical model of Kraichnan [52] can only be applied on infinitely extended domains. It is then assumed that the part of the spectrum between the forcing wave number and the lowest excited wave number is statistically stationary *e.g.* the spectrum as shown in Fig 1.1 between $k_1 < k < k_f$ becomes steady for $t > t_1$, whereas the range $k_2 < k < k_f$ becomes steady for $t > t_2$ etc.

It was already conjectured by Kraichnan [52] that on a finite domain the energy piles up in the lowest available mode. As a consequence, a completely different equilibrium solution will emerge. To prevent this condensation state it is common practice in the study of forced 2D turbulence in a periodic box to apply additional friction terms on the largest scales. It is then assumed that the non-linear transfer of energy up-scale is balanced by the dissipation of kinetic energy due to the presence of friction.

Time-averaging of the enstrophy balance (1.12) yields that

$$\lim_{\nu \rightarrow 0} \frac{1}{A} \langle (\omega, q) \rangle = \frac{2\nu}{A} \langle P \rangle = -\chi, \quad (1.28)$$

where A denotes the area of the flow domain. Recall that the boundary integral terms in Eq. (1.12) are absent since the KBL theory is developed on an infinite extended 2D plane. The interpretation of the latter limit is that the enstrophy injected by the forcing is transferred with a rate χ towards the smallest scales of motion where the enstrophy is dissipated by viscous forces.

For the case of decaying turbulence Batchelor [5] considered the inviscid limit for a fixed time t_c ,

$$\lim_{\nu \rightarrow 0} \frac{1}{A} \left\langle \frac{dZ}{dt} \right\rangle = -\frac{2\nu}{A} \langle P \rangle = \chi \quad \text{for} \quad 0 < t_c < \infty, \quad (1.29)$$

where $\langle \cdot \rangle$ denotes ensemble averages with a time dependent probability measure. Recently discussion about the existence of this limit is revived by Tran and Dritschel [105] who suggest that in the limit of $\nu \rightarrow 0$ the enstrophy dissipation will vanish. If their argument is valid it would imply that a direct cascade of enstrophy in freely evolving 2D turbulence vanishes for infinite Reynolds numbers. Note that in numerical studies always a finite value for the viscosity is employed. Therefore, the observation of the enstrophy cascade in numerical studies on decaying turbulence are not in conflict with their argument. It is anticipated that future high-resolution simulations may be necessary to examine this limit in further detail.

The shape of the energy spectrum in the energy cascade range is confirmed by many numerical and experimental studies on forced 2D turbulence. The conclusion of various studies on the enstrophy cascade range strongly vary with the type of large-scale friction that is applied to enforce a steady state. Furthermore, in many studies on the direct enstrophy cascade the Laplacian is replaced by higher-order harmonic operators or hyperviscosity to extend the range of wave numbers of the cascade. Also the resolution is an important issue as early numerical simulations indicated steeper spectra, whereas more recent studies with higher resolution show a better agreement with the KBL picture. Nam *et al.* [77] have shown that due to the presence of a drag force steeper spectra can be expected in the enstrophy cascade range. Recently, Boffetta [11] confirmed the dual cascade picture by performing very high resolution computations. A steady state in the latter study is achieved by applying linear bottom friction and the usual Laplacian is considered such that artificial dissipation mechanisms are completely avoided. It was observed that the spectrum in the enstrophy cascade range was steeper than k^{-3} as predicted by Nam *et al.* [77] for forced 2D flow with bottom friction. Boffetta [11] concludes, however, that a k^{-3} spectrum in 2D turbulence could be achieved by taking simultaneously the limits $L/l_f \rightarrow \infty$ and $l_f/l_d \rightarrow \infty$, where L denotes the largest scale, l_f represents the forcing scale and l_d the dissipation length scale. In Chapter 8 forced turbulence in a square domain with no-slip boundaries will be examined. Note that the difference with a periodic boundary is that vorticity can be produced at the walls, which can result in enhanced dissipation of the energy. It is anticipated that on a domain with no-slip boundaries it is possible to reach a balance between the energy input of the forcing and viscous dissipation, thus $\langle (\mathbf{f}, \mathbf{u}) \rangle = 2\nu \langle Z \rangle$. This implies that the use of additional friction terms is not necessary to achieve a steady state. Therefore, it is challenging to measure the small-scale vorticity statistics and test the KBL-scaling hypothesis in the bulk of wall bounded 2D turbulence (see Chapter 8).

1.3 Vorticity production at no-slip walls

No-slip boundaries can strongly affect 2D turbulence due to their role as sources of vorticity, see van Heijst *et al.* [40] for an overview. As a result of vorticity production the flow becomes to a certain degree inhomogeneous and anisotropic, such that the key assumptions of the KBL scaling theory may be violated. Furthermore, it has been observed in decaying 2D turbulence that the vorticity injection from the no-slip boundaries can result in a secondary forcing length scale that is proportional to the boundary-layer thickness [22].

To reveal the mechanism of vorticity production at a no-slip wall Morton [76] has studied the exact solutions of various Stokes problems. A similar approach is developed in this section. First the exact solutions of two viscous diffusion problems are studied that may serve as analogies for more complicated flow-wall interaction problems. Heuristic scaling arguments can be extracted from the viscous solutions, which may be helpful to clarify some scaling issues on the energy, enstrophy, palinstrophy and the corresponding derivatives in 2D turbulence confined by no-slip sidewalls.

First we study the production of vorticity in the upper half plane above a horizontal flat plate. From the x -component of the Navier-Stokes equations in velocity-pressure form (1.1) an expression can be derived for the flux of vorticity into the upper half-plane,

$$-\nu \frac{\partial \omega}{\partial y} = \frac{1}{\rho} \frac{\partial p}{\partial x} + \frac{d\tilde{u}}{dt} \quad \text{for} \quad y = 0, t \in [0, \infty) \quad (1.30)$$

where \tilde{u} denotes the velocity of the plate. Eq. (1.30) shows that the flux of enstrophy into the upper half-plane is generated by a pressure gradient along the plate and the acceleration of the plate. Since the pressure gradient along the boundary and the acceleration of the plate have the same effect on the vorticity production a simple problem will be examined. Consider an oscillating plate that generates a horizontal velocity profile u on the upper half-plane $y \geq 0$. The amplitude of the oscillating plate is denoted by V and the frequency by $\omega_p = 2\pi/T_p$ with T_p the period of the oscillation. Only the diffusive part of the x -component of the Navier-Stokes equations in velocity-pressure form (1.1) will be considered. It is assumed that there are no pressure differences in the horizontal direction, thus $\frac{\partial p}{\partial x} = 0$. This yields a diffusion problem of the form,

$$\frac{\partial u}{\partial t} = \nu \frac{\partial^2 u}{\partial y^2} \quad \text{for} \quad y \geq 0, t \in [0, \infty) \quad (1.31)$$

with the boundary condition at $y = 0$

$$u = V \cos(\omega_p t) \quad \text{for} \quad t \in [0, \infty). \quad (1.32)$$

It is further assumed that for $y \rightarrow \infty$ the velocity tends to zero, $u \rightarrow 0$. A time-periodic solution to this problem can be found by considering a solution

of the form

$$\frac{u}{V} = \mathcal{R}[g(y)\exp(i\omega_p t)], \quad (1.33)$$

where \mathcal{R} denotes the real part and $g(y)$ a complex amplitude. By mere substitution and implementation of the boundary condition at $y = 0$ one readily obtains,

$$\frac{u}{V} = \exp(-y/\delta_p) \cos(\omega_p t - \frac{y}{\delta_p}) \quad (1.34)$$

where $\delta_p = \sqrt{2\nu/\omega_p}$ represents the Stokes boundary-layer thickness. Straightforward calculation yields the following expressions for the integral quantities and the corresponding time derivatives,

$$\begin{aligned} \omega|_{\partial\Omega} &\propto \frac{V}{\delta_p} && \propto \frac{V}{T_p^{1/2}\nu^{1/2}}, \\ \partial_n \omega|_{\partial\Omega} &\propto \frac{V}{\delta_p^2} && \propto \frac{V}{T_p\nu}, \\ Z &\propto \frac{DV^2}{\delta_p} && \propto \frac{DV^2}{T_p^{1/2}\nu^{1/2}}, \\ P &\propto \frac{DV^2}{\delta_p^3} && \propto \frac{DV^2}{T_p^{3/2}\nu^{3/2}}, \\ \frac{dE}{dt} &\propto D\omega_p V^2 \delta_p && \propto \frac{DV^2\nu^{1/2}}{T_p^{1/2}}, \\ \text{Power} &\propto D\omega_p V^2 \delta_p && \propto \frac{DV^2\nu^{1/2}}{T_p^{1/2}}, \\ \frac{dZ}{dt} &\propto \frac{D\omega_p V^2}{\delta_p} && \propto \frac{DV^2}{T_p^{3/2}\nu^{1/2}}, \end{aligned} \quad (1.35)$$

where the integrations are performed on a rectangular section with a horizontal width D on the upper half-plane. Using these scaling relations it is found that the terms T_1 and T_2 in the enstrophy balance (1.12) show equivalent scaling behaviour. Note that there is a balance between the power delivered by the plate and the dissipation of the total kinetic energy. Recall that the decay of energy is associated with the total enstrophy of the flow, see Eq. (1.10).

The oscillating plate problem is defined on the upper half-plane. In order to verify if a similar vorticity profile develops in a bounded geometry, with consequent scaling behaviour of the integral quantities, the oscillating plate problem is translated to the unit circle \mathcal{C} . The diffusion equation on the unit circle becomes

$$\frac{\partial u_\phi}{\partial t} = \nu \left[\frac{\partial^2 u_\phi}{\partial r^2} + \frac{1}{r} \frac{\partial u_\phi}{\partial r} - \frac{u_\phi}{r^2} \right] \quad \text{for} \quad \mathcal{C} \times [0, \infty), \quad (1.36)$$

with u_ϕ the angular velocity. This equation is accompanied with the boundary condition for $r = 1$,

$$u_\phi = V_\phi \cos(\omega_p t) \quad \text{for} \quad t \in [0, \infty), \quad (1.37)$$

where V_ϕ represents the amplitude of the angular velocity at the boundary. A similar solution strategy as for the oscillating plate yields,

$$\frac{u_\phi}{V_\phi} = \mathcal{R} \left[\frac{J_1(\delta_p^{-1}(1+i)r)}{J_1(\delta_p^{-1}(1+i))} \exp\left(i \frac{t}{T_p}\right) \right] \quad (1.38)$$

where J_1 denotes the first order Bessel function of the first kind. The solution is displayed in Fig. 1.2. It shows that a very steep velocity profile appears that falls off exponentially towards the center of the circle. This behaviour is very similar to the solution of the flat oscillating plate. The thickness of the boundary layer is also proportional to δ_p . The difference is that for $r \rightarrow 0$ the velocity essentially vanishes, whereas the instantaneous velocity profile of the oscillating plate solution has an infinite number of oscillations around the line $u = 0$ when moving into the upper half-plane. It is possible to derive the same scaling relations as assembled in Eq. (1.35), which signifies that the boundedness of the flow does not affect the validity of the proposed scaling argument.

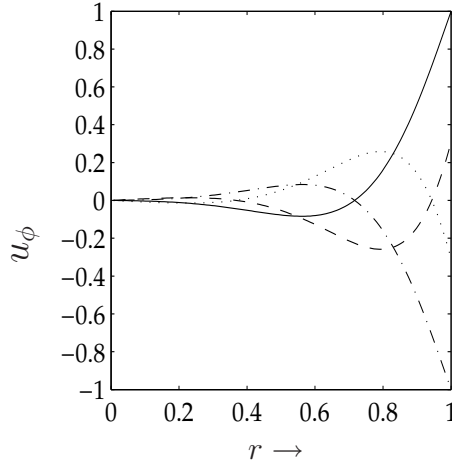


Figure 1.2 – Illustration of the angular velocity u_ϕ versus the radial coordinate r in an oscillating circle. The oscillation period $T_p = 1$, the amplitude $V_\phi = 1$, the kinematic viscosity $\nu = 0.1$ and the radius of the circle $r = 1$. Different times are shown $t = 0$ (solid), $t = 0.2$ (dashed), $t = 0.5$ (dashed-dot) and $t = 0.7$ (dot).

1.4 Vortex-wall interaction

A very characteristic process in both decaying and forced 2D turbulence is the spontaneous development of coherent vortices. In case of a bounded domain with lateral no-slip walls these vortices can collide with the solid boundaries. During such violent events high-amplitude vorticity filaments are generated and subsequently injected into the bulk of the flow. Furthermore, the forces that are exerted on the domain boundaries during individual vortex-wall collisions can result in a net torque on the sidewalls of the container. This can result in a growth of the angular momentum of the flow.

Considering the important role of vortices in bounded turbulence it is helpful to address the interaction of vortices with solid boundaries in some detail. Furthermore, it is anticipated that scaling relations of the integral quantities that are obtained for vortex-wall problems can be extended towards fully developed 2D turbulence [23].

Vortex-induced flow near a no-slip boundary

Several studies have been performed on the boundary layer at a no-slip wall affected by single vortices. Peridier *et al.* [85, 86] studied the the boundary-layer processes for a vortex above a no-slip wall in a stagnant fluid. The vortex in their investigation moves along the boundary due to self-induced velocity. This setup was modeled by considering point vortices. Recently, Obabko and Cassel [78] considered a thick-core vortex, which is essentially one half of a Lamb dipole. It was assumed that the self-induced velocity balances the free stream velocity such that the vortex remains at a fixed location with respect to the wall. The presence of the vortex induces an adverse pressure gradient along the boundary. Recall that the pressure gradient along the boundary can be related to a flux of vorticity into the upper plane, see Eq. (1.30). The flux of vorticity into the upper plane results in the formation of a secondary recirculation zone. This process is followed by a detachment of the boundary layer. Fig. 1.3 displays the development of shear layer instabilities and the subsequent vorticity injection into the flow at $Re = 10^4$, based on the self-induced velocity (in balance with the mean stream velocity) and the vortex radius. First the vorticity layers roll up and form an array of small-scale vortices in the zone between the primary vortex and the wall. At subsequent times the vortices grow in size and detach from the wall. By this process high-amplitude vorticity is transported into the bulk of the flow.

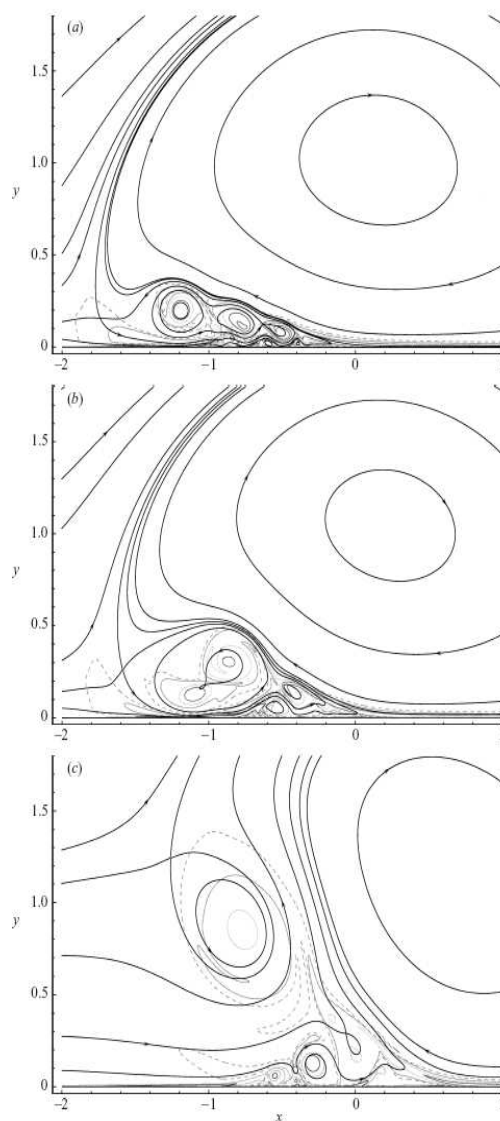


Figure 1.3 – The development of shear layer instabilities in the case of an isolated vortex near a no-slip wall. Instantaneous streamlines and vorticity contours for $\text{Re} = 10^4$ (dashed line represents $\omega = 0$) $t = 2.5$, $t = 3.5$ and $t = 4.5$. Figure is adopted from Obabko and Cassel [78]

1.4.1 Dipole-wall collision

In decaying 2D turbulence a vortex is in general not fixed at a certain position in the domain. Due to the induced velocity from the other vortices a vortex has a net velocity and can consequently collide with the domain boundaries. The first numerical and experimental test of a dipolar vortex colliding with a no-slip wall has been performed by Orlandi [80]. A decade later Clercx and van Heijst [23] performed a dipole-wall collision study at extremely high Reynolds numbers in order to quantify the Reynolds number dependence of the enstrophy and palinstrophy production at the instant of collision. Also recently Kramer *et al.* [54] report about a detailed analysis of the dipole-wall collision problem. In the latter study many of the small-scale vorticity features observed by Obabko and Cassel [78] have been observed as well. Clercx and Bruneau [18] studied the numerical convergence issues of dipole-wall collision computations and provided detailed information for benchmark purposes.

Fig. 1.4 gives an illustration of the normal dipole-wall collision obtained by a Chebyshev pseudospectral computation [17, 53]. The Reynolds number is $Re = UW/\nu = 1000$ is based on the half-width W of the container, the rms velocity U and the kinematic viscosity ν . More details about the computational method and the initial flow field will be considered in Chapters 2, 3 and 4. As the dipole impinges the wall at $t \approx 0.3$ relatively thin boundary layers are formed containing oppositely-signed vorticity compared to the approaching (primary) monopoles. In addition high-amplitude vorticity filaments are stripped from the boundary layers yielding two new (secondary) vortex cores, as can be seen in the vorticity contour plot at $t = 0.4$. The trajectories of the new vortices are strongly curved, resulting in a second collision at $t \approx 0.6$. For $t \gtrsim 0.8$ there is no appreciable production of vorticity at the no-slip wall anymore while the vorticity already present is slowly dissipated. In Fig. 1.5 the evolution of the total kinetic energy and enstrophy are presented for different values of the initial Reynolds number.

Clercx and van Heijst [23] recognized two different scaling regimes of the peak enstrophy and palinstrophy during the first collision of the dipole with the no-slip boundaries,

$$Z \propto Re^{0.8}, \quad P \propto Re^{2.25} \quad \text{for } 5 \times 10^2 \lesssim Re \lesssim 2 \times 10^4, \quad (1.39)$$

and for higher Reynolds numbers it was found that

$$Z \propto Re^{0.5}, \quad P \propto Re^{1.5} \quad \text{for } Re \gtrsim 2 \times 10^4. \quad (1.40)$$

For convenience the scaling relation of the enstrophy and palinstrophy at the first collision are expressed as a function of the Reynolds number as defined above, although it is actually the dependence on the kinematic viscosity ν that is measured. The results (1.39) and (1.40) imply that the decay of energy is proportional to $Re^{-0.2}$ for the lower Reynolds numbers and becomes proportional to $Re^{-0.5}$ in the large Reynolds number limit. This is markedly different compared with the

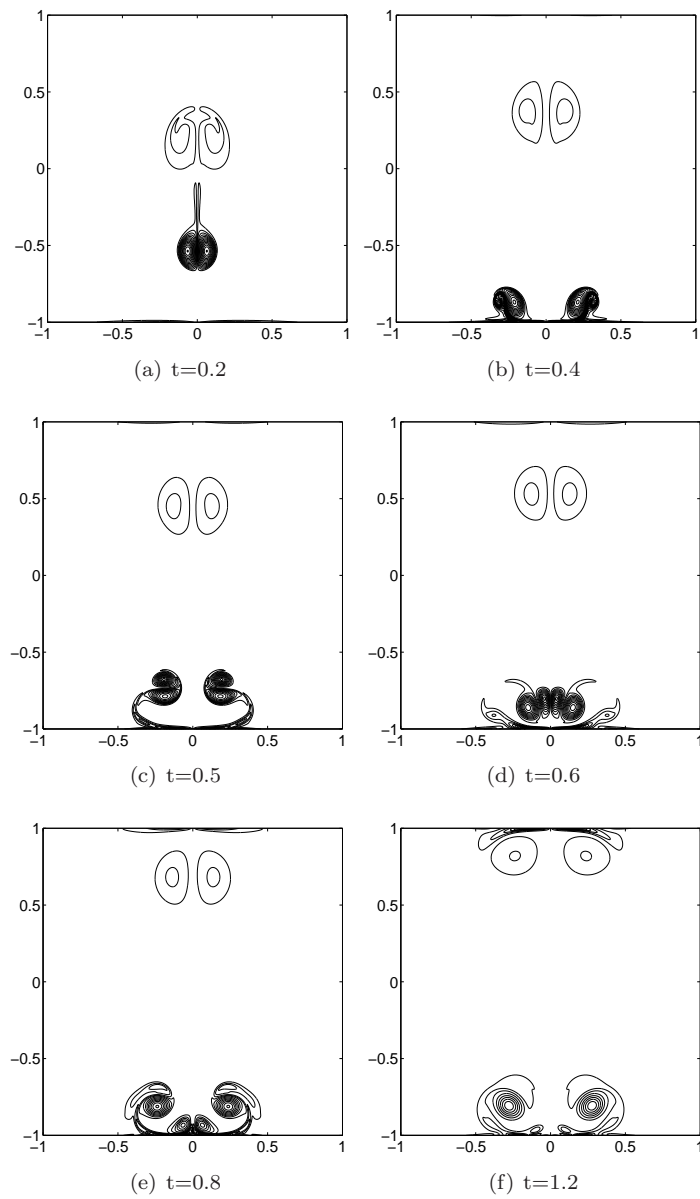


Figure 1.4 – Contour plots of the vorticity field of a normal dipole-wall collision with $Re = 1000$. In this simulation 1024 Chebyshev modes are used perpendicular to the wall and 2048 Fourier modes for the periodic channel direction. The time step is given by $\delta t = 10^{-5}$. Contour levels are drawn for $-270, -50, -30, -10, 10, 30, 50, \dots, 270$.

periodic case where the energy decay is proportional to Re^{-1} . Note that on a periodic domain the enstrophy is bounded by the initial condition, see (1.12) and thus results in an energy decay rate proportional to Re^{-1} , as can be deduced from (1.10).

Using steady boundary-layer theory Clercx and van Heijst [23] proposed the following scaling:

$$\begin{aligned} Z &\propto \frac{\Gamma_b^2}{D\delta_b}, \\ P &\propto \frac{\Gamma_b^2}{D\delta_b^3}, \\ \omega|_{\partial\Omega} &\propto \frac{\Gamma_b}{D\delta_b}, \\ \partial_n\omega|_{\partial\Omega} &\propto \frac{\Gamma_b}{D\delta_b^2}, \end{aligned} \tag{1.41}$$

where δ_b denotes the boundary-layer thickness and Γ_b represents the circulation contained by the boundary layer. Usually it is assumed that inside the boundary layer the convective terms balance the viscous terms in the Navier-Stokes equations, which yields a standard estimate for the boundary-layer thickness proportional to $\text{Re}^{-1/2}$. If it is assumed that the circulation inside the boundary layer does not depend on the Reynolds number, the scaling (1.41) is consistent with the assumption of a finite pressure distribution along the boundary. Note that at the boundary it holds that $\frac{\partial p}{\partial x} = -\nu\frac{\partial\omega}{\partial y}$, where x is the wall-tangential direction and y represents the wall-normal direction. This implies that the pressure at the domain boundary is also proportional to Γ_b .

If it is assumed that the circulation in the boundary layer is virtually independent of the Reynolds number and that the proposed scaling of the boundary-layer thickness holds, it correctly explains the observed high Reynolds number scaling behaviour (1.40). It was verified by Clercx and van Heijst that the circulation of the boundary layer is virtually independent of the Reynolds number for $Re \gtrsim 10^4$. Furthermore, for the lower Reynolds numbers some dependence of the circulation on the Reynolds number was found, which could explain some increase of the theoretical scaling exponents. Detailed measurements of the circulation of both the primary and secondary boundary layer at the instant of collision are provided by Kramer *et al.* [54]. The corresponding values of the primary boundary layer circulation are $\Gamma_b = 1.67$ for $Re = 625$, $\Gamma_b = 2.00$ for $Re = 1250$ and $\Gamma_b = 2.92$ for $Re = 20000$. Indeed there is some dependence of the circulation on the Reynolds number that could justify a small increase of the scaling exponents of the enstrophy and palinstrophy of approximately 0.2. This might explain the increase of the exponent that corresponds with the total enstrophy from the theoretical value of 0.5 to 0.7. However, it strongly underestimates the observed scaling exponent for

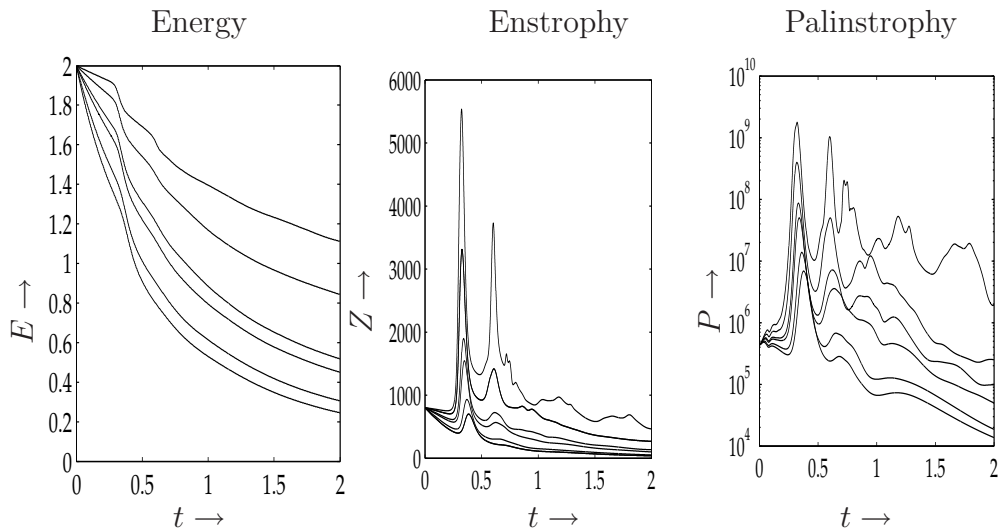


Figure 1.5 – Total kinetic energy $E(t)$, enstrophy $Z(t)$ and palinstrophy $P(t)$ for a normal dipole-wall collision, Reynolds number $Re = 500, 625, 1000, 1250, 2500$ and 5000 . These high-resolution computational data are provided by W. Kramer (private communication).

the palinstrophy with a theoretical value of 1.5 to 1.7, whereas the measured exponent is 2.25.

Besides the normal dipole wall collision Clercx and van Heijst [23] considered the case of oblique dipole-wall collision. In this case the dipole traverses the square bounded domain under a certain angle with respect to the sidewalls. The same scaling results have been obtained as for the normal-dipole wall collision (1.40, 1.39). A very interesting aspect for the oblique case is the production of angular momentum. As can be deduced from Eq. (1.19) a net torque can develop during an oblique dipole-wall collision with the no-slip boundaries. A very detailed report about the normal and oblique dipole-wall collision is provided by Clercx and Bruneau [18]. From their results it can be deduced that the vorticity gradient perpendicular to the wall increases by a factor 10 if the Reynolds number is increased from 625 to 2500, which increases significantly faster than the expected linear Reynolds number dependence derived from steady boundary-layer theory, see Eq. (1.41). Consequently the integrand of the first term on the right-hand side of the angular momentum balance expressed as in Eq. (1.19) increases faster than the Reynolds number. It was observed, however, that the angular momentum production during the first collision is virtually insensitive for the Reynolds number, provided that $Re \gtrsim 500$. Apparently the integral over the domain boundary vir-

tually cancels out the extremely high positive and negative values of the vorticity gradient at the domain boundaries. This results in a finite value for the contribution of the vorticity gradients or pressure contribution in the angular momentum balance expressed as (1.19) or in the form (1.18), respectively. This is an important observation for angular momentum generation in fully developed turbulence in a geometry with no-slip boundaries, which will be considered in Chapters 6 and 7.

1.5 Alternative scaling relations for boundary-layer vorticity

In this Section we proceed with a study of the enstrophy production during a dipole-wall collision. Recall that in section 1.4.1 some details of the study of Clercx and van Heijst [23] on this particular problem have been addressed. They proposed a steady boundary-layer model to obtain scaling relations for the enstrophy and palinstrophy with respect to the initial Reynolds number. This model showed excellent agreement for extremely high Reynolds numbers typically larger than 20000. For moderate Reynolds numbers the steady boundary-layer model is, however, inconsistent with the numerical data. Instead of applying steady boundary-layer theory an alternative scaling method is proposed in this section. The time dependence of the vortex-wall problem is explicitly taken into account.

1.5.1 Alternative scaling model

Two typical time-scales can be associated with the dipole-wall collision problem. The first time scale T_a can be related to the vortex-wall approach. It is a measure of the time-span between the instant a boundary layer starts to form and the instant of collision. For sufficiently high Reynolds number it can be assumed that the amount of dissipation of the total kinetic energy of the vortex in the interior of the domain can be neglected. Therefore the time scale T_a can be estimated by means of the translation speed V and the diameter D of the vortex core,

$$T_a \propto \frac{D}{V}. \quad (1.42)$$

The second time scale T_p is a measure for the duration of the collision or the contact time with the viscous boundary layer. Note that as the dipolar vortex approaches the wall a boundary layer is formed due to the induction of velocity in the near-wall region. As the primary vortex cores move back into the interior of the flow domain the magnitude of the velocity in the boundary layer will decrease again. A typical shape of the vortex trajectory during the collision with the wall is given in Fig. 1.6. It does not require much imagination to realize that the vortex

rebound can be compared with half a period of the oscillating plate problem considered in section 1.3: now it is the fluid that exhibits oscillatory motion, whereas the boundary is fixed. Note that the vorticity is produced due to the presence of a pressure gradient along the wall, which is equivalent to an acceleration of the wall, as can be seen in the vorticity flux equation (1.30).

If we adopt the oscillating plate as an analogous boundary-layer problem the scaling relations assembled in Eq. (1.35) can be used to predict the scaling of the enstrophy and palinstrophy in the viscous boundary layer of the dipole-wall problem.

We want to express the scaling relations in terms of the Reynolds number. Therefore, it is essential to express T_p in terms of D , V and ν . For low Reynolds numbers $\text{Re} < \text{Re}_c$ the duration of the collision can be related to the ratio of the boundary-layer thickness $\delta \propto \sqrt{\nu T_a}$ and the magnitude of the normal-wall component of the velocity v_\perp of the vortex core at the instant of collision with the top of the boundary layer,

$$T_p \propto \frac{\delta}{v_\perp} \propto \frac{\sqrt{\nu T_a}}{v_\perp} \propto \frac{\sqrt{\nu D}}{V^{3/2}} \quad \text{for} \quad \text{Re} < \text{Re}_c. \quad (1.43)$$

Note that v_\perp is smaller than the translation speed of the vortex V , because the trajectory strongly bends during the vortex-wall approach, see Fig. 1.6. We consider now a sufficiently high Reynolds number, typically $\text{Re} \gtrsim 1000$. During the first part of the collision the vortex cores follow the same trajectory as in the stress-free case, which is virtually Reynolds number independent for $\text{Re} > 1000$. Therefore, it can be assumed that the velocity component v_\perp does not depend significantly on the Reynolds number. On the other hand, the viscous boundary layer is thicker for lower Reynolds numbers or larger values of the kinematic viscosity. This will result in a longer duration time of the collision, as the boundary layer will resist the motion of the incoming vortex over a larger distance. Realize that the pressure inside the boundary layer is uniform within first order, which can readily be derived from the wall-normal component of the momentum equation (1.1) at the no-slip boundary.

For sufficiently high Reynolds numbers the process described in the previous paragraph can be neglected. It can then be assumed that the collision time becomes independent of the kinematic viscosity and thus a function of V and D only,

$$T_p \propto \frac{D}{V} \quad \text{for} \quad \text{Re} > \text{Re}_c. \quad (1.44)$$

Inserting the expression (1.43) for T_p in the range $\text{Re} < \text{Re}_c$ into the scaling expression of the oscillating plate problem Eq. (1.35) yields that,

$$\begin{aligned} Z &\propto \text{Re}^{3/4} \\ P &\propto \text{Re}^{9/4}. \end{aligned} \quad (1.45)$$

For the high Reynolds number regime $Re > Re_c$ it is found, on the other hand, by inserting (1.44) into Eq. (1.35) that,

$$\begin{aligned} Z &\propto Re^{1/2} \\ P &\propto Re^{3/2}. \end{aligned} \quad (1.46)$$

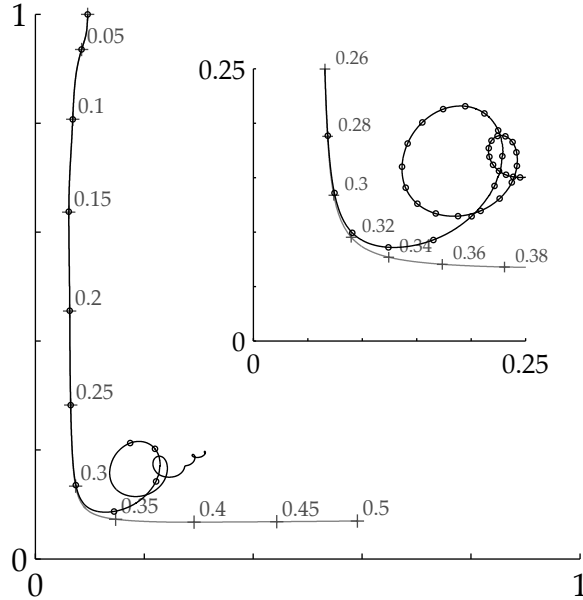


Figure 1.6 – Trajectory of a dipole approaching a stress-free or a no-slip wall for $Re=1250$. The path of the dipole colliding with a no-slip wall (black) compared with the path in case a stress-free boundary condition is applied (gray). The position of the maximum core vorticity at specific times (+0), where time is denoted by the labels. Figure is adopted from Kramer et al. [54].

1.5.2 Validation

The scaling relations (1.45) agree reasonably well with the scaling relation (1.39) found in the numerical study on dipole-wall collisions conducted by Clercx and van Heijst [23] with $Re_c = 20000$. Also the data obtained in the high Reynolds number regime $Re \gtrsim 20000$ found by the same authors (1.39) is consistent with the scaling relations (1.46).

Although the scaling result shows satisfactory correspondence with the numerical data for enstrophy and palinstrophy it is important to verify if it is indeed

conjecture (1.43) that explains the anomalous scaling behaviour for $Re < 20000$. It is however difficult to precisely obtain the value of time-scale T_p . It can be based for instance, on the width of the enstrophy or the palinstrophy peaks in Fig. 1.5. The curves obtain a more spiky appearance for high Reynolds numbers, which could indicate a decreasing duration time of the dipole-wall collision. A more convenient method to verify the validity of the scaling (1.43) is to consider the time derivative of the palinstrophy $P(t)$. Following the same oscillating plate analogy an expression can be derived for the time derivative of the palinstrophy proportional to

$$\frac{dP}{dt} = \frac{DV^2}{T_p^{5/2} \nu^{3/2}}. \quad (1.47)$$

The conjecture for the scaling of the collision time (1.43) yields then an estimate for the time derivative of the palinstrophy according to,

$$\frac{dP}{dt} \propto Re^{11/4}. \quad (1.48)$$

Fig. 1.7 assembles the data of the enstrophy, palinstrophy and the derivative of the palinstrophy for different Reynolds numbers in a double logarithmic plot. It can be seen that all the estimates are in excellent agreement for $1000 < Re < 20000$ with the alternative scaling proposal. Small deviations can be observed for the data obtained with $Re \lesssim 1250$.

Note that it is assumed that the typical velocity V is constant for $500 < Re < 2 \times 10^4$. The rms velocity at the instant of the collision changes significantly between Reynolds numbers of 625 and 2500, namely from 0.79 to 0.93, respectively. For higher Reynolds numbers the difference is, however, negligible since the rms velocity is 0.96 for $Re = 20000$, thus within a few percent error margin of the corresponding value for the $Re = 2500$ case. Recall that in Kramer *et al.* [54] it was observed that the shape of the vortex for $Re \lesssim 1250$ depends on the Reynolds number. Furthermore, the approach of the dipole has a different appearance due to interaction with the detached vorticity layers for the lower Reynolds number cases. These effects might explain the minor deviations observed for $Re \lesssim 1250$ in Fig. 1.7.

1.5.3 Finite pressure assumption

It is also possible to obtain an estimate for the pressure at the boundary by the vorticity flux equation (1.30) and the estimate in the oscillating plate problem for the velocity gradients perpendicular to the wall yielding,

$$p|_{\partial\Omega} \propto \frac{\rho DV}{T_p}. \quad (1.49)$$

Note that for an incompressible flow only the pressure difference is relevant. Here we set the domain averaged pressure equal to zero. Eq. (1.49) reveals an intimate

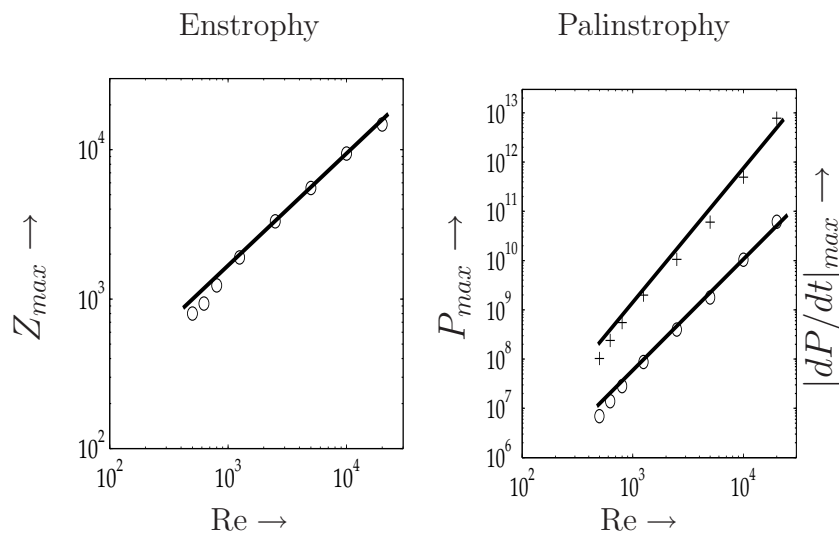


Figure 1.7 – Maxima of the enstrophy Z and the Palinstrophy P (open circles) and the maximum of the time derivative of the palinstrophy (plus signs). Reference line $Re^{0.75}$ for Z in left-hand panel and in the right-hand panel $Re^{2.25}$ and $Re^{2.75}$ for P and the time derivative of P , respectively. The high-resolution data is provided by W. Kramer (private communication), setup of simulations and more details are reported in Kramer *et al.* [54].

relationship between the collision time T_p and the pressure in the boundary layer. Therefore, the usual assumption that the pressure becomes finite in the limit of vanishing viscosity is consistent with the conjecture (1.44) of a finite value of the collision time T_p . The impulse exerted by the boundary layers on the colliding vortex can be estimated by using the estimate (1.49) for the pressure and the collision time T_p :

$$I \propto \rho D^2 V. \quad (1.50)$$

The right-hand side of (1.50) is proportional to the change of momentum as the dipole collides with the boundary layer. Note that for increasing Reynolds number in the range $Re < Re_c$ the collision time T_p decreases according to (1.44), and the pressure increases with $1/T_p$ such that the net change of momentum is essentially constant.

Concluding remarks

The study of Kramer *et al.* [54] reports on the formation of a secondary boundary layer and consequent development of shear layer instabilities as soon as the dipole vortex collides with the wall for Reynolds numbers larger than 5000. Therefore,

it is quite remarkable that a simplified unsteady boundary-layer model can still explain the anomalous scaling of the enstrophy and palinstrophy at the instant of collision with satisfactory agreement between the scaling model and the numerical data.

Chapter 2

Numerical methodⁱ

2.1 Introduction

In Chapters 2, 3 and 4 we examine the convergence and accuracy of a fast Fourier spectral method combined with an immersed boundary technique called “volume penalization” [1] to mimic the no-slip boundary condition. Fourier spectral methods are potentially accurate for sufficiently smooth functions on double-periodic domains. Moreover, these methods are fast, relatively easy to implement even for performing parallel computations (see Ref. [107]). Incorporation of no-slip boundaries is, however, not straightforward.

In the volume-penalization approach of Arquis & Caltagirone [3] a Darcy drag term is added to the Navier-Stokes equations such that the velocity is penalized towards zero inside an obstacle. It is analytically shown that by increasing the penalization strength the penalized Navier-Stokes equations converge towards the Navier-Stokes equations with no-slip boundary conditions (see Ref. [1], [14]). Angot and co-workers [1] also present numerical results for 2D flow around a square obstacle, which confirms that the method is indeed converging. The maximum value of the Reynolds number in their simulations, based on the main stream velocity U_0 , the size of the square L , and the kinematic viscosity ν , is $Re = \frac{U_0 L}{\nu} = 80$, which is relatively low. Paccou *et al.*, [83] also found clear convergence results of a volume-penalization approach for a fully hyperbolic problem, *i.e.* the linear wave equation.

Kevlahan & Ghidaglia [51] tested the suitability of a Fourier spectral scheme with volume-penalization for the problem of flow around a cylinder at a substantially higher Reynolds number, $Re = \frac{U_0 D}{\nu} = 1000$, based on the main stream velocity and the diameter D of the cylinder. A drawback of the penalization technique is the formation of steep velocity-gradients inside the porous object, that can deteri-

ⁱThe contents of this chapter is an adapted version of Keetels *et al.* [48]

orate the spectral convergence rate to first order. This effect is generally referred to as the Gibbs phenomenon, visibly present by wiggles in both the Fourier-Galerkin and collocation projection of any piecewise continuous function. Nevertheless, the Gibbs oscillations present in the simulations of Kevlahan & Ghidaglia [51] and Schneider [96] seem to be stable during the flow evolution. This demonstrates that it is possible to perform stable and reasonably accurate Fourier spectral computations of incompressible viscous flow past an arbitrary shaped object. We believe that it is interesting to extend this analysis using the very challenging dipole-wall collision experiment at high Reynolds numbers as a test problem. An important issue is to fully quantify the role of the Gibbs effect on the flow dynamics: is it possible to recover higher-order accuracy of the Fourier spectral scheme? Here, we follow some recent developments in the theory and application of Fourier spectral methods on discontinuous phenomena, see for an overview the work of Gottlieb & Gottlieb [35]. These advances indicate that high-order information can be recovered from stable Fourier spectral computations. We use a high-order recovery technique proposed by Tadmor & Tanner [104]. They propose a mollification procedure, which involves a subtle process of cancelling nearby Gibbs oscillations to obtain an accurate reconstruction of any piecewise continuous function in the physical domain. A strong advantage is that tuning of the parameters is completely avoided. Furthermore, the implementation is quite straightforward and thus relatively easy to optimize from a computational point of view.

Besides the Fourier spectral technique we will consider the Coherent Vortex Simulation (CVS) method with volume-penalization using an adaptive wavelet method. The main idea is to split the flow into two orthogonal parts, a coherent contribution and an incoherent background flow, using a nonlinear wavelet filtering of vorticity [31]. It is shown by Beta *et al.* [10] that the coherent part is mainly responsible for the nonlinear dynamics, while the incoherent background can be considered as decorrelated or structureless. Therefore, Farge & Schneider [30] propose to model its influence on the coherent flow statistically and only solve by direct numerical simulation the few wavelet coefficients that describe the coherent part of the flow. This makes the CVS method potentially fast in terms of CPU time, while the memory requirements can strongly be reduced. Schneider and Farge successfully applied the CVS method to different flow problems such as flow around a cylinder [94], 3D turbulent mixing layers [93], [98] and present some preliminary results (containing aliasing errors) for a dipole-wall collision [95].

In Chapters 3 and 4 we will continue with a more detailed comparison of the CVS and Fourier spectral results with a high-resolution benchmark computation conducted with a Chebyshev-Fourier and Chebyshev spectral method for 2D flow with no-slip boundary conditions in one or two directions, respectively (See Refs. [53], [17]). We start with a description of the volume-penalization technique and formulate different approaches to treat the Darcy drag term in Fourier spectral schemes and in CVS. Then the convergences of these schemes and the penalization

error will be analyzed in terms of isovorticity lines, a global measure of the error in the vorticity and the total kinetic energy and enstrophy of the flow.

2.2 Volume-penalization

2.2.1 The model equation

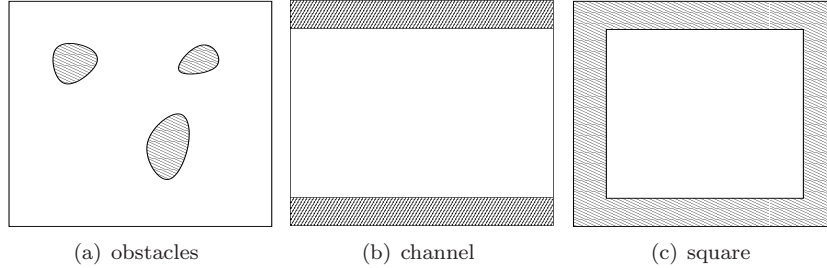


Figure 2.1 – Decomposition of a square computational domain Ω into porous objects Ω_s (dashed) and flow domain Ω_f (white).

Consider an incompressible fluid of unit density, $\rho = 1$, in a domain $\Omega_f \in \mathbb{R}^2$, which evolves according to the Navier-Stokes equations

$$\partial_t \mathbf{u} + (\mathbf{u} \cdot \nabla) \mathbf{u} + \nabla p - \nu \Delta \mathbf{u} = 0 \quad \text{in} \quad \Omega_f \times [0, T] \quad (2.1)$$

and the continuity condition

$$\nabla \cdot \mathbf{u} = 0 \quad \text{in} \quad \Omega_f \times [0, T] \quad (2.2)$$

where $\mathbf{u} = (u(\mathbf{x}, t), v(\mathbf{x}, t))$ is the Eulerian velocity, $p = p(\mathbf{x}, t)$ the scalar kinetic pressure and ν the kinematic viscosity. An impermeable, stationary geometry can be defined by setting the velocity component normal to the wall to zero. The tendency of a fluid to stick to the boundaries $\partial\Omega_f$ is usually modelled by removing the tangential velocity component relative to the wall. The combination of these boundary conditions on each component of the velocity defines the no-slip boundary condition, which reads for a stationary geometry,

$$\mathbf{u}(\mathbf{x}, t) = 0 \quad \mathbf{x} \in \partial\Omega_f, \quad t \in [0, T], \quad (2.3)$$

which is essentially a Dirichlet boundary condition for \mathbf{u} . Note that Eq. (2.1) contains second-order derivatives so two boundary conditions are required for the existence of a unique solution.

In the volume-penalization approach fluid-wall interaction is no longer described

by demanding the no-slip boundary condition (2.3). The basic idea originating from Arquis & Caltagirone [3] is to embed the flow domain in a larger domain Ω , such that $\Omega_f = \Omega \setminus \overline{\Omega_s}$, where Ω_s represents the volume of porous objects. The interaction with the porous objects is modelled by adding a Darcy drag term to the Navier-Stokes equations locally inside Ω_s , which yields the penalized Navier-Stokes equations

$$\partial_t \mathbf{u} + (\mathbf{u} \cdot \nabla) \mathbf{u} + \nabla p - \nu \Delta \mathbf{u} + \frac{1}{\epsilon} H \mathbf{u} = 0 \quad \text{in} \quad \Omega \times [0, T], \quad (2.4)$$

where the mask function H is defined as

$$H = \begin{cases} 1 & \text{if } \mathbf{x} \in \overline{\Omega_s} \\ 0 & \text{if } \mathbf{x} \in \Omega_f. \end{cases}$$

Figure 2.1 shows some examples of possible geometries. In this study we model a channel with two no-slip boundaries and two periodic boundaries and the square bounded geometry with four no-slip boundaries by choosing the mask function shown in Fig. 2.1b and in Fig. 2.1c, respectively. The continuity condition accompanies the penalized Navier-Stokes equations in Ω . On the boundaries of the computational domain $\partial\Omega$ one can consider different boundary conditions. Here we have chosen for the periodic boundary condition on $\partial\Omega$, such that Fourier spectral methods can be applied. For convenience the penalized Navier-Stokes equations (2.4) can be rewritten in velocity-vorticity formulation by taking the curl of Eq. (2.4) and applying several vector identities to arrive at

$$\partial_t \omega + (\mathbf{u} \cdot \nabla) \omega - \nu \Delta \omega + \frac{1}{\epsilon} \nabla \times H \mathbf{u} = 0 \quad \text{in} \quad \Omega \times [0, T], \quad (2.5)$$

where $\omega = (\nabla \times \mathbf{u}) \cdot \mathbf{e}_z$ is the vorticity. Note that the velocity-vorticity formulation is scalar-valued in two dimensions. The volume of the obstacles can be interpreted as a porous medium with permeability ϵ . As a consequence the flow inside Ω_f induces a small and time-dependent velocity inside the obstacles and thus on the boundaries $\partial\Omega_s$. The flow inside the obstacle Ω_s can be matched with the flow inside Ω_f by demanding continuity of both velocity and surface stress. Note that Darcy drag can be considered as a volume force such that the surface stresses $\boldsymbol{\tau}$ in the penalized Navier-Stokes equations (2.4) can be expressed in the usual way, *i.e.* $\boldsymbol{\tau} = \mathbf{n} \cdot \mathbf{T}$ where \mathbf{n} is the outward unit normal on $\partial\Omega_s$ and the stress tensor $\mathbf{T} = \nu(\nabla \mathbf{u} + \nabla \mathbf{u}^t) - p\mathbf{I}$. This implies together with demanding continuity that the velocity is at least C^1 and the pressure C^0 on $\partial\Omega_s$ (see Ref. [14]).

2.2.2 Convergence and regularity

It has been shown rigorously by Angot *et al.* [1] that the solutions of the penalized Navier-Stokes equations converge towards the Navier-Stokes solution in Ω_f

with an $\mathcal{O}(\epsilon^{\frac{1}{4}})$ error bound. Their numerical simulations, however, show a better convergence, indicating that the analytical upper bound for the error is not sharp enough. Later, Carbou & Fabrie [14] improved the analytical error estimate inside the flow domain by using a singular perturbation technique. They obtained formal expansions for the velocity and pressure in terms of $\sqrt{\epsilon}$ inside Ω . In addition, they derived that the upper bound of the penalization error is $\mathcal{O}(\epsilon^{\frac{1}{2}})$ in the L_2 sense of the velocity and velocity gradients with respect to the Navier-Stokes solution in Ω_f with the no-slip boundary condition. Furthermore, they found C^1 continuity in the larger domain Ω of the velocities determined by the penalized Navier-Stokes equations. The C^1 continuity of the $\sqrt{\epsilon}$ and higher-order expansion terms is achieved by the introduction of an asymptotically thin boundary layer proportional to $\sqrt{\nu\epsilon}$ inside the obstacle.

A remarkable result is, however, that the boundary layer components are only required to determine the order ϵ and higher-order terms in the asymptotic expansion of the velocity and pressure inside Ω_f . Therefore, it might be expected that if the spatial resolution is too low to resolve the details of the asymptotic boundary layer, one is still able to compute the solution of the penalized Navier-Stokes equations in Ω_f up to order $\sqrt{\epsilon}$ accurate. Inside the obstacles ($\text{dist}(x, \partial\Omega_s) \gg \sqrt{\nu\epsilon}$) the leading order expansion term for the velocity is order ϵ and for the pressure order zero. These terms can uniquely be determined, again without computing the boundary layer solution. The zeroth-order part of the pressure follows a Laplace equation that can be solved by applying a matching condition on $\partial\Omega_s$. The order ϵ part of the velocity can then be determined by solving a Darcy relation involving the zeroth-order part of the pressure. An advantage of the small skin depth is, on the other hand, that the obstacles can be relatively thin. This implies that not many grid points are required to represent a wall on a Cartesian grid and for adaptive methods, such as CVS, only the flow near the surface of the porous objects needs to be calculated.

2.3 Numerical methods

In this section we present an overview of the different numerical schemes.

2.3.1 Fourier-Galerkin with an explicit treatment of Darcy drag

For the sake of simplicity we write equation (2.5) as

$$\partial_t \omega - \nu \Delta \omega = \mathcal{N}(\omega) \tag{2.6}$$

where

$$\mathcal{N} = -(\mathbf{u} \cdot \nabla) \omega - \frac{1}{\epsilon} \nabla \times H \mathbf{u}.$$

For the exact treatment of the diffusion term we first consider the homogeneous equation, *i.e.*, $\mathcal{N} = 0$. The exact solution can be expressed as,

$$\omega(\mathbf{x}, t) = \omega(\mathbf{x}, t_0) \exp(\nu t \Delta) \quad (2.7)$$

where $\exp(\nu t \Delta)$ is the semi-group of the heat-kernel. By using variation of constants the inhomogeneous equation, *i.e.*, $\mathcal{N} \neq 0$ can be written in the form

$$\partial_t \{\omega \exp(-\nu t \Delta)\} = \mathcal{N}(\omega) \exp(-\nu t \Delta), \quad (2.8)$$

see, *e.g.*, Ref. [96] for details. The vorticity and velocity are expanded with a doubly truncated Fourier series as a trial basis,

$$\omega_N(\mathbf{x}, t) = \sum_{k_x=-N/2}^{N/2-1} \sum_{k_y=-N/2}^{N/2-1} \hat{\omega}_{\mathbf{k}}(t) \exp(i\mathbf{k} \cdot \mathbf{x}), \quad (2.9)$$

where $\mathbf{k} = (k_x, k_y)$ and $\hat{\omega}_{\mathbf{k}}(t)$ denotes the continuous Fourier expansion coefficients of $\omega(\mathbf{x}, t)$, which are defined for simplicity on $\mathbf{x} \in [0, 2\pi]^2$ as

$$\hat{\omega}_{\mathbf{k}}(t) = \frac{1}{4\pi^2} \int \omega(\mathbf{x}, t) \exp(-i\mathbf{k} \cdot \mathbf{x}) d\mathbf{x}. \quad (2.10)$$

Note that the trigonometric polynomials are complete for functions in $L_2(\Omega)$. Thus it is, in principle, possible to make an expansion of functions with Dirichlet boundary conditions on $\partial\Omega$ as well. However, the convergence of the Fourier series expansion is only guaranteed in the L_2 -norm and not in the pointwise sense. Note that setting a Dirichlet boundary condition actually requires convergence in the pointwise sense. Therefore, it is not possible to directly take into account the Dirichlet boundary condition on the domain boundaries. One thus has to apply immersed boundary techniques like, for example, the volume-penalization method in this study and consider periodic boundary conditions.

By virtue of the continuity condition (2.2) the velocity $\hat{\mathbf{u}}_{\mathbf{k}}(t)$ can be computed from $\hat{\omega}_{\mathbf{k}}(t)$,

$$\hat{\mathbf{u}}_{\mathbf{k}}(t) = \frac{i(k_y \mathbf{e}_x - k_x \mathbf{e}_y)}{k^2} \hat{\omega}_{\mathbf{k}}(t). \quad (2.11)$$

where $k^2 = \mathbf{k} \cdot \mathbf{k}$. By substitution of the expansions into Eq. (2.8) and taking inner products with the Fourier system as test functions as well, we follow a Fourier-Galerkin approach yielding an evolution equation for each \mathbf{k}

$$d_t \{\hat{\omega}_{\mathbf{k}} \exp(\nu k^2 t)\} = \mathcal{K}(\hat{\omega}_{\mathbf{k}}) \exp(\nu k^2 t), \quad (2.12)$$

where

$$\mathcal{K} = [(\mathbf{u}_N \cdot \nabla) \omega_N]_{\mathbf{k}} + \frac{ik_x}{\epsilon} [Hv_N]_{\mathbf{k}} - \frac{ik_y}{\epsilon} [Hu_N]_{\mathbf{k}}. \quad (2.13)$$

This \mathcal{K} term is evaluated by collocation in the physical domain where aliasing is avoided by applying the zero-padding technique introduced by Orszag [81], generally referred to as the 2/3-rule (see, for details, Ref. [13]). Furthermore, it is important to realize that in the Fourier-Galerkin approach the precise form of the continuous equation in this case the velocity-pressure (2.4) and velocity-vorticity (2.5) formulations yield identical algorithms. The computation of \mathcal{K} involves Fourier projections of the discontinuous restricted velocities Hu and Hv , which might affect the convergence of the scheme.

A third-order extrapolated backward differentiation (BDF3) formula [39] is applied for the time discretization of Eq. (2.12)

$$\sum_{h=0}^3 \alpha_h \hat{\omega}_{\mathbf{k}}^{n+1-h} \exp(-\nu k^2 h \delta t) = -\delta t \sum_{h=1}^3 \beta_h \mathcal{K}(\hat{\omega}_{\mathbf{k}}^{n+1-h}) \exp(-\nu k^2 h \delta t). \quad (2.14)$$

The values of the coefficients α_h and β_h , which can be found in Table 2.1, are given by the backward differentiation scheme and extrapolation, respectively. We chose this time scheme for the good stability results obtained by Kress & Löstedt [56]. They considered backward difference time schemes with fourth-order finite differences for the spatial discretization of the incompressible Navier-Stokes equations with no-slip boundaries in a straight channel. Note that the treatment of viscous diffusion in Eq. (2.14) is exact. The accuracy and stability restrictions of the time scheme solely arise from the nonlinear \mathcal{K} term.

2.3.2 Fourier collocation with an implicit treatment of Darcy drag

A drawback of the explicit treatment of the Darcy drag is that for stability the time step has to be of the same order as ϵ , because the problem is stiff. Recall that the accuracy of the penalized Navier-Stokes equations with respect to the no-slip boundary condition converges relatively slow with $\sqrt{\epsilon}$. Therefore, it might be necessary to decouple the time step from ϵ , such that the time step is only limited by the CFL number. Kevlahan & Ghidaglia [51] used a GMRES Krylov subspace technique in an explicit time scheme for this purpose. To achieve a stiffly stable third-order time scheme, without additional memory or computational requirements we consider an alternative method. It is based on a collocation approach of the penalized Navier-Stokes equations in primitive variables (2.4) at the grid points $\mathbf{x} = (2\pi n_x/N, 2\pi n_y/N)$ where n_x and n_y range from 0, ..., $N - 1$. The grid values of \mathbf{u}_N and p_N are now related to the discrete Fourier coefficients defined as

$$\tilde{p}_{\mathbf{k}} = \frac{1}{N^2} \sum_{n_x=0}^{N-1} \sum_{n_y=0}^{N-1} p_N(\mathbf{x}) \exp(-i\mathbf{k} \cdot \mathbf{x}) \quad (2.15)$$

such that

$$p_N(\mathbf{x}) = \sum_{k_x=-N/2}^{N/2-1} \sum_{k_y=-N/2}^{N/2-1} \tilde{p}_{\mathbf{k}} \exp(i\mathbf{k} \cdot \mathbf{x}) \quad (2.16)$$

due to the orthogonality of the Fourier basis. A third-order extrapolated BDF scheme with exact differentiation of the diffusion term can be expressed as

$$\alpha_0 \mathbf{u}_N^{n+1} + \delta t \mathbf{L}_N(\mathbf{u}_N^{n+1}) = - \sum_{h=1}^3 (\delta t \beta_h \mathbf{G}_N(\mathbf{u}_N^{n+1-h}) + \alpha_h \mathbf{u}_N^{n+1-h}) e^{h\delta t \nu \Delta} \quad (2.17)$$

$$\tilde{\nabla} \cdot \mathbf{u}_N = 0 \quad (2.18)$$

where $\mathbf{G}_N = (\mathbf{u}_N \cdot \tilde{\nabla}) \mathbf{u}_N + \tilde{\nabla} p_N$, $\mathbf{L}_N = \frac{1}{\epsilon} H \mathbf{u}_N$ and a tilde stresses that collocation derivatives are used. The same values of the coefficients α_j and β_j are applied as for the explicit time scheme, see Table 2.1. Thus the Darcy drag is now evaluated with backward differentiation instead of extrapolation. The error $\tilde{\nabla} u - (\nabla u)_N$ is of the same order as the truncation error of the Fourier-Galerkin derivative of u (see Ref. [13]). In the following we will neglect this error and suppose that interpolation and differentiation commute, *i.e.*, $\tilde{\nabla} u = (\nabla u)_N$ for simplicity. To keep the velocity field solenoidal with respect to the collocation derivatives we demand,

$$\tilde{\nabla} \cdot \mathbf{G}_N = 0, \quad (2.19)$$

such that the Helmholtz decomposition of \mathbf{G}_N only contains a rotational part,

$$\mathbf{G}_N = \tilde{\nabla} \times \mathbf{A}. \quad (2.20)$$

Taking the curl on both sides of equation (2.20) yields,

$$\tilde{\nabla} \times \left[(\mathbf{u}_N \cdot \tilde{\nabla}) \mathbf{u}_N \right] = \tilde{\nabla} \times (\tilde{\nabla} \times \mathbf{A}) = \tilde{\nabla} (\tilde{\nabla} \cdot \mathbf{A}) - \tilde{\nabla}^2 \mathbf{A}. \quad (2.21)$$

The convolution sum on the left-hand side is evaluated by using the 2/3 rule to avoid aliasing errors. In transform space it is then straightforward to obtain the Fourier expansion coefficients of \mathbf{A} . In addition, it is possible to obtain \mathbf{G}_N via the Helmholtz decomposition (2.20). This procedure finally yields the following algorithm

$$\mathbf{G}_N(\mathbf{u}_N) e^{h\delta t \nu \Delta} = \sum_{\mathbf{k} \in \mathbb{Z}^2} \frac{i(k_y \mathbf{e}_x - k_x \mathbf{e}_y)}{k^2} \left[(\mathbf{u}_N \cdot \tilde{\nabla}) \omega_N \right]_{\mathbf{k}} e^{-\nu k^2 h \delta t + i\mathbf{k} \cdot \mathbf{x}}. \quad (2.22)$$

The penalization parameter ϵ can be chosen independent from the time step without additional FFTs (3 forward and 4 backward). Furthermore, it is not necessary to perform a Fourier expansion of the discontinuous restricted velocities Hu and Hv . Therefore, the only convergence limitations appear from the regularity of the penalized Navier-Stokes equations considered in section 2.2.2.

Table 2.1 – Coefficients for third-order extrapolated backward differentiation (BDF3)

α_0	α_1	α_2	α_3	β_1	β_2	β_3
11/6	-3	3/2	-1/3	3	-3	1

2.3.3 Coherent vortex simulation

Coherent Vortex Simulation (CVS) introduced by Farge and co-workers [31], [30] is a new method to compute turbulent flows. It is based on the wavelet filtered Navier–Stokes equations, whose solutions are computed in an adaptive wavelet basis. The wavelets are dynamically selected to track the flow evolution with a reduced number of modes (cf. [93], [30], [94] [98]). The success of this methodology hinges on the ability of the wavelets to achieve a significant reduction in the number of modes needed to describe the flow evolution. In the following we briefly summarize the adaptive wavelet method to solve the two-dimensional Navier–Stokes equations in velocity-vorticity formulation (2.5).

In the CVS computations we employ a semi-implicit time scheme of second order [32], *i.e.*, an Euler–backwards scheme for the diffusion term and an Adams–Bashforth scheme for the advection and penalization term. The explicit treatment of the advection and penalization terms implies a limitation of the time step size to guarantee stability, *i.e.* the time step has to satisfy the CFL condition and also has to be smaller than the penalization parameter. Discretizing (2.6) therewith we obtain

$$(\gamma - \nu\Delta)\omega^{n+1} = \frac{4}{3}\gamma\omega^n - \frac{1}{3}\gamma\omega^{n-1} + \mathcal{N}(2\omega^n - \omega^{n-1}) \quad (2.23)$$

$$\Delta\Psi^{n+1} = \omega^{n+1} \quad \text{and} \quad \mathbf{u}^{n+1} = \nabla^\perp\Psi^{n+1} \quad (2.24)$$

where $\gamma = 2/(3\delta t)$, $\nabla^\perp = (-\partial_y, \partial_x)$ and Ψ denotes the stream function. Hence in each time step two elliptic problems have to be solved and a differential operator has to be applied. Formally, the above equations can be written in the abstract form $Lu = f$, where L is an elliptic operator with constant coefficients, corresponding to a Helmholtz type equation for ω with $L = (\gamma - \nu\Delta)$ and a Poisson equation for Ψ with $L = \Delta$.

For the spatial discretization we use a Petrov–Galerkin scheme. The trial functions are orthogonal wavelets and the test functions are operator-adapted wavelets. To solve the elliptic equations $Lu = f$ at time step t^{n+1} we develop u^{n+1} into an orthogonal wavelet series, *i.e.*, $u^{n+1} = \sum_\lambda \tilde{u}_\lambda^{n+1} \psi_\lambda$, where $\lambda = (j, i_x, i_y, d)$ denotes the multi-index containing scale j , space i_x, i_y and direction information d . Requiring that the residuum vanishes with respect to all test functions $\theta_{\lambda'}$, we obtain a linear system for the unknown wavelet coefficients \tilde{u}_λ^{n+1} of the solution u :

$$\sum_\lambda \tilde{u}_\lambda^{n+1} \langle L\psi_\lambda, \theta_{\lambda'} \rangle = \langle f, \theta_{\lambda'} \rangle. \quad (2.25)$$

The test functions θ are defined such that the stiffness matrix turns out to be the identity. Therefore the solution of $Lu = f$ reduces to a change of the basis, *i.e.*, $u^{n+1} = \sum_{\lambda} \langle f, \theta_{\lambda} \rangle \psi_{\lambda}$. The right-hand side f can then be developed into a biorthogonal operator adapted wavelet basis $f = \sum_{\lambda} \langle f, \theta_{\lambda} \rangle \mu_{\lambda}$, with $\theta_{\lambda} = L^{*-1} \psi_{\lambda}$ and $\mu_{\lambda} = L \psi_{\lambda}$ ($*$ denotes the adjoint operator). By construction θ and μ are biorthogonal, $\langle \theta_{\lambda}, \mu_{\lambda'} \rangle = \delta_{\lambda, \lambda'}$. It can be shown that both have similar localization properties in physical and Fourier space as has ψ and that they form a Riesz basis [32].

To get an adaptive space discretization for the problem $Lu = f$ we consider only the significant wavelet coefficients of the solution. Hence we only retain coefficients \tilde{u}_{λ}^n which have an absolute value larger than a given threshold $\tilde{\varepsilon}$, *i.e.*, $|\tilde{u}_{\lambda}^n| > \tilde{\varepsilon}$. The corresponding coefficients are shown in Fig. 2.2 (white area under the solid line curve). The threshold $\tilde{\varepsilon}$ is not constant in time. It depends on the enstrophy Z of the flow in the following way

$$\tilde{\varepsilon}(t) = \tilde{\varepsilon}_0 \sqrt{Z(t)/Z(t_0)}. \quad (2.26)$$

with a constant $\tilde{\varepsilon}_0$. This choice is motivated for decaying flows to maintain the relative error in the enstrophy. To be able to integrate the equation in time we have to account for the evolution of the solution in wavelet-coefficient space (indicated by the arrow in Fig. 2.2). Therefore we add at time step t^n the local neighbours to the retained coefficients, which constitute a security zone (grey domain in Fig. 2.2). The equation is then solved in this enlarged coefficient set (white and grey region in Fig. 2.2) to obtain $\tilde{u}_{\lambda}^{n+1}$. Subsequently, we threshold the coefficients and retain only those with $|\tilde{u}_{\lambda}^{n+1}| > \tilde{\varepsilon}$ (coefficients under the dashed curve in Fig. 2.2). This strategy is applied in each time step and allows hence to track automatically the evolution of the solution in scale and space.

The nonlinear term $f(u^n)$, where the wavelet coefficients of u^n are given is evaluated in physical space on a locally refined grid. This approach is similar to the pseudo-spectral evaluation of nonlinear terms used in spectral methods, and therefore this method is called pseudo-wavelet technique. The prerequisites, however, are that fast adaptive wavelet decomposition and reconstruction algorithms are available. This means that functions can be reconstructed on a locally refined grid from a sparse set of their significant wavelet coefficients and vice versa, which are given in [32]. The method can be summarized as follows: starting from the significant wavelet coefficients of u , *i.e.*, $|\tilde{u}_{\lambda}| > \tilde{\varepsilon}$, one reconstructs u on a locally refined grid, $u(x_{\lambda})$. Then one can evaluate $f(u(x_{\lambda}))$ pointwise and the wavelet coefficients of f can be calculated using the adaptive decomposition to get \tilde{f}_{λ} .

Finally, we have to calculate those scalar products of the r.h.s f with the test functions θ , to advance the solution in time. We compute $\tilde{u}_{\lambda} = \langle f, \theta_{\lambda} \rangle$ belonging to the enlarged coefficient set (white and gray region in Fig. 2.2). In summary the above algorithm is of $O(N^2)$ complexity, where N denotes the number of wavelet coefficients used in the computation per spatial direction.

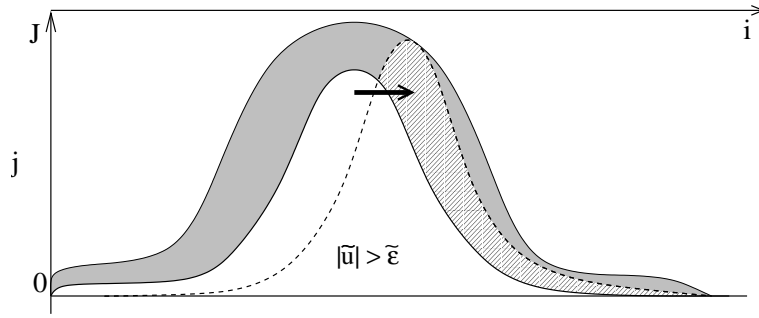


Figure 2.2 – Illustration of the dynamic adaptation strategy in wavelet coefficient space. The vertical axis represents scale and the horizontal axis represents 1D space information denoted by j and i , respectively, in the multi-index λ . The white area under the solid curve represents the wavelet coefficients at t_n , the gray region is the security zone and the dashed region represents the distribution of the wavelet coefficients at the new time-level t_{n+1} .

2.3.4 Chebyshev spectral methods

Pseudospectral simulations were performed with numerical codes developed by Clercx [17] and Kramer [53] for the square bounded and a periodic channel geometry, respectively. For the square bounded domain the flow variables are expanded by Chebyshev polynomials in both directions. The solver of Kramer [53] is very similar to the solver of Clercx [17]. The main difference is that a Fourier expansion of the flow variables in the periodic direction has been applied. In the non-periodic direction the flow variables are represented by Chebyshev expansions as well. An advantage of the latter approach is that it is easier to achieve high-resolution computations both in the direction normal and tangential to the wall.

On the domain Ω_f , the vorticity problem can be written in the dimensionless form as put forward by Daube [26]

$$\begin{cases} \frac{\partial \omega}{\partial t} + (\mathbf{u} \cdot \nabla) \omega = \frac{1}{Re} \Delta \omega & \text{in } \Omega_f \times [0, T] \\ \omega(\cdot, 0) = \omega_0 & \text{in } \Omega_f \\ \omega = (\nabla \times \mathbf{u}) \cdot \mathbf{e}_z & \text{on } \partial \Omega_f \times [0, T] \end{cases} \quad (2.27)$$

where ω_0 is initial condition. The integral-scale Reynolds number is defined as $Re = UW/\nu$ (where U is a characteristic velocity of the flow, W the half-width of the domain and ν the kinematic viscosity of the fluid). The vorticity problem (2.27) has to be solved in combination with the Poisson problem

$$\begin{cases} \Delta \mathbf{u} = \mathbf{e}_z \times \nabla \omega & \text{in } \Omega_f \times [0, T] \\ \mathbf{u} = 0 & \text{on } \partial \Omega_f \times [0, T], \end{cases} \quad (2.28)$$

with \mathbf{e}_z the unit vector perpendicular to the plane of the flow. Note that for the periodic channel geometry the no-slip boundary condition is only applied in the

non-periodic direction. The time discretization in the square bounded geometry of the vorticity equation (2.27) consists of the second-order explicit Adams-Bashforth scheme for the advection term and the implicit Crank-Nicolson procedure for the diffusion term. For the periodic channel geometry a third-order backward difference scheme is applied for diffusion and extrapolation for the advection term.

2.4 Recovery of higher-order accuracy of Fourier schemes

Recall that the $C^1(\Omega)$ and $C^0(\Omega)$ continuity of respectively the velocity and pressure of the penalized Navier-Stokes equations are enforced by an asymptotically thin boundary layer. On the other hand, continuity of the higher derivatives is guaranteed in Ω_f and Ω_s (see Ref. [14]). Thus in the limit $\epsilon \rightarrow 0$ the penalized solution converges to a piecewise continuous function. This might be a problem for Fourier spectral methods since the L_p convergence of both the continuous (2.9) and discrete Fourier expansions (2.16) depends on the global smoothness of a function. As a consequence the uniform convergence is exponential for analytic functions, but a localized discontinuity, on the other hand, makes the Fourier projection suffer from oscillatory behaviour known as the Gibbs phenomenon. The uniform convergence is lost in the neighbourhood of a discontinuity and the L_p convergence rate drops to first order. Fortunately, the convergence rate for piecewise continuous functions in terms of moments against any analytic function $\phi(x)$ (or more rigorously stated in terms of Sobolev norm of negative order) is still excellent,

$$\left| \int_0^{2\pi} \{f_N(x) - f(x)\} \phi(x) dx \right| \leq Kr^N \quad (2.29)$$

for some constant K and a constant r between zero and one. The only requirement is that f belongs to the space L_2 (see Ref. [13] for details). This demonstrates that nearby Gibbs oscillations cancel very rapidly in the weighted mean $\phi(x)$ being any smooth function.

Inspired by estimate (2.29) several techniques have been proposed to recover the pointwise convergence for the Fourier projections of piecewise continuous data. In this paper we follow the so-called ‘‘mollification’’ approach introduced by Gottlieb & Tadmor [38] and later improved by Tadmor & Tanner [104]. It exploits the fast cancellation of the Gibbs oscillations and offers a robust, efficient and general purpose procedure for accurate reconstruction of piecewise continuous data, where tuning of the parameters and roundoff errors are completely avoided.

The basic idea is to equip the analytic weight function $\phi(x)$ in equation (2.29) with two parameters p and θ , such that it is charged to find a balance between localization of the function f and cancellation of neighbouring Gibbs oscillations. To simplify notation we discuss the mollification process of the continuous Fourier

expansion in 1D. It is however straightforward to apply the algorithm in 2D. The procedure can be expressed as a convolution integral of the form,

$$R[f_N](x) = \phi_{p,\theta} \star f_N(x) = \int_0^{2\pi} f_N(\bar{x}) \phi_{p,\theta}(x - \bar{x}) d\bar{x}, \quad (2.30)$$

where the mollifier is defined as $\phi_{p,\theta}(z) = (1/\theta)\rho(z/\theta)D_p(z/\theta)$, with the Dirichlet kernel

$$D_p(\zeta) = \begin{cases} \frac{1}{2\pi} \frac{\sin((p+1/2)\zeta)}{\sin(\zeta/2)} & \text{if } \zeta \neq 0, 2\pi, \dots \\ \frac{2p+1}{2\pi} & \text{if } \zeta = 0, 2\pi, \dots \end{cases} \quad (2.31)$$

and a piecewise C^∞ weight function

$$\rho(\zeta) = \begin{cases} e^{-10\zeta^2/(\pi^2 - \zeta^2)} & \text{if } |\zeta| < \pi, \\ 0 & \text{if } |\zeta| \geq \pi. \end{cases} \quad (2.32)$$

The number of near-vanishing moments of the mollifier and thus the number of cancellations is controlled with p . The parameter θ handles the support $]-\theta\pi, \theta\pi[$ and should be as large as possible to allow a necessary amount of cancellation in the convolution integral (2.30). Due to the requirement of localized regularity of the function f it is not allowed to incorporate a discontinuity. For optimal convergence the support of the mollifier should be $\theta = \max(d(x)/\pi, 2\pi/N)$, where $d(x)$ represents the distance to the nearest jump discontinuity. Note that due to the symmetry of the mollifier it is not possible to use the mollification procedure on the discontinuity itself. An optimal choice for p depends in addition on the support of the mollifier, $p(x) = \kappa\theta(x)N/2$, where κ is an arbitrarily chosen parameter between 0 and 1. The same value $\kappa = 0.5$ is chosen as in the numerical validation of the method presented in Ref. [104]. In order to obtain finite-order convergence in a small region of $\mathcal{O}(1/N)$ around a discontinuity Tadmor & Tanner [104] have introduced normalization procedures that remove the higher-order moments of the mollifier. As a result, exponential convergence in the pointwise sense is recovered from the Fourier projection sufficiently far from a discontinuity. At a distance of $\mathcal{O}(1/N)$ fourth-order convergence is achieved and at least second-order convergence appears up to the discontinuity. In Ref. [104] an equivalent procedure is developed for the discrete Fourier expansion, with similar convergence results.

In this study the mollification procedure is only applied as a postprocessing tool. A similar approach, although with a Gegenbauer postprocessing tool (see Ref. [36]), is successfully performed by Shu & Wong [99] on development of shocks in the solution of the Burgers equation and also in the 2D Euler equations by Don [28]. It should be emphasized that these are *a posteriori* results due to the lack of full theoretical justification. Gottlieb & Gottlieb [35] explain these results, however, by going back to the argument of Lax [57] on the suitability of Fourier spectral schemes on shock development in nonlinear hyperbolic systems. Nevertheless, it is

not *a priori* known whether postprocessing can successfully recover the solution of the penalized Navier-Stokes equations as well.

Chapter 3

Convergence study of a normal dipole-wall collisionⁱ

A simple two-dimensional vortex-wall collision poses a serious challenge for CFD methods, see, for example, the simulation of the dipole-wall collision with a no-slip wall conducted with both finite differences and Chebyshev spectral methods [18]. In particular, the formation and detachment of very thin boundary layers, containing high-amplitude vorticity, during the collision process and the subsequent formation of small-scale vorticity patches in the near-wall region can possibly deteriorate the accuracy of the flow computation. This dramatically affects the dynamics of the flow after the impact. The initial flow field fulfills the boundary condition (within machine precision no normal and tangential velocities at the no-slip boundaries) such that initialization errors are avoided. The boundary layers are produced during the approach of the dipole to the wall. The production of small-scale vorticity during the vortex-wall interaction makes this process a very good benchmark for many CFD methods aimed at simulation of wall-bounded flows or flows around solid obstacles.

The first numerical investigation of the dipole-wall problem was conducted by Orlandi [80] already a decade ago. Later other studies used the dipole-wall collision experiment to investigate the reliability of several CFD methods. For example, Ould-Salihi [82] *et al.* used this test case to validate particle methods against finite-differences methods. Cottet *et al.* [24, 25] used the dipole-wall collision as a benchmark to validate mesh adaption techniques that allow the use of refined vortex methods in both directions near the wall. Another example, considering a B-spline numerical method, can be found in Kravchenko *et al.* [55]. They analyzed the effect of zonal embedded grids on the evolution of the dipole-wall collision. Clercx & Bruneau [18] provide, on the other hand, a more detailed comparison of

ⁱThe contents of this chapter is an adapted part of Keetels *et al.* [48]

finite differences and a pseudospectral Chebyshev method. It was observed that the dipole-wall problem is an extremely tough test case, *i.e.* the resolution to achieve grid or mode convergence should be substantially larger than considered previously.

3.1 Dipole-wall collision benchmark computation

The numerical simulations of Clercx & Bruneau [18] indicate that it is extremely difficult to obtain mode or grid-convergence for a dipole that collides with a no-slip boundary using a Chebyshev pseudospectral method or finite differences. Here we focus on the convergence properties of a normal dipole-wall collision, *i.e.* the translation of the dipole being perpendicular to the wall, at an integral-scale Reynolds number $Re = \frac{UW}{\nu} = 1000$, based on the total kinetic energy of the flow (determining the average velocity U) and the half width W of the domain. Note that this value of Re is similar as in the 2D decaying turbulence simulations in square bounded domains by Clercx and Nielsen [21]. They used (initial) integral-scale Reynolds numbers varying between 5000 and 20000, but the Reynolds number based on the vortex size in these runs was always in the range 700-2500. Therefore the dipole-wall experiment at $Re = 1000$ can be seen as a novel test case to explore the possibility of pursuing DNS of wall bounded turbulence.

3.1.1 Setup and initial condition

The flow domain Ω_f is defined as,

$$\Omega_f = \{\mathbf{x} \in \mathbb{R}^2 \mid -1 \leq x \leq 1, -1 \leq y \leq 1\}.$$

The initial (scalar) vorticity field ω_0 and velocity field \mathbf{u}_0 should vanish at the boundary, which guarantees absence of artificial boundary layers due to enforcing the no-slip condition at $t = 0$. In order to satisfy these constraints, two equally strong, oppositely signed, isolated monopoles are put close to each other near the centre of the container. The vorticity distribution of the isolated monopoles is chosen as:

$$\omega_0 = \omega_e(1 - (r/r_0)^2)\exp(-(r/r_0)^2), \quad (3.1)$$

with $r = (x^2 + y^2)^{1/2}$ the distance from the centre of the monopole, r_0 its dimensionless 'radius' (at which the vorticity changes sign) and ω_e its dimensionless extremum vorticity value (in $r = 0$). In the present simulations the exact numerical value for the radius of the monopoles is $r_0 = 0.1$, and $\omega_e = 299.528385375226$. With this value of r_0 the vorticity at the boundary (at $r \approx 1$) is virtually zero, as can be concluded by substituting the numerical value of the ratio r/r_0 in Eq.

(3.1).

This value of ω_e is determined by the condition that the total kinetic energy of the dipolar flow field,

$$E(t) = \frac{1}{2} \int_{-1}^1 \int_{-1}^1 \mathbf{u}^2(\mathbf{x}, t) dx dy , \quad (3.2)$$

is normalized to $E(0) = 2$ for all runs. As a consequence, both U and the half-width of the domain W are fixed and the Reynolds number is defined as $\text{Re} = UW/\nu$. The total enstrophy of the dipolar flow field is defined by,

$$Z(t) = \frac{1}{2} \int_{-1}^1 \int_{-1}^1 \omega^2(\mathbf{x}, t) dx dy , \quad (3.3)$$

with $Z(0) \approx 800$. The exact numerical values for the initial position of the two isolated monopoles is $\{(x_1, y_1), (x_2, y_2)\} = \{(0, 0.1), (0, -0.1)\}$. The initial condition $\mathbf{u}_0 = (u_0, v_0)$ for the integration of the Navier-Stokes equations in primitive variables can be derived straightforwardly for a couple of isolated monopoles, satisfying Eq. (3.1) and is then given by :

$$\begin{aligned} u_0 &= -\frac{1}{2}|\omega_e|(y - y_1)\exp(-(r_1/r_0)^2) + \frac{1}{2}|\omega_e|(y - y_2)\exp(-(r_2/r_0)^2) \\ v_0 &= \frac{1}{2}|\omega_e|(x - x_1)\exp(-(r_1/r_0)^2) - \frac{1}{2}|\omega_e|(x - x_2)\exp(-(r_2/r_0)^2) , \end{aligned} \quad (3.4)$$

with $r_1^2 = (x - x_1)^2 + (y - y_1)^2$ and $r_2^2 = (x - x_2)^2 + (y - y_2)^2$. This initial condition also proves that the no-slip condition is sufficiently well guaranteed by our choice $r_0 = 0.1$ (note that $e^{-(r/r_0)^2} \approx e^{-100} \approx 10^{-44}$).

3.1.2 Chebyshev-Fourier and Chebyshev benchmark computations

Figure 1.4 gives an overview of the normal dipole-wall collision obtained by a Chebyshev-Fourier benchmark computation, using 1024 Chebyshev modes and 2048 active Fourier modes with a time step $\delta t = 10^{-5}$. It is found by Clercx and Bruneau [18] that an extremely fine discretization is required for accurate quantitative results. Especially for simulations with long integration times compared with the time t_1 of the primary collision. In particular underresolved high-amplitude vorticity patches near the no-slip wall (visible in Fig. 1.4) can possibly deteriorate the accuracy in course of time.

To analyze the quality of the Chebyshev and Chebyshev-Fourier computations we analyze the relative error in the vorticity

$$\delta_N = \frac{\| \omega(N) - \omega(N_{\max}) \|_{L^2}}{\| \omega(N_{\max}) \|_{L^\infty}} , \quad (3.5)$$

where $\omega(N)$ is the approximation of the vorticity with resolution N and N_{\max} is the maximum N that is available. The highest-resolution computations that are

performed for the square bounded domain have 640 Chebyshev modes in both directions. For the periodic channel domain a maximum of 1024 Chebyshev modes for the non-periodic direction and 2048 active Fourier modes is used for the periodic direction. To estimate the error of the computations lower resolution computations are performed as well. For the square bounded case a second computation is conducted with 512 Chebyshev modes in both directions and the periodic channel with 512 Chebyshev modes versus 1024 active Fourier modes. The time step is fixed for all computations, *i.e.*, $\delta t = 10^{-5}$. It is found that the truncation error δ_N is less than 1.2×10^{-4} for the square bounded case. Clercx & Bruneau [18] have shown that the truncation error of the Chebyshev scheme decays exponentially with N . They considered the dipole-wall experiment for $Re = 1250$ and $N_{\max} = 512$ in both directions. The order of magnitude of the truncation error observed here for $Re = 1000$ and $N_{\max} = 640$ is consistent with the results of Clercx & Bruneau [18]. The error δ_N for the periodic channel geometry is less than 8.2×10^{-5} for $t \leq 2.0$. Therefore, the high-resolution computations in both geometries can be considered as sufficiently accurate benchmark computations.

3.2 Convergence analysis of Fourier schemes

To simulate the dipole-wall collision with volume-penalization the flow domain Ω_f defined in Section 2.2.1 is embedded in the channel geometry of Fig. 2.1b. The computational domain Ω is defined as

$$\Omega = \{ \mathbf{x} \in \mathbb{R}^2 \mid -1 \leq x \leq 1, -(1 + \delta_w) \leq y \leq (1 + \delta_w) \}, \quad (3.6)$$

where the wall thickness δ_w is chosen such that there is a set of grid points on the interface between the fluid and the solid (porous) material. It is found that decreasing δ_w from ten percent down to one percent of the channel width does not change the computational result significantly. To reduce the number of gridpoints inside Ω_s as much as possible the wall thickness δ_w is fixed to about one percent of the domain size for the Fourier spectral simulations presented here.

Due to the continuity restrictions of the solution of the penalized Navier-Stokes equations (see section 2.2.2) on $\partial\Omega_f$ it can be expected that the Fourier projections of the different flow variables will suffer from the Gibbs phenomenon. The key question is, however, whether the low convergence rate of the Fourier projection will in addition prevent proper convergence of the Fourier spectral scheme or that higher-order accuracy can be recovered by the mollification technique proposed by Tadmor & Tanner [104] (or alternative techniques such as high-wavenumber filtering [68] and Gegenbauer postprocessing [37]).

3.2.1 Gibbs oscillations

Fig. 3.1 presents the isolines of the vorticity obtained by the Fourier spectral solver with 1364 active Fourier modes in both directions using $\epsilon = 2.5 \times 10^{-5}$ and implicit treatment of the Darcy drag with a time step of $\delta t = 10^{-5}$. As the

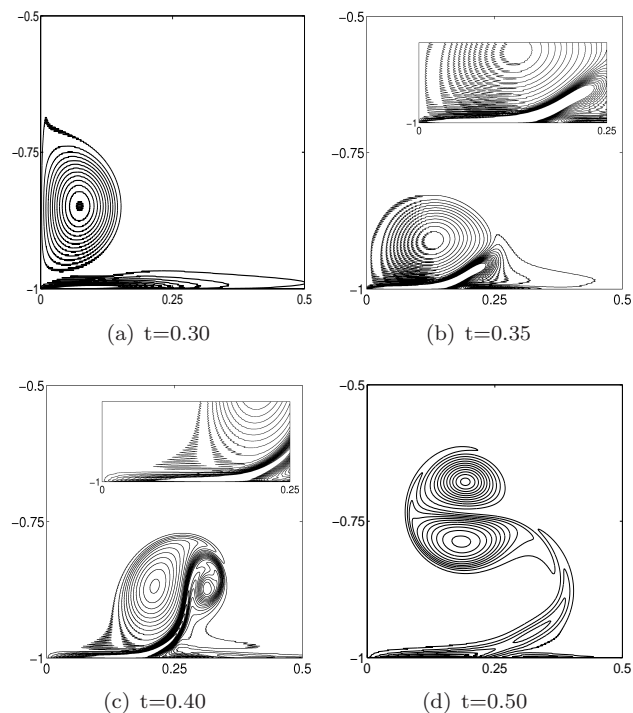


Figure 3.1 – Contour plots of the vorticity field of a normal dipole-wall collision with $Re = 1000$ using 1364×1364 active Fourier modes, $\delta t = 10^{-5}$ and $\epsilon = 2.5 \times 10^{-5}$ with an implicit scheme. Contour levels are drawn for $-270, -50, -30, -10, 10, 30, 50, \dots, 270$.

dipole impinges the wall strong oscillations in the vorticity isolines become indeed apparent, as is evident from Fig. 3.1. Note that only one half of the domain is shown because of the symmetry of a normal dipole-wall collision. The oscillations are more pronounced near the wall than in the interior of the flow domain. An important observation is that the wiggles automatically disappear as the vortex moves into the interior of the flow domain, $t = 0.5$ in Fig. 3.1d. In addition Fig. 3.2 shows the mollified results obtained by the recovery method of Tadmor & Tanner [104] applied to the computational output presented in Fig. 3.1. It reveals strong correspondence with the Chebyshev-Fourier benchmark computations. This indicates that the observed oscillations do not have a serious dynamical effect on the evolution of the dipole-wall collision.

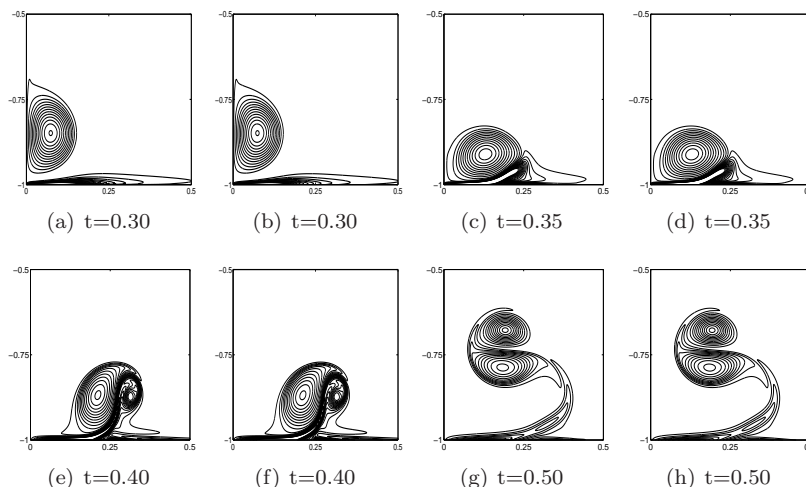


Figure 3.2 – Contour plots of the vorticity of a normal dipole-wall collision with $Re = 1000$. Panels (a,c,e,g) show mollified Fourier projection using 1364×1364 active Fourier modes, $\delta t = 10^{-5}$ and $\epsilon = 2.5 \times 10^{-5}$ with an implicit treatment of Darcy drag. Panels (b,d,f,h) show the Chebyshev-Fourier benchmark computation with 1024 Chebyshev modes and 2048 Fourier modes. Contour levels are drawn for $-270, -50, -30, -10, 10, 30, 50, \dots, 270$.

3.2.2 Truncation error

In order to investigate the scaling behaviour of the truncation error the simulations are compared with the highest available resolution of 2730×2730 active number of Fourier modes (computed with 4096×4096 Fourier modes to prevent aliasing errors), while the penalization parameter is fixed for all computations at a value of $\epsilon = 2.5 \times 10^{-5}$. This value is chosen such that it is feasible to test both the implicit and explicit implementation of the Darcy drag efficiently. Note that for the explicit implementation the time step has to be in the same order as the penalization parameter. As a consequence, a smaller value for ϵ would result in a blow-up of the amount of wall-clock time. On the other hand, $\epsilon = 2.5 \times 10^{-5}$ is small enough to have an acceptable correspondence with the Chebyshev-Fourier benchmark computation, which satisfy the no-slip condition within machine-precision accuracy. The mollification procedure of Tadmor and Tanner [104] involves a symmetric mollifier that gives second order accuracy in the immediate vicinity of a discontinuity (the wall in this case) and higher-order accuracy when moving away from the discontinuity. Therefore, we decompose the domain in an interior part Ω_{int} ranging from $x = [-0.99, 0.99]$ and $y = [-0.99, 0.99]$ and a boundary zone. Only in the interior part high-order recovery of the Fourier projection can be expected for all the resolutions considered here. Fig. 3.3 demonstrates the convergence behaviour in the boundary zone. A cross-section of the viscous boundary is presented at the

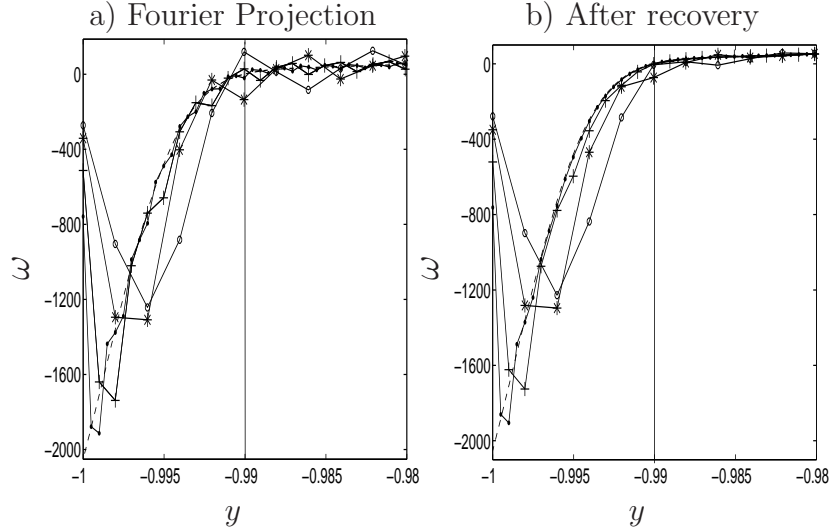


Figure 3.3 – Cross-section of the vorticity along the line $x = 0.083$ at $t = 0.35$, Chebyshev-Fourier benchmark result (dashed) and implicit scheme (solid). $\delta t = 10^{-5}$, $\epsilon = 2.5 \times 10^{-5}$, with different number of active Fourier modes: 512^2 (open circles), 682^2 (stars), 1364^2 (plus signs) and 2730^2 (closed circles).

point where the vorticity on the wall has a maximum. Fig. 3.3a shows that the amplitude of the oscillations in the Fourier projection decreases slowly by increasing the resolution. The vorticity value on the wall reflects a well-known convergence property of Fourier series

$$\lim_{N \rightarrow \infty} \omega_N(x) = \frac{\omega(x_-) + \omega(x_+)}{2} \quad (3.7)$$

where x_- and x_+ denote the limits from below and above x , respectively. Since the vorticity inside the obstacle is negligible (see section 2.2.2) the projection ω_N underpredicts the vorticity on the wall by a factor two. Recall that C^0 continuity of the vorticity is enforced by an asymptotically thin boundary layer inside the obstacle proportional to $\sqrt{\nu\epsilon}$. The resolution of the computations is, however, too low to resolve this boundary layer.

The recovered Fourier projection in Fig. 3.3b converges smoothly towards the benchmark computation. Note that this reflects that both the quality of the computation and the accuracy of the postprocessing improve with N .

The convergence in the interior is analyzed by considering the error

$$\delta_N = \frac{\|\omega_N - \omega_{2730}\|_{L^2(\Omega_{int})}}{\|\omega_{2730}\|_{L^\infty(\Omega_f)}} \quad (3.8)$$

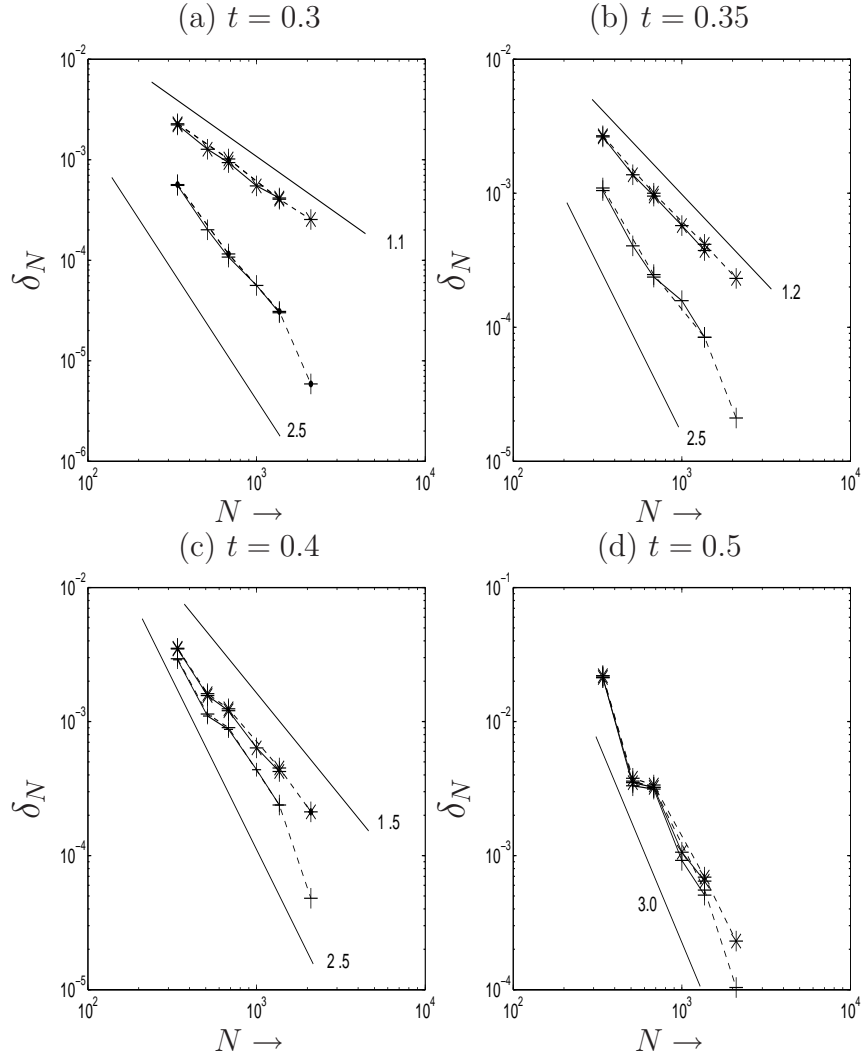


Figure 3.4 – Truncation error δ_N versus number of active Fourier modes N . Explicit (solid) and implicit (dashed) implementation of Darcy drag. The error of the Fourier projection (stars) and the mollified result (plus signs).

where N represents the simulations conducted with less than 2730 active Fourier modes in both directions. The time step is fixed for all computations, *i.e.*, $\delta t = 10^{-5}$ consistent with the CFL condition of the high-resolution computation with 2730×2730 active Fourier modes. The convergence rate of the Fourier projection

presented in Fig. 3.4 depends on the time considered. During the collision process, in particular at $t = 0.3$, $t = 0.35$ and $t = 0.4$, the error of the Fourier projection only shows first order decay, while at some later time, for example, $t = 0.5$ the error decays faster. The error of the mollified vorticity fields shows, however, fast decay at least proportional to $N^{-2.5}$ for all times. From these observations it is difficult to determine the exact value for the order of the scheme. Especially, because it is not sure how the mollified error is behaving with either a specific power law or exponentially. Note that the slope increases when moving towards the higher end of the spectral range considered here. This might indicate that the error of the postprocessed results behaves exponentially or that higher-order convergence appears after reaching a specific resolution related to the thickness of the viscous boundary layer. At $t = 0.5$ the mollification procedure does not improve the scaling of the truncation error, which can be related to absence of strong oscillations in the vorticity isolines in Fig. 3.1d. The schemes of section 2.3.1 and 2.3.2 with an explicit and implicit treatment of the Darcy drag respectively, show a similar decay of the truncation error as can be deduced from Fig. 3.4.

3.2.3 Long-time integrations and global quantities

Some additional convergence results are presented in Fig. 3.5, concerning the total kinetic energy and total enstrophy of the flow. The computation with penalization parameter $\epsilon = 10^{-3}$ and $N = 682$ active Fourier modes shows a stronger decay of the total kinetic energy, while the total enstrophy is strongly underestimated. Setting $\epsilon = 10^{-8}$ and $N = 2730$ yields a curve $E(t)$ that is on top of the benchmark computation. The curve $Z(t)$ of the total enstrophy coincides with the benchmark almost everywhere, but slightly underpredicts the maximum value of the enstrophy at $t = 0.35$. About 90% of the enstrophy is contained in the boundary layer, as shown in the cross-sectional plots in Fig. 3.3, especially the values on the wall itself strongly contribute to the total enstrophy. Unfortunately, we are not able to reconstruct the vorticity in the immediate vicinity of the wall and on the wall itself (see Fig. 3.3). This explains why the maximum enstrophy is slightly underestimated (a deviation of approximately 1%). If, however, the vorticity value on the wall is corrected with a factor two related to the convergence property (3.7) the error becomes less than 3.0×10^{-3} .

As reported by Clercx and Bruneau [18] especially long-time integrations beyond the first dipole-wall collision are difficult to resolve properly. In Fig. 3.6 the vorticity isolines are shown for a long-time integration using $N = 1364$ active Fourier modes, a penalization parameter $\epsilon = 10^{-8}$ and a time step $\delta t = 10^{-5}$. It clearly shows that convergence can be achieved as well for long-time integrations by setting the resolution and penalization parameter appropriately. Furthermore, the larger time integrations support the observation that Gibbs oscillations do not trigger any significant dynamical effects.

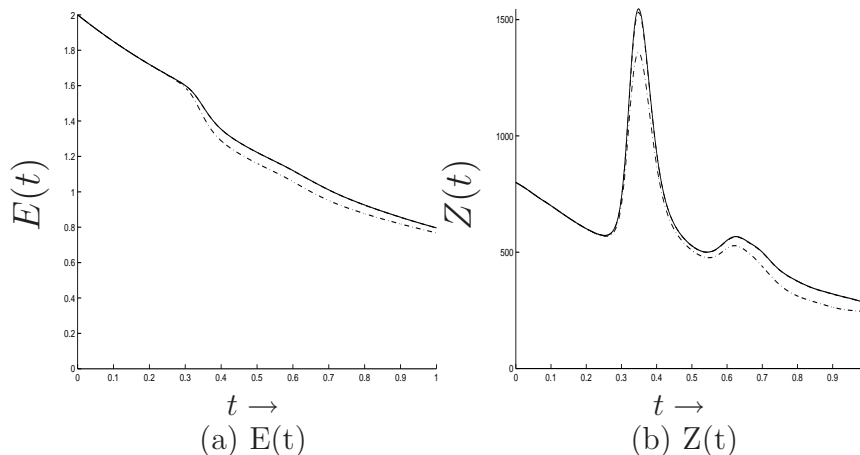


Figure 3.5 – Total kinetic energy $E(t)$ and enstrophy $Z(t)$ of a computation with setting $\epsilon = 10^{-3}$, $N = 682$, $\delta t = 10^{-5}$ (dashed-dot) and $\epsilon = 10^{-8}$, $N = 2730$, $\delta t = 10^{-5}$ compared with Chebyshev-Fourier benchmark computation (solid).

3.3 Convergence analysis of Coherent Vortex Simulation (CVS)

In the following we present results of coherent vortex simulations using the adaptive wavelet method ([95], [94], [93], [98]) presented in subsection 2.3.3. The CVS simulations are conducted in the square bounded geometry, see Fig. 2.1c, the wall thickness $\delta_w = 0.1$ for all four side walls (note that $\Omega_f = [-1, 1] \times [-1, 1]$).

First we inspect the vorticity isolines computed with CVS versus a high-resolution Chebyshev computation. Then we consider the compression rate of the degrees of freedom by the Coherent Vortex Simulation method. In addition we analyze the scaling behaviour of the discretization error using different resolutions (128^2 , 256^2 , 512^2 and 1024^2) for the CVS computations. Finally it is checked if it is possible to further reduce the number of wavelet coefficients by varying the threshold $\tilde{\epsilon}_0$ while keeping the number of grid points fixed.

3.3.1 Visualization

Fig. 3.7 visualizes the isolines of vorticity at $t = 0.4$ for a CVS computation using 1024^2 gridpoints and a time step $\delta t = 5 \times 10^{-5}$ compared to a Chebyshev benchmark result with 640 Chebyshev modes in both directions using a time step $\delta t = 1.25 \times 10^{-5}$. Although both simulations yield isolines which are very close to each other, the symmetry around the y -axis is slightly broken in the CVS computation: a magnification of the left dipole half yields almost coinciding isolines,

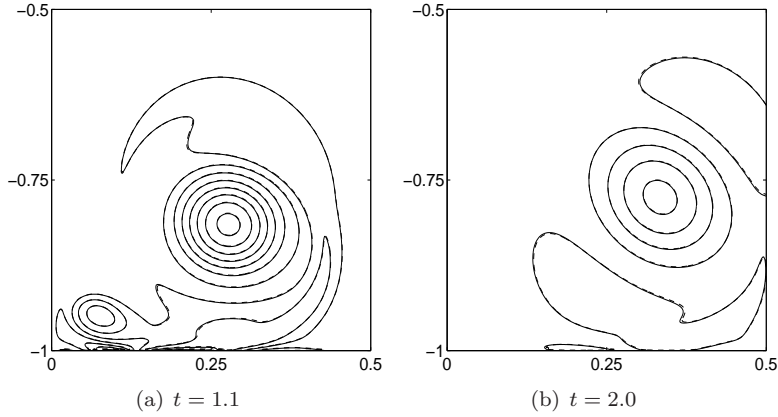


Figure 3.6 – Contour plots (dashed) of the vorticity for $\epsilon = 10^{-8}$ with 1364×1364 active Fourier modes and Chebyshev-Fourier benchmark computation (solid). Contour levels are drawn for $\dots, -50, -30, -10, 10, 30, 50, \dots$

while a magnification of the other half in Fig. 3.7b visualizes some small deviations of the isolines compared to the Chebyshev benchmark computation.

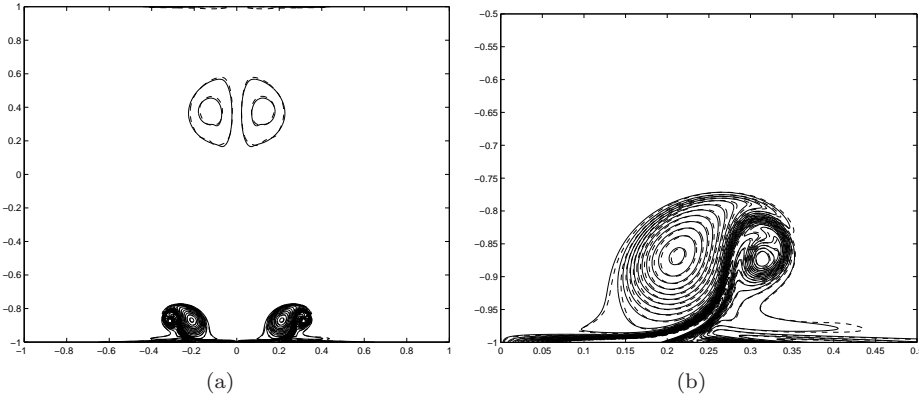


Figure 3.7 – Isolines (dashed) of ω drawn for $-270, \dots, -50, -30, -10, 10, 30, 50, \dots, 270$, comparison of CVS simulation on 1024^2 grid and $\delta t = 5 \times 10^{-5}$, with the Chebyshev run with 640^2 modes and $\delta t = 1.25 \times 10^{-5}$ (solid) at $t = 0.4$. Left: total domain. Right: Zoom in.

Although the wavelet discretization is symmetric on a regular grid, the applied thresholding introduces some slight asymmetry on the locally refined grid, which is not perfectly symmetric (cf. Fig. 3.8). Focussing on the vorticity isolines of the secondary vortex pair moving to the top of the domain it is seen in Fig. 3.7a that they differ slightly from the benchmark computation. This can be explained by

the filtering effect of CVS. In each time step weak wavelet coefficients are filtered out, which correspond to weak vorticity contributions. As the secondary vortex pair contains much less enstrophy than the primary one it is more affected by the CVS filtering. We find that the CVS-1024 result exhibits no Gibbs oscillations like the Fourier computations. Therefore we decided not to apply any postprocessing to the CVS results.

3.3.2 Grid adaptation

To illustrate the dynamical adaption strategy of the CVS computations we plot in Fig. 3.8 the locally refined grids at different instants, $t = 0.1, 0.2, 0.3$ and 0.4 . The computation has been performed with a maximum of $J = 10$ available scales,

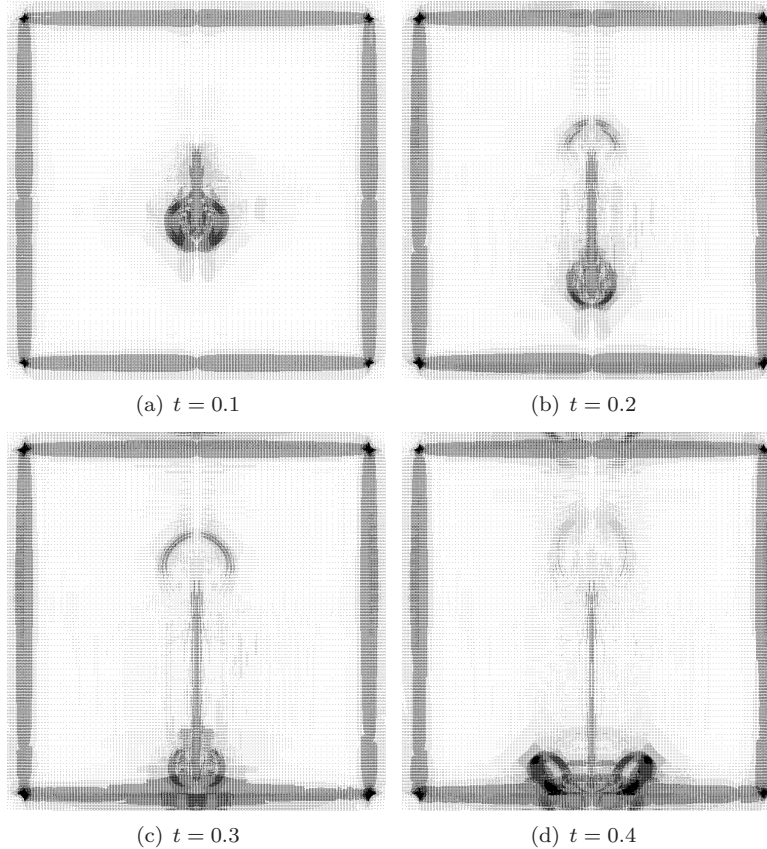


Figure 3.8 – Adaptive grid at $t = 0.1, 0.2, 0.3$ and 0.4 for CVS computation with 1024 grid points in both directions. The number of wavelets are 93 674, 104 711, 112 065 and 124 364 for $t = 0.1, 0.2, 0.3$ and 0.4 , respectively.

corresponding to a maximum number of 1024^2 unknowns, a fixed time step of $\delta t = 5 \times 10^{-5}$ and a threshold value of $\tilde{\varepsilon}_0 = 10^{-5}$. The penalization parameter was chosen as $\epsilon = 10^{-4}$. Note that without penalization the time step is only limited by the CFL-condition, which would allow a larger time step of $\delta t = 5 \times 10^{-4}$ for the CVS computations up to 1024^2 grid points. Unfortunately, the explicit treatment of Darcy drag constitutes a restriction on the time step required for stable second-order time integration. In Fig. 3.8 we observe that the grid automatically tracks the time evolution of the dipole. In regions of strong gradients we find fine grid spacing

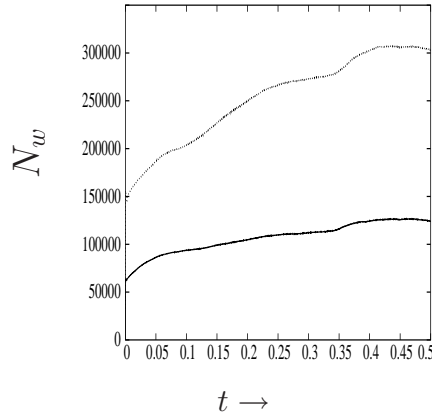


Figure 3.9 – Time evolution of the number of wavelet coefficients N_w with (dots) and without (solid) security zone for CVS computation on 1024^2 grid with $\delta t = 5 \times 10^{-5}$.

while in quiescent regions the grid is coarsened. At the boundary of the domain, *i.e.* at the interface between the penalized region and the fluid domain, the grid is also refined to be able to resolve the strong gradients of vorticity. The finest scale $J = 10$ present in the CVS-1024 computation corresponds to the total number of wavelet modes N of $2^{2J} = 1024^2 = 1,048,576$. The time evolution of the number of active wavelet modes N_w for the CVS-1024 run, with and without the security zone (cf. subsection 2.3.3), is depicted in Fig. 3.9. Both numbers are increasing also after the first collision. This can be explained by the choice (2.26) for the threshold $\tilde{\varepsilon}$. The threshold decreases with the total enstrophy retaining more modes in the computation. At $t = 0.1, 0.2, 0.3$ and 0.4 the computation (without security zone) uses 93,674, 104,711, 112,065 and 124,364 wavelet modes, respectively, *i.e.* less than 12% of the total number of modes. A comparison of the total kinetic energy and enstrophy evolution of the CVS-1024 run with the Chebyshev benchmark with 640 Chebyshev modes in both directions is given in Fig. 3.10. It shows that the CVS computation closely follows the reference Chebyshev computation. Both

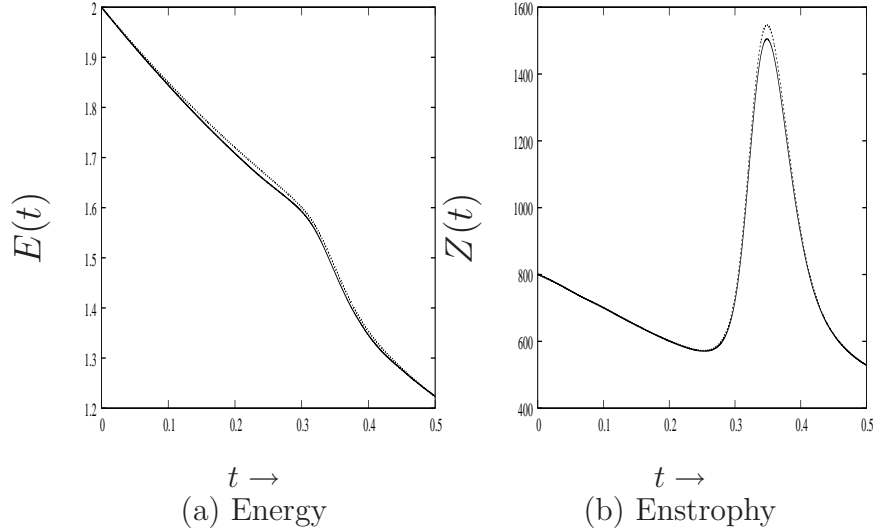


Figure 3.10 – Comparison of $E(t)$ (a) and $Z(t)$ (b) between the CVS run on 1024^2 -grid, $\delta t = 5 \times 10^{-5}$, and penalization parameter $\epsilon = 10^{-4}$ (solid) and the Chebyshev run with 640^2 modes (dots) and $\delta t = 1.25 \times 10^{-5}$.

total kinetic energy and enstrophy of the CVS computation are slightly below the reference run. To quantify the errors between the two methods we compute the relative maximum error for the energy, $\max|(E(t) - E^{cvs}(t))/E(t)|$, and for the enstrophy $\max|(Z(t) - Z^{cvs}(t))/Z(t)|$. For the former we find a value below 0.8% while the latter is below 2.8%. Note that the computed error is the sum of the discretization and penalization error (Gibbs oscillations are not present in the CVS runs).

The time evolution of the wavelet modes for CVS computations with $N = 256^2$, $N = 512^2$ and $N = 1024^2$ grid points with a fixed time step $\delta t = 5 \times 10^{-5}$ is shown in Fig. 3.11. The compression rate improves with increasing resolution. For 256^2 almost all the coefficients (including security zone) are used at $t = 0.5$ (about 90%), while for 1024^2 less than 30% are used.

3.3.3 Error analysis

To quantify the error of the CVS computations Fig. 3.12a shows a double-logarithmic graph of the normalized error in the vorticity (3.8) of (i) the CVS computations with respect to the Chebyshev-640 reference computation and (ii) with respect to the CVS computation on the finest grid with 1024^2 grid points. Both curves show a power law behaviour with a slope of 1.47. In Fig. 3.12b a cross-section of the viscous boundary layer is shown at $t = 0.35$ along a line $x = 0.083$. From

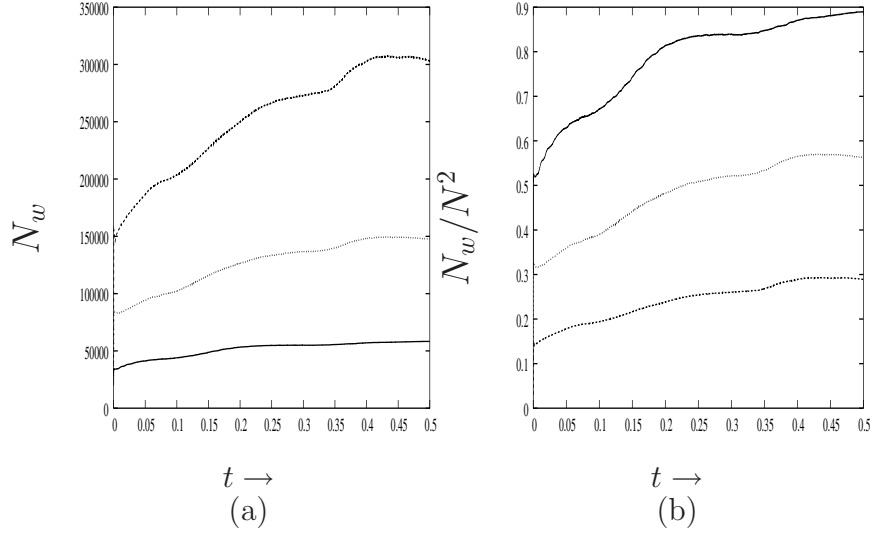


Figure 3.11 – Time evolution of the (a) number of wavelet coefficients N_w with security zone and (b) number of wavelet coefficients normalized with total number of grid points N for the CVS 256^2 grid points (solid) and $\delta t = 10^{-4}$, 512^2 grid points and $\delta t = 10^{-4}$ (dots) and 1024^2 grid with $\delta t = 5 \times 10^{-5}$ (dashed) runs.

this figure it can be deduced that the CVS result with 1024^2 -grid is capable of capturing the vorticity profile of the viscous boundary layer reasonably well. The behaviour on the wall itself is not a result of the Gibbs effect. It is a result of the implementation of the mask function in the CVS computations, which does not guarantee that there is a set of grid points on the wall at $y = -1$. The vorticity at the grid points inside the obstacle $y < -1$ is approximately zero. Recall that the solution of the penalized Navier-Stokes equation inside the obstacle can be described by Darcy flow, which has no rotation. As a consequence, there is no vorticity inside the obstacle. Interpolation between the grid point inside the obstacle and in the flow gives a wiggle near the wall at $y = -1$ in Fig. 3.12b. From the fit in Fig. 3.12a we could deduce that the CVS method is of order 1.5 (in terms of vorticity), which is similar to the order of the Fourier spectral schemes without postprocessing. However, we should be careful with this conclusion, because the measurements are obtained in the regime where the number of grid points inside the viscous boundary layer is less than four. Here, the boundary-layer thickness δ based on the ratio of vorticity and vorticity gradients on the wall is defined as $\delta \approx \frac{1}{4\sqrt{Re}}$, see Ref. [18]. Hence, it cannot be ruled out that finer grid computations would yield different scaling behaviour of the error, especially beyond a critical grid size that is proportional to the boundary-layer thickness. Unfortunately, higher-resolution computations are not yet feasible, because the current code does not

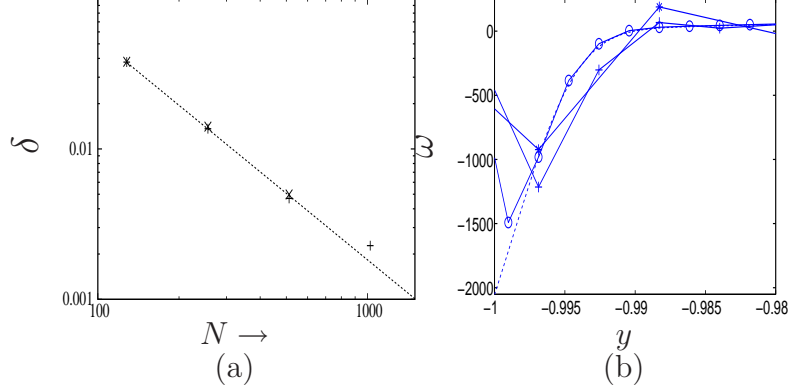


Figure 3.12 – Panel (a) shows the normalized L_2 -error in the vorticity δ versus Chebyshev benchmark with 640^2 modes and $\delta t = 1.25 \times 10^{-5}$ (+) and the error with respect to the CVS computation on 1024^2 grid with time-step $\delta t = 5 \times 10^{-5}$ and $\epsilon = 10^{-4}$ (x) and the power law $47.05N^{-1.47}$ (dashed) obtained fitting the (+). Panel (b) shows the cross section of the vorticity similar along the line $x=0.083$ at $t = 0.35$ (see Fig. 6) using different grids 256^2 (stars), 512^2 (plus signs) and 1024^2 (open circles) and benchmark computation using 640 Chebyshev modes in both directions and $\delta t = 1.25 \times 10^{-5}$ (dashed).

run in parallel. On the other hand, Clercx & Bruneau [18] found that about five grid points inside the boundary layer are necessary to achieve grid-convergence for the normal dipole-wall collision experiment with a second-order (in velocity) finite-difference scheme. Considering the decay rate of the error in the vorticity we expect that grid-convergence is achieved for the CVS-1024 computation.

3.3.4 Penalization parameter and reduction of wavelet coefficients

Different CVS computations have been performed to check the influence of the penalization parameter ϵ and of the threshold $\tilde{\epsilon}_0$ of the wavelet coefficients. In Fig. 3.13a we plot the time evolution of the enstrophy for CVS-512 using three different values of the penalization parameter ϵ . The amount of enstrophy production on the wall increases significantly with the penalization parameter in the range $\epsilon = 10^{-2}$ to $\epsilon = 10^{-4}$. For the penalization parameter $\epsilon = 10^{-2}$, the accuracy becomes extremely poor, as can be seen in Fig. 3.13a. A second set of simulations is conducted to analyze the effect of $\tilde{\epsilon}_0$ on the enstrophy production. It is found that in the range $\tilde{\epsilon}_0 = 10^{-4}$ to $\tilde{\epsilon}_0 = 10^{-6}$ the maximal difference in $Z(t)$ lies within machine precision. However, the number of wavelet coefficients used in the $\tilde{\epsilon}_0 = 10^{-4}$ run is two times smaller than in the $\tilde{\epsilon}_0 = 10^{-6}$ computation, which

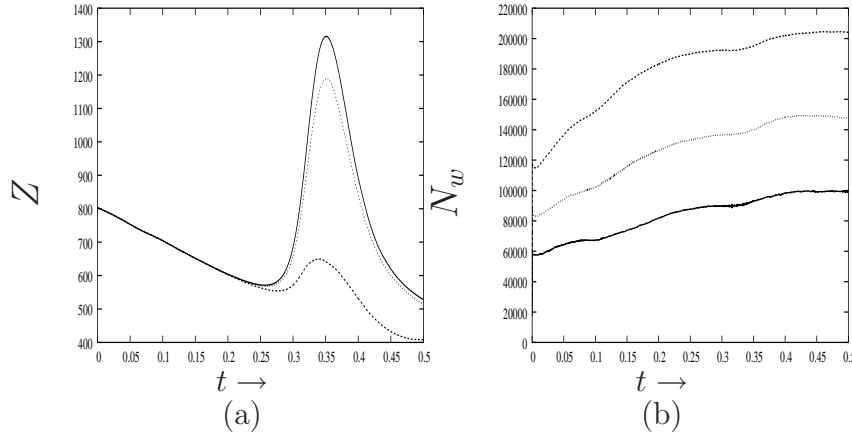


Figure 3.13 – Enstrophy versus time for three different values of the penalization parameter $\epsilon = 10^{-2}$ (dashed), $\epsilon = 10^{-3}$ (dots) and $\epsilon = 10^{-4}$ (solid), threshold $\tilde{\epsilon}_0 = 10^{-5}$ is fixed (a). Number of wavelet coefficients N_w with security zone for three different values of the threshold $\tilde{\epsilon}_0 = 10^{-4}$, $\tilde{\epsilon}_0 = 10^{-5}$ and $\tilde{\epsilon}_0 = 10^{-6}$ with penalization parameter $\epsilon = 10^{-4}$ fixed (b).

can be deduced from Fig. 3.13b. As the computing time is linear with the number of wavelet modes used, for the same accuracy, a speed-up by a factor two can be obtained.

3.4 Penalization error

In this section we focus on the penalization error δ_ϵ corresponding to the differences between the solution of the Navier-Stokes equations with no-slip boundary condition and the solution of the penalized Navier-Stokes equations. The challenge is to find a balance between the truncation and the penalization error by an optimal choice for ϵ for every N . Fig. 3.14 shows the vorticity isolines of runs where both the penalization parameter ranges from $\epsilon = 10^{-3}$ to $\epsilon = 10^{-8}$ and the number of active Fourier modes from $N = 682$ to $N = 2730$. The combination of penalization parameter and number of active Fourier modes is chosen such that an optimal setting is achieved, *i.e.*, increasing N does not improve the accuracy significantly. The largest value of the penalization parameter, $\epsilon = 10^{-3}$, yields a slightly different vortex path compared with the benchmark computation. Especially after the second collision at $t = 0.8$ it is seen that the secondary vortex core is not strong enough to bend the vortex system sufficiently outward (see Fig. 3.14a). This might be related to the amount of vorticity that is produced on the wall and in addition advected into the interior. As the penalization parameter is decreased, more vorticity is produced on the wall such that the resulting secondary

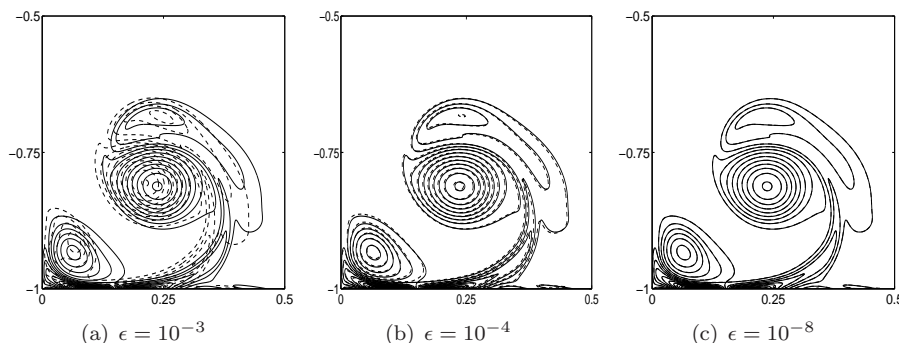


Figure 3.14 – Contour plots (dashed) of the vorticity after the second collision at $t = 0.8$ for different values of the penalization parameter ϵ with respect to the benchmark simulation (solid). Contour levels are drawn for $-270, -250, \dots, -50, -30, -10, 10, 30, 50, \dots, 250, 270$. Number of active Fourier modes 682^2 (a), 1364^2 (b) and 2730^2 (c), time-step is fixed to $\delta t = 10^{-5}$.

vortex becomes stronger, finally resulting in acceptable converged vorticity isolines. Fig. 3.15a shows the total error δ_{tot} , which is the sum of the truncation error δ_N and the penalization error δ_ϵ . It is calculated by using the high-resolution Chebyshev-Fourier benchmark computation with 1024 Chebyshev modes in the wall direction and 2048 Fourier modes in the periodic channel direction. As can be deduced from Fig. 3.15a it is possible to improve the decay rate of the total error versus N by taking sufficiently small values for the penalization parameter. For every ϵ a saturation level emerges at a specific N , *e.g.* for $\epsilon = 10^{-4}$ at $N \approx 1000$. From the saturation levels in the total error it is possible to obtain an estimate for the penalization error. Note that at the saturation level it can be assumed that the truncation error is no longer leading in the total error. The corresponding estimates for the penalization error are presented in Fig. 3.15b. The decay rate of the penalization error is consistent with the theoretical bound proportional to $\sqrt{\epsilon}$ from Carbou & Fabrie [14]. Actually the error scales slightly better, proportional to $\epsilon^{0.7}$. Note that in the simulations the asymptotic boundary layer inside the wall is not resolved properly since $\sqrt{\nu\epsilon} < 2/N$. This confirms our expectation in section (2.2.2) that without resolving the penalization boundary layer a $\sqrt{\epsilon}$ accuracy bound is still achievable.

Now it is possible to derive an optimal choice for the penalization parameter ϵ versus N . Recall that the minimal decay rate of the truncation error of the Fourier methods is $\delta_N = \alpha N^{-2.5}$, with constant $\alpha \approx 1.0 \times 10^4$. The penalization error scales as $\delta_\epsilon = \beta \epsilon^{0.7}$ with $\beta \approx 1$ optimum is thus achieved when $\delta_N = \delta_\epsilon$ and one readily obtains

$$\epsilon = \left(\frac{\alpha}{\beta}\right)^{10/7} N^{-3.6} \approx \gamma N^{-3.6},$$

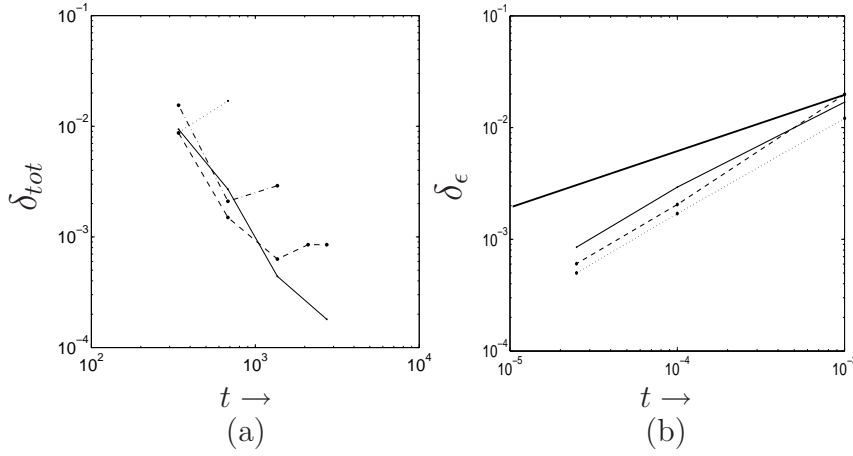


Figure 3.15 – Total error δ_{totot} versus number of Fourier modes N at $t = 0.8$, $\epsilon = 10^{-3}$ (dots), $\epsilon = 10^{-4}$ (dashed-dot), $\epsilon = 2.5 \times 10^{-5}$ (dashed) and $\epsilon = 10^{-8}$ (solid) (a). Modelling error versus ϵ computed at $t = 0.4$ (dots), $t = 0.5$ (dashed) and $t = 0.8$ (solid) and theoretical upper bound (b).

where γ is an $\mathcal{O}(10^5)$ constant. The same approach for the CVS method with $\delta_N = \alpha N^{-1.5}$ with $\alpha \approx 50$ yields an optimum

$$\epsilon = \left(\frac{\alpha}{\beta}\right)^{10/7} N^{-2.1} \approx \gamma N^{-2.1},$$

with γ in the order of 10^2 .

3.5 Conclusions and discussion

Based on a difficult test case of a dipole-wall collision we conclude that the penalized Navier-Stokes equations at high-Reynolds numbers can be solved accurately by Fourier spectral methods and coherent vortex simulation. Gibbs oscillations are present in the Fourier spectral schemes due to continuity restrictions, which results in a slow decay of the truncation error. This does, however, not affect the stability such that it is not necessary to introduce any artificial viscosity terms to enhance the stability of the scheme (Ref. [35]). Furthermore, higher-order recovery of the solution can be achieved by the mollification technique proposed by Tadmor and Tanner [104]. It is very likely that similar results can be achieved by other recovery procedures like, for example, Gegenbauer postprocessing (Ref. [44], [35], [36]). The Petrov-Galerkin discretization used in CVS with quintic splines as a trial basis avoids the Gibbs effect such that mollification is not necessary. We found that the degrees of freedom using a grid-adaptive strategy can seriously be reduced for this

particular problem, at least by a factor 1/8, without a significant loss of accuracy.

The penalization error corresponding to the difference between the solution of the penalized Navier-Stokes equations and the solution of the Navier-Stokes equations with no-slip boundary condition can be controlled by choosing appropriate values of the penalization parameter. Furthermore, the theoretical error bound of $\sqrt{\epsilon}$ obtained by Carbou & Fabrie [14] is confirmed. We found that it is not necessary to resolve the asymptotic boundary layer with a thickness proportional to $\sqrt{\nu\epsilon}$, such that an extreme refinement of the grid inside the obstacle can be avoided. This can be expected because only the order ϵ and higher order asymptotic expansions of Carbou & Fabrie [14] rely on the boundary layer solutions. For an optimal convergence scenario one has to find a balance between the truncation and penalization error. Therefore the penalization parameter must be reduced for increasing resolutions $\epsilon \propto N^{-3.6}$. As a consequence it makes sense to decouple the time step proportional to N^{-1} from the penalization parameter. Kevlahan & Ghidaglia [51] used a GMRES Krylov subspace technique in an explicit time-scheme for this purpose. As an alternative we propose an implicit treatment of the Darcy drag in a Fourier collocation scheme yielding good convergence results with respect to the truncation and penalization error.

Clercx & Bruneau [18] consider different important quantities of the dipole-wall collision problem, like for example the location and magnitude of the primary vortex cores, the collision time of the first and second collision, vortex-trajectories, vorticity on the wall, one-dimensional Chebyshev spectra and the pressure inside the cores of the vortices. Here we studied the convergence in terms of the global L_2 -error. It is, however, verified that convergence is achieved in terms of several of the quantities mentioned above, like the magnitude and location of both the primary and secondary vortex cores and the collision time. The computations of Clercx & Bruneau are conducted in the square bounded geometry. It is observed here that there is no significant difference between the simulations of the normal-dipole wall collision in the channel geometry or the square geometry. Clercx & Bruneau increase the initial Reynolds number $Re = 625, 1250, 2500$ and 5000 . Here the Reynolds number is fixed to a moderate value of $Re = 1000$, this allows a better inspection of the asymptotic decay rate of the truncation or discretization error within a feasible range of resolutions.

In this study we focused on the convergence of the schemes and did not address the computational aspects like, for example, the amount of CPU, memory requirements and parallelization issues. Nevertheless, some additional remarks should be made about the computational aspects of the different methods. In Table 3.1 the computational costs per time step are given for the Chebyshev-Fourier computation (CF), Fourier spectral scheme (FF) and the coherent vortex method (CVS). Both the Chebyshev-Fourier and Fourier spectral solver use the same FFT library and are compiled with the same compiler and optimization options. De-aliasing

of the spectral methods is performed using the zero padding technique or the 2/3 rule, see Ref. [81], thus requiring larger arrays than the number of active modes. An estimate of the CPU costs presented in Table 3.1 is obtained by comparing the array size in the normal direction to the no-slip wall and the well-known scaling proportional to $N \log N$ of the number of operations required for the FFT, see for example Ref. [13]. Note that more FFTs are necessary in the Fourier spectral codes to incorporate volume-penalization, *i.e.* seven instead of five required for the Chebyshev-Fourier computations. From Table 3.1 it can be deduced that the actual costs per time step for the Fourier spectral method are two to three times larger due to the need for an increased array size in the wall-normal direction and extra FFTs related with the volume-penalization. The CPU-time of the CVS simulation is markedly larger. The most expensive routines are the operator adapted wavelet decompositions to solve the Helmholtz and Poisson equations. It is anticipated that a better optimized version of the CVS code will show a significantly improved performance.

For a given resolution Table 3.1 indicates that the costs per time step are minimal for the Chebyshev-Fourier benchmark. However, the time step for the Chebyshev methods is restricted by a local CFL-condition. The strong refinement of the Gauss-Lobatto grid in the near wall region results in a stability condition $\delta t \leq 9/M^2$ [17]. In Ref. [18] and Ref. [53] it is shown, on the other hand, that for higher resolutions it is possible to relax this condition somewhat. The time step for the Fourier spectral method with implicit time integration of the Darcy drag scales only linearly with the number of Fourier modes. In this study the time step was fixed to a relatively small value of $\delta t = 10^{-5}$ for this comparative study. This corresponds with a CFL-number less than 0.1 for the Fourier spectral scheme, which keeps the error induced by the time scheme small with respect to the truncation error. It may be expected that substantial speed up can be gained in this respect for many practical applications while keeping the accuracy of the computation. It is anticipated that the Fourier volume-penalization algorithm will be more efficient than the Chebyshev-Fourier spectral code. We will analyze this issue in further detail in the near future. Recall that it is straightforward to compute a different geometry without additional computational requirements using volume-penalization. This is not the case for Chebyshev spectral methods. For example the costs per time step of the Chebyshev-Chebyshev spectral method (CC) for the square geometry are substantially larger than the Chebyshev-Fourier method for the periodic channel geometry. For $N \lesssim 384$ the costs of Chebyshev-Chebyshev are proportional to $N^2 \log^2 N$, but they become proportional to N^3 for $N \gtrsim 384$.

The dipole-wall collision problem can be seen as a particular problem of fully developed 2D turbulence. Accurate simulation of the collision process can reveal some important aspects *e.g.* the enstrophy production on the domain boundaries [23]. It is, however, important to perform simulations of fully developed bounded turbulence, as well. For these simulations it is essential to have a high resolution in

both the near-wall region and in the interior of the domain, where intensive vortex-vortex interactions require high spatial and temporal resolution. The Fourier spectral and CVS solver can benefit in this respect from the regular grids, while the number of Chebyshev modes needs to be increased substantially due to the non-regular Gauss-Lobatto grid.

In a future study we will conduct a more detailed analysis of the computational aspects involving a wider range of CFD methods like lattice-Boltzmann, finite differences and spectral elements. In addition, the potential of the Fourier and adaptive wavelet scheme will be exploited for pursuing DNS of fully developed high-Reynolds number two and three dimensional flows in complex geometries. With respect to this purpose a promising development for CVS (see Ref. [27]) is to make the time-step adaptive in combination with adaptive multiresolution discretizations in space.

Table 3.1 – *Computational costs per time step of the Chebyshev-Fourier benchmark (CF) computation, Fourier spectral scheme (FF) and coherent vortex simulation (CVS). CF and FF are performed on Itanium 1.3 GHz and CVS on Itanium 1.5 GHz processor. N represents the resolution in the wall normal-direction and M is resolution parallel to the wall. N_{tot} and M_{tot} denote the total array size per direction required for the computation. The FFT costs are estimated with respect to the Chebyshev-Fourier benchmark. Memory estimates are based on array size.*

precision	$< 10^{-4}$		$< 10^{-3}$		
	CF	FF	CF	FF	CVS
N	1024	2730	384	682	1024
M	1364	1364	682	682	1024
N_{tot}	1536	4096	576	1024	1024
M_{tot}	2048	2048	1024	1024	1024
# FFT	5	7	5	7	-
FFT cost	1	4.2	1	2.7	-
CPU meas.	2.6 s	6.0 s	0.4 s	0.7 s	40 s
Memory est.	1	3	1	2	2
Memory meas.	231 MB	750 MB	66 MB	105 MB	630 MB

Chapter 4

Convergence study of an oblique dipole-wall collisionⁱ

In the second benchmark study an important extension is provided considering an oblique dipole-wall collision at a significantly higher Reynolds number. In this way it can be analyzed whether breaking of several symmetries of the square will make Gibbs oscillations dynamically active. Furthermore, another crucially important quantity for bounded 2D turbulence *i.e.* the total angular momentum with respect to the centre of the square, is measured. The (artificial) angular momentum production is also measured for a normal dipole-wall collision in a square geometry that is rotated with respect to the underlying Cartesian mesh. The results of these computations provide important information about the usability of the volume-penalization approach for solving Navier-Stokes flow in complex geometries.

4.1 Geometry error

In Chapter 3 and Keetels *et al.* [48] the truncation error and the penalization error have been quantified by considering the convergence of a very challenging normal dipole-wall collision. To verify if the volume-penalization approach is also capable to solve more complicated geometries it is important to measure a third type of error, *i.e.* the geometry error. This error appears in case a non-trivial geometry is approximated on a regular grid, see, for example the geometries displayed in Fig 2.1a and Fig. 4.1. Recall that in the volume-penalization approach an obstacle (here the rigid wall) is approximated on a regular grid with collocation points coinciding with the boundaries. To quantify the effect of the approximation error of the geometry we study the angular momentum production of a normal dipole-wall

ⁱThe contents of this chapter is an adapted version of Keetels *et al.* [45]

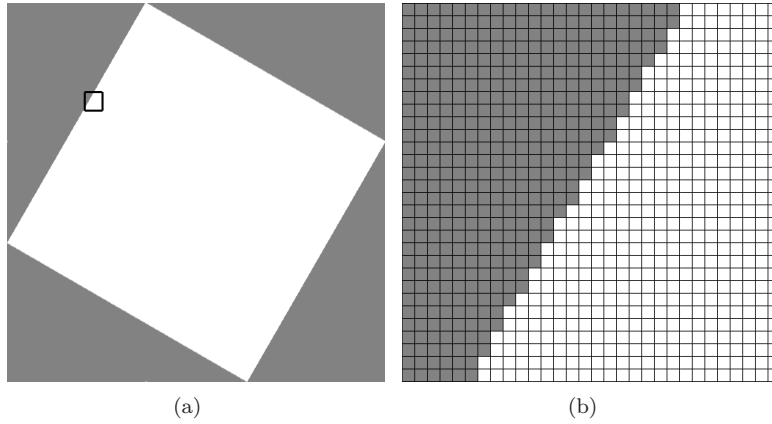


Figure 4.1 – Embedding of a square flow domain under an angle of 30 degrees with respect to a square computational domain with a Cartesian grid. Mask function in complete domain using 512×512 grid points (a), magnification of a small section in the upper left corner (b). Square box in upper left corner of panel (a) represent magnified area presented in panel (b).

collision using the mask function of Fig. 4.1. Note that considering the symmetry of a normal dipole-wall collision angular momentum should, ideally, be absent for all times. Fig. 4.2 shows the angular momentum production versus time for different resolutions. It can be observed that a small amount of angular momentum is produced due to the approximation of the rotated square with respect to the Cartesian grid. Furthermore, the behaviour of the angular momentum depends on the resolution. Table 4.1 displays some statistical quantities of the artificial spin-up of the flow. Note that the data in table 4.1 can be seen as an alternative measure of the numerical convergence of the Fourier spectral method with volume-penalization. It confirms that the approximation of the rotated square geometry on the Cartesian grid yields at best first-order convergence only. The magnitude

Table 4.1 – Statistics of angular momentum production of a normal dipole-wall collision at $Re = 1000$ in rotated square geometry (see Fig. 4.1). Amplitude $A = (L_{max} - L_{min})/2$, maximum of dL/dt , and standard deviation of $\langle dL/dt \rangle$.

N	A	$\max dL/dt$	$\langle dL/dt \rangle$
340	1.5×10^{-3}	2.0×10^{-2}	1.5×10^{-2}
682	9.0×10^{-4}	9.6×10^{-3}	6.0×10^{-3}
1364	5.0×10^{-4}	8.2×10^{-3}	2.7×10^{-3}

of the angular momentum production (here indicated by dL/dt) is, however, negligible compared with the amount of angular momentum production observed for

an oblique dipole-wall collision (two or three magnitudes, see next section). This indicates that the approximation error of the geometry is not a serious drawback for the volume-penalization technique to model different geometries like circular and elliptical domains, for turbulence simulations.

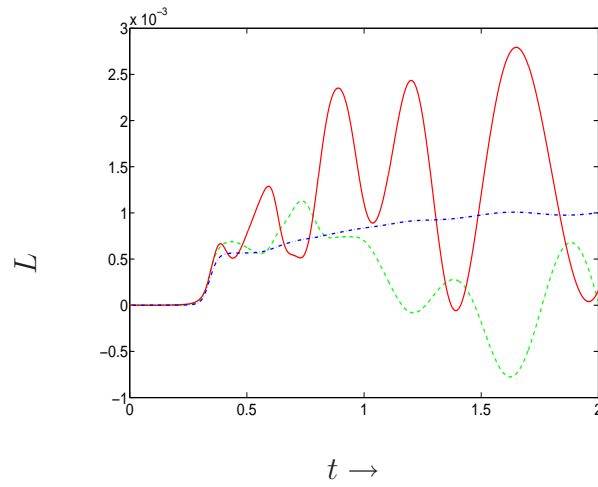


Figure 4.2 – Angular momentum production during a normal collision at $Re = 1000$ using a rotated square domain as shown in Fig. 4.1. Different resolutions are used: the number of active Fourier modes $N = 340$ (solid), $N = 682$ (dashed) and $N = 1364$ (dashed-dot).

4.2 Oblique dipole-wall collisions

To increase the complexity of the flow problem, including the generation of multiple scales, we consider an oblique collision in the square bounded geometry, as shown in Fig. 2.1c, implying breaking of certain symmetries, and at a higher Reynolds number $Re = 2500$. The benchmark computation for this problem is obtained by the Chebyshev solver developed by Clercx [17]. In the square bounded geometry, Chebyshev expansions are applied in both directions. Fig. 4.3a,b show the contour lines of the vorticity of an oblique collision obtained by the Fourier spectral and the Chebyshev benchmark computation, respectively. Note that Fig. 4.3a shows the mollified Fourier projection of the vorticity. A comparison with the benchmark computation shown in Fig. 4.3b demonstrates that the Fourier spectral scheme with post-processing is able to compute the isolines of the small-scale structures sufficiently accurately for this challenging problem. Fig. 4.4 shows a magnification

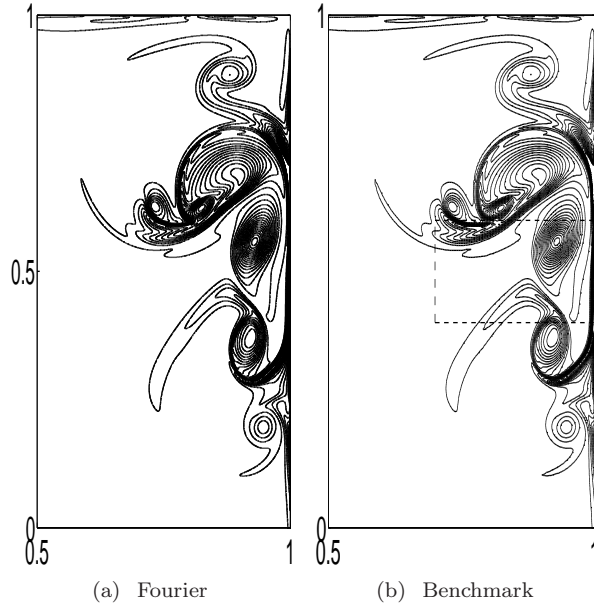


Figure 4.3 – Vorticity isolines of an oblique dipole-wall collision at $t = 0.6$ obtained with a Fourier spectral method with volume-penalization with 2730 active Fourier modes and the time step $\delta t = 2 \times 10^{-5}$. Fourier projection after mollification (a), and the benchmark computation conducted with 640 Chebyshev modes in both directions and $\delta t = 1.25 \times 10^{-5}$ (b). Contour levels are drawn for $-390, -370, \dots, -50, -30, -10, 10, 30, 50, \dots, 370, 390$. The dashed line represents the magnified area of Fig. 4.4.

of a small section of the oblique dipole-wall collision shown in Fig. 4.3. In Fig. 4.4a it can be observed that some Gibbs oscillations are present in the Fourier

projection of the vorticity. The mollification procedure of Tadmor & Tanner [104] results, however, in smooth vorticity isolines, see Fig. 4.4b, that can reasonably well be compared with the Chebyshev benchmark computation in Fig. 4.4c. Recall that a more detailed analysis of the Gibbs oscillations including convergence in the L_2 -sense is performed in [48]. In Fig. 4.3 and Fig. 4.4 it is confirmed that the Gibbs oscillations do not trigger spurious effects during a very intensive oblique dipole-wall collision. Note that reflection symmetry is absent for an oblique collision. Therefore, it is crucial to apply the post-processing procedure of Tadmor and Tanner [104] in both the wall-normal and wall-tangential direction. Important

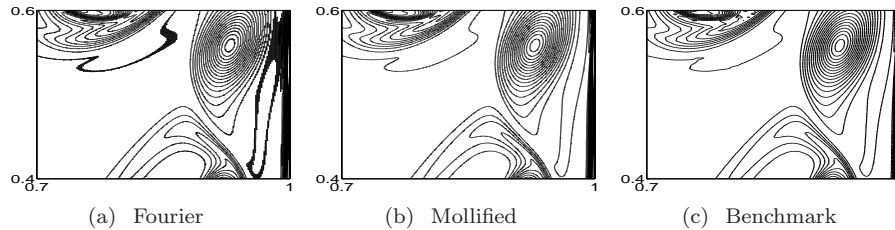


Figure 4.4 – Magnification of the vorticity isolines of the same simulations as presented in Fig. 4.3. The Fourier projection of the vorticity (a), Fourier projection after mollification (b), the benchmark (c).

global measures, *i.e.* the total enstrophy and angular momentum, are presented in Fig. 4.5. The total enstrophy $Z(t)$ is the L_2 -norm of the vorticity in the flow domain Ω_f . The angular momentum of the flow is computed with respect to the centre of the container. It is found that the maximum error in the total enstrophy is smaller than 1%. Recall that the quality of the post-processing procedure of Tadmor & Tanner [104] is only second order in the vicinity of the wall and cannot be applied on the wall itself. Therefore the accuracy in the total enstrophy is slightly limited.

Clercx & Bruneau [18] found that it is difficult to achieve convergence in the total angular momentum, especially after the second collision, due to its critical dependence on the position of strong small-scale vortices near the boundary. Fig. 4.5b shows a very good agreement between the high-resolution benchmark computation with 640 active Chebyshev modes in both directions and the Fourier spectral computation with $N = 2730$ active Fourier modes. Note that the Fourier spectral method corresponds to an equidistant grid, while the Chebyshev method uses a Gauss-Lobatto grid that is strongly refined in the corners of the domain [17]. Therefore, it is not surprising that the required number of active Fourier modes is larger than the number of Chebyshev modes to achieve mode convergence for this particular problem. As we shall see in the following chapters full turbulence simulation demonstrate, however, that small-scale vorticity patches and filaments are advected deep into the interior of the flow domain. To resolve these small-scale

structures in the centre of the domain using a Gauss-Lobatto grid would result in an unfeasible number of active Chebyshev modes.

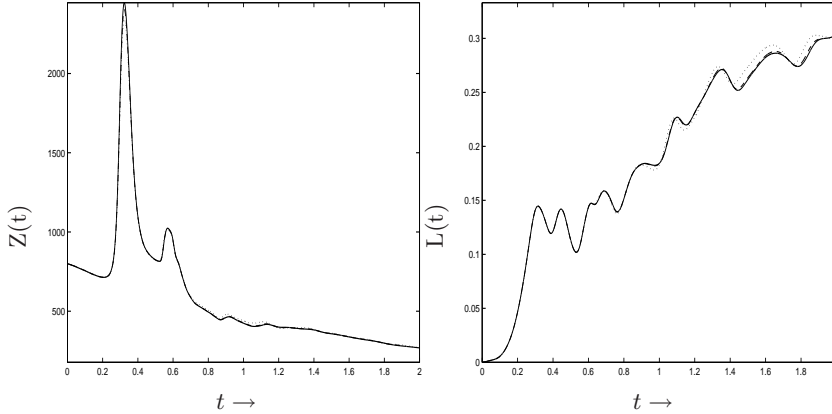


Figure 4.5 – Total enstrophy $Z(t)$ and angular momentum $L(t)$ with respect to the centre of the domain versus time. The Chebyshev benchmark computation is conducted with 640 active Chebyshev modes in both directions and time step $\delta t = 1.25 \times 10^{-5}$ (solid), Fourier spectral computation with volume-penalization obtained with $N = 1364$ (dots) and $N = 2730$ active Fourier modes (dashed). For both runs a time step of $\delta t = 2 \times 10^{-5}$ and penalization parameter $\epsilon = 10^{-8}$ is used. Note that the dashed curve for the Fourier spectral computation with $N = 2730$ active Fourier modes completely coincides with the solid curve of the Chebyshev benchmark computation.

4.3 Conclusion and discussion

The numerical results of the present study demonstrate that it is possible to conduct stable and accurate Fourier spectral computations using volume-penalization for both normal and oblique dipole-wall collisions. The satisfactory convergence results for a normal collision at $Re = 1000$ reported in Keetels *et al.* [48] are confirmed for an oblique collision at a substantially higher Reynolds number $Re = 2500$. Note that reflection symmetry (about x or y -axis) is not present for an oblique collision. As a consequence, Gibbs oscillations may potentially become more dynamically active for an oblique collision compared to a normal collision. It is found, however, that it is possible to remove the Gibbs oscillations from the vorticity isolines appropriately with the same procedure as in the normal-wall collision case considered in Chapter 3. An important and particularly challenging measure of the convergence of an oblique collision is the total angular momentum with respect to the centre of the container. It is observed that the method demonstrates satisfactory convergence compared to a high-resolution Chebyshev spectral scheme. Another interesting observation is that it is apparently not essential to

resolve the details of the penalization boundary layer inside the obstacle. The thickness of the penalization boundary layer is proportional to $\sqrt{\nu\epsilon}$ and is certainly not resolved by the Cartesian mesh used in the present study. This observation can be related to formal expansion of the penalized Navier-Stokes solution (see [14, 48] for details). Only the higher-order terms in the $\sqrt{\epsilon}$ expansion rely on the details of the penalization boundary layer. As a consequence, a $\sqrt{\epsilon}$ accuracy of the penalized Navier-Stokes equations is possible without fully resolving the penalization boundary layer. In the present study it is confirmed that an appropriately small value for the penalization parameter ($\epsilon = 10^{-8}$) results in well-converged intensive dipole-wall interaction.

The simulations with a rotated mask function demonstrate that the error induced by the approximation of the geometry does not result in a significant production of angular momentum. Therefore, the geometry error seems to remain quite small. This result is important for adopting the volume-penalization method for flows in complex geometries. It is in particular shown that the multiscale structures and their dynamical behaviour are correctly predicted by this method. Furthermore, important dynamical quantities such as the total enstrophy and angular momentum are well resolved. In our opinion the combination of Fourier spectral methods and volume-penalization can be useful to pursue DNS of turbulence in complex geometries.

Chapter 5

Quasi-stationary states in a circular geometry

In several numerical and experimental studies [19–21, 66] on freely evolving or decaying 2D turbulence on a square bounded domain it is observed that a flow, initially containing no net angular momentum, spontaneously acquires angular momentum by flow-wall interaction. From earlier work, by Li and Montgomery [60, 61], it could be conjectured that on a circular domain with no-slip boundaries angular momentum production is absent. This observation has recently been confirmed by Schneider and Farge [96] for decaying 2D turbulence with substantially higher initial integral scale Reynolds numbers. In this chapter we revisit the circular case. First we discuss several techniques aimed at describing the end-state of freely evolving flow. Then we proceed with the simulation of decaying turbulence in a circular geometry. The role of the initial condition on the characteristic structure of the end-state is examined.

5.1 Statistical mechanics and the minimum-entropy principle

Several techniques have been developed to characterize the quasi-stationary state of decaying 2D turbulent. For Euler flow a steady state can, according to Eq. (1.5), be described as

$$J(\omega, \psi) = 0. \tag{5.1}$$

This constraint demands a functional form $\omega = g(\psi)$, with g an arbitrary function. Although condition (5.1) corresponds with a steady state in the case of Euler flow, it is observed in several studies [62, 66] that a functional relationship between the vorticity and stream function is also present in the late-time evolution of freely

decaying viscous flow.

Various statistical mechanical approaches have been developed since the early work of Onsager [79] on equilibrium solutions of systems of point vortices. Based on a maximum-entropy principle Joyce and Montgomery [43] showed that this equilibrium solution can be characterized by the sinh-Poisson equation, $\omega = c \sinh(\beta\psi)$. Numerical simulations performed by Montgomery *et al.* [74, 75] on decaying 2D Navier-Stokes turbulence on a double periodic domain demonstrate that the vorticity and the stream function of the quasi-stationary end-state can reasonably well be described by the sinh-Poisson relationship. Note that viscous dissipation is not absent in the latter studies, which apparently has no dramatic consequence for the conjecture of a functional relationship between the vorticity and stream function. A different statistical mechanics approach is developed independently by Miller [71] and Robert and Sommeria [89]. The main difference is that the continuous vorticity field is not described by means of point vortices, but in terms of local probability distributions $\rho(\mathbf{r}, \sigma)$ of different vorticity levels σ at position \mathbf{r} . A locally averaged field of the vorticity or coarse-grained vorticity can then be defined as,

$$\bar{\omega}(\mathbf{r}) = \int \rho(\mathbf{r}, \sigma) \sigma d\sigma. \quad (5.2)$$

Based on the statistical mechanics framework [71, 89] Chavanis and Sommeria [16] provided a classification of stationary *Euler* solutions for various geometries with a *free slip* boundary condition. The coarse-grained vorticity is related with an associated stream function on the fluid domain Ω_f

$$\bar{\omega} = -\Delta \bar{\psi} \quad \text{with} \quad \bar{\psi} = 0 \quad \text{on} \quad \partial\Omega_f. \quad (5.3)$$

The energy associated with the coarse-grained flow field can be expressed as,

$$\bar{E} = \frac{1}{2} \int \bar{\psi} \bar{\omega} d^2 \mathbf{r}. \quad (5.4)$$

Note that the energy is a conserved quantity of Euler flow. Another conserved quantity is the global probability of the vorticity $\gamma(\sigma)$

$$\gamma(\sigma) = \int \rho(\mathbf{r}, \sigma) d^2 \mathbf{r} \quad (5.5)$$

which is essentially the total area of each vorticity level. Furthermore, all the moments of the vorticity are conserved,

$$\bar{\Gamma}_n = \int \gamma(\sigma) \sigma^n d\sigma = \int \bar{\omega}^n d^2 \mathbf{r}. \quad (5.6)$$

The first moment is the circulation of the coarse-grained vorticity and the second moment represents the enstrophy after taking local averages of the squared

vorticity. On a circular domain an additional conserved quantity in the Euler dynamics was recognized by Chavanis and Sommeria [16], which is the total angular momentum now expressed as,

$$\bar{L} = \int \bar{\omega} r^2 d^2 \mathbf{r}. \quad (5.7)$$

The most probable state is obtained by maximizing the entropy,

$$\bar{S}_e = - \int \rho(\mathbf{r}, \sigma) \ln \rho(\mathbf{r}, \sigma) d^2 \mathbf{r} d\sigma. \quad (5.8)$$

A variational problem can then be formulated where the conserved quantities are considered as constraints. Chavanis and Sommeria [16] have studied in particular the limit of strong mixing for which the probabilities $\rho(\mathbf{r}, \sigma)$ are close to uniform. In that case it can be shown that a linear relation between the vorticity and the stream function can be assumed. The solution of the variational problem and the associated maxima of the entropy is governed by a single control parameter $\Lambda(\bar{E}, \bar{\Gamma}_1, \bar{L})$. In case the circulation is zero, the control parameter represents the angular momentum normalized with the kinetic energy. Chavanis and Sommeria [16] observed that an asymmetric dipolar state has the maximum amount of entropy for a wide range of the control parameters. Furthermore, it is shown that the statistical mechanical prediction in the limit of strong mixing is consistent with the principal of minimum enstrophy proposed by Matthaeus and Montgomery [69] and further explored for the case of circular symmetric vortices by Leith [59].

The minimum-entropy principal is motivated by selective decay, see Appendix 5.A, in the presence of weak viscous dissipation. The non-linear transfer of enstrophy from the large scales towards the dissipation ranges enhances the selective decay of the enstrophy. On the other hand, it can be expected in 2D flow that the kinetic energy is confined to the largest scales of motion. It is then anticipated that the enstrophy contained in the large scales reaches a minimum value for a given value of the energy or additional constraints such as the circulation or the angular momentum. Chavanis and Sommeria [16] compared their statistical mechanics approach with the minimum-entropy principle by considering the enstrophy based on the coarse-grained vorticity,

$$\Gamma_2^{cg} = \int \bar{\omega}^2 d^2 \mathbf{r}, \quad (5.9)$$

which is smaller than the total enstrophy $\bar{\Gamma}_2$. It is shown that an equivalent variational problem is obtained by minimizing the coarse-grained enstrophy Γ_2^{cg} and considering the energy \bar{E} , circulation $\bar{\Gamma}_1$, and the angular momentum \bar{L} as constraints. Chavanis and Sommeria [16] demonstrate that exactly the same solutions are obtained by the minimum-entropy variational problem as the statistical mechanical prediction based on a maximum-entropy principle in the limit of strong mixing. Moreover, the value of the entropy and enstrophy of these solutions are

algebraically related *i.e.* a higher maximum of the entropy corresponds with a lower value of the enstrophy minimum and vice versa.

The correspondence between the minimum-enstrophy principle and the statistical mechanical predictions of Chavanis and Sommeria [16] holds for Euler flow with a free slip boundary condition. For viscous flow and the presence of no-slip boundaries the energy, angular momentum and circulation are no longer conserved quantities. Therefore, the statistical mechanical predictions of the quasi-stationary end-state of Chavanis and Sommeria may not be applicable for viscous flow. On the other hand, it can be anticipated that minimum-enstrophy solutions may be selected by Navier-Stokes flow due to the presence of selective viscous decay and the dual cascade phenomenon. Therefore, the minimum-enstrophy states have been computed, see Appendix 5.B. These states may be useful to study the development of large-scale structures in freely decaying Navier-Stokes flow with no-slip boundaries. In this chapter we compare the minimum-enstrophy states with flow structures that emerge in the late time evolution of the decaying turbulence on a circular domain. Furthermore, the stability of the minimum-enstrophy states is studied numerically.

5.2 Setup of the simulations

The simulations in this section are performed in a circular geometry with a radius equal to one. Details of the simulations are collected in table 5.1. The initial condition basically consists of 100 nearly equal-sized Gaussian vortices with a dimensionless radius 0.05. The initial condition is normalized such that the rms velocity $U = 1$. This corresponds with a vortex amplitude $\omega_{max} \simeq 100$. Half of the vortices have positive circulation and the other vortices have negative circulation. The vortices are placed on a regular lattice, well away from the boundaries. The symmetry is slightly broken by a slight displacement of the vortex centres, see for more details [21]. In Fourier transform space certain coefficients are set equal to zero such that the initial angular momentum is zero within machine precision. A smoothing function is applied to ensure that the initial flow is consistent with the no-slip boundary condition. Additionally, some initial fields are generated that contain net angular momentum. This is achieved by adding the fundamental Stokes mode with a certain amplitude (runs 2a and 2b). The initial condition is then normalized such that $U = 1$. In runs 3a and 3b the angular momentum is added via a minimum-enstrophy solution in the branch $j_{11} < \gamma < j_{31}$, see Appendix 5.B for definitions. All runs are repeated twice and also two resolutions $N = 512$ and $N = 1024$ have been applied to check for possible convergence issues. No significant differences have been found.

Table 5.1 – Overview of the disk simulations. The angular momentum of the initial condition L_0 is normalized with the L_{sb} , the amount of angular momentum of a fluid in solid body rotation with the same level of the kinetic energy. The Reynolds number Re is based on the rms velocity and unit radius of the circle. N denotes the spatial resolution, ϵ the penalization parameter and δt the time step. Simulation 1a and 1b do not contain angular momentum. In the initial condition of simulation 2a and 2b angular momentum is added via the fundamental Stokes mode. For the initial condition of run 3a and 3b the presence of net angular momentum is achieved by choosing a minimum-ensrophy state in the branch $j_{11} < \gamma < j_{31}$ with $\gamma = 6.025$, see Appendix 5.B. All the simulations are performed twice with a statistically similar initial condition.

Number	L_0/L_{sb}	Re	N	ϵ	δt
1a	0	5000	512	10^{-8}	5×10^{-4}
1b	0	5000	1024	10^{-8}	2.5×10^{-4}
2a	0.18	5000	512	10^{-8}	5×10^{-4}
2b	0.18	5000	1024	10^{-8}	2.5×10^{-4}
3a	0.22	5000	512	10^{-8}	5×10^{-4}
3b	0.22	5000	1024	10^{-8}	2.5×10^{-4}

5.3 Initialization without angular momentum

Fig. 5.1 shows the vorticity of a run that is initialized without the presence of angular momentum. It can be observed that the number of vortices decreases dramatically during the decay process. The formation, detachment and roll-up of vorticity layers from the boundaries is clearly present in almost all the frames. Fig. 5.2 shows the corresponding stream function. Three typical patterns can be recognized: an asymmetric quadrupole, a symmetric dipole state, and very late in the decay process one observes an asymmetric dipole. Several transitions can be observed between the asymmetric quadrupole and the symmetric dipole patterns. The transition from a dipole state towards a quadrupole can be associated with the roll-up of vorticity layers from the boundaries into two new vortices. Li *et al.* [62] discovered the quadrupole-dipole transition in a numerical simulation at a lower initial Reynolds number of approximately 700. Maassen *et al.* [66] observed this phenomenon in an experiment in a two-layer stratified fluid with a maximal Reynolds number of 1500 – 2000.

The normalized angular momentum, integral length scale and Reynolds number are presented in Fig. 5.3. The angular momentum is normalized with the amount of angular momentum $L_{sb}(t)$ that corresponds with a solid body rotation of the fluid with an equal amount of energy $E(t)$. Normalization with $L_{sb} = L_{sb}(t = 0)$ (dashed-line) in Fig. 5.3 confirms the conjecture that significant production of angular momentum is absent in a circular geometry [60,61]. On the other hand, the angular momentum normalized with $L_{sb}(t)$ increases due to selective decay, see Appendix 5.A for a comprehensive description of the selective decay mechanism. The integral length scale $\mathcal{L} = \sqrt{E/Z}$, is gradually increasing. Note that the integral length scale is based on the total enstrophy and energy of the flow. As a

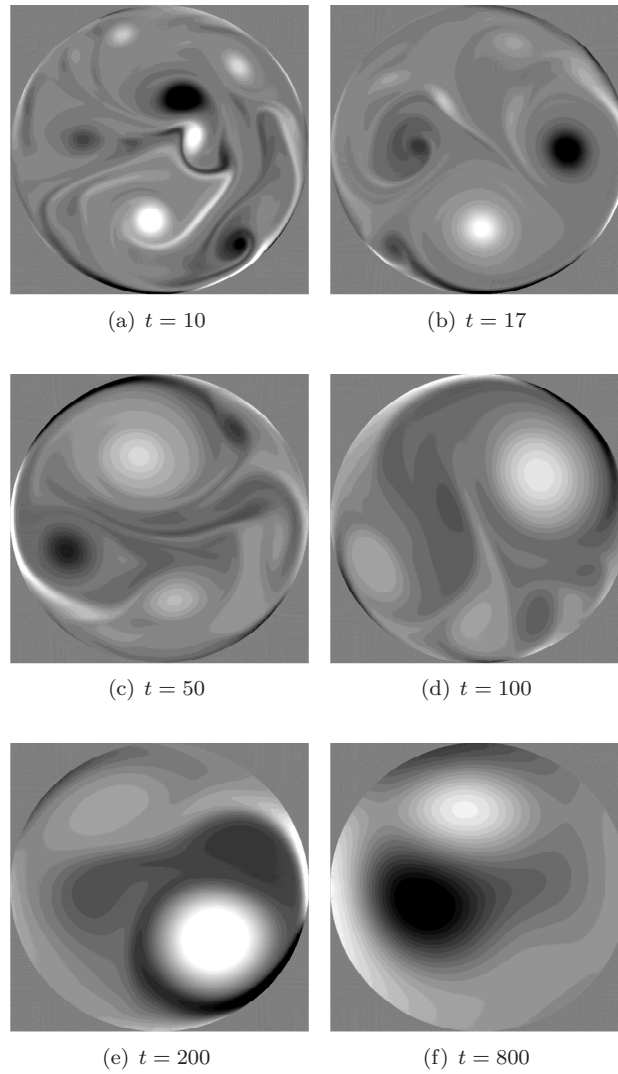


Figure 5.1 – *Vorticity distribution of a $Re = 5000$ simulation initiated with $L = 0$. Twenty gray scales are applied in a vorticity range $[-20, 20]$ (a,b), $[-10, 10]$ (c), $[-5, 5]$ (d), $[-1, 1]$ (e) and $[-0.01, 0.01]$ (f).*

consequence it is affected by both the vorticity in the boundary layers and the large-scale vortices. The fast oscillations in the integral length scale, see Fig. 5.3b, can be associated with the production of vorticity during violent flow-wall interaction events. Note that finally these oscillations are absent as the internal flow

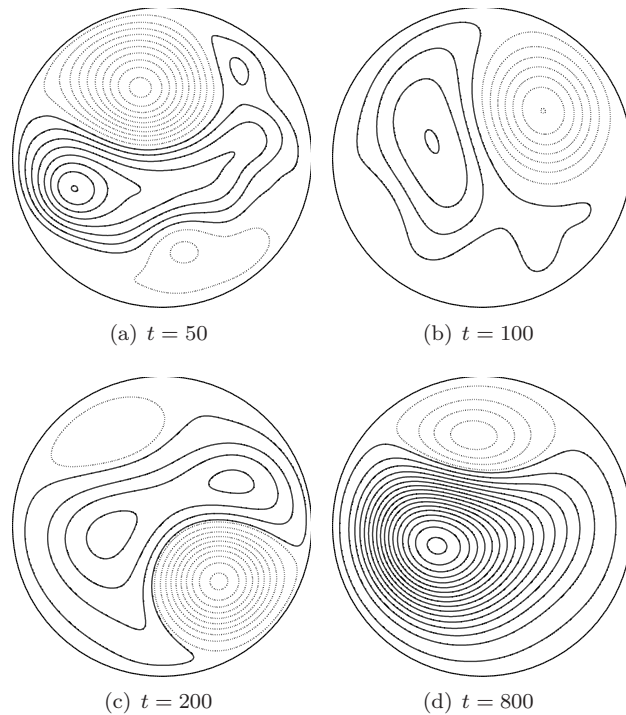


Figure 5.2 – Stream function plot corresponding with the vorticity distribution of Fig. 5.1 for $t = 50, 100, 200$ and 800 . Increments for negative (solid contours) and positive (dashed contours) values are different at $t = 800$ in panel (d).

relaxes towards the end-state and the production of vorticity at the wall ceases. The Reynolds number $Re(t)$ of the flow, during the quadrupole-dipole transition is larger than 500, thus the internal flow can still be considered as advection-dominated.

An explanation of the quadrupole-dipole transition may be found in the framework obtained from the minimum-*enstrophy* principle as developed in Appendix 5.B. A symmetric dipole is the absolute minimum-*enstrophy* solution for $L = 0$. This solution is shown in Fig. 5.15f for the branch $(m, n) = (1, 1)$, where m denotes the angular periodicity of the solution and n controls the structure of the solution in the radial direction, see Appendix 5.B. A symmetric quadrupole belongs to the branch with $(m, n) = (2, 1)$, see Fig. 5.17f. Both the symmetric dipole and the quadrupole are also solutions of the Stokes equation with no-slip boundaries, see Appendix 5.A. In Fig. 5.4 it is demonstrated that the asymmetric quadrupole solution is actually the sum of a symmetric dipole and a symmetric quadrupole. Therefore, the dipole-quadrupole transition can be seen as an excursion between the state with an absolute *enstrophy* minimum and a local *enstrophy*-minimum

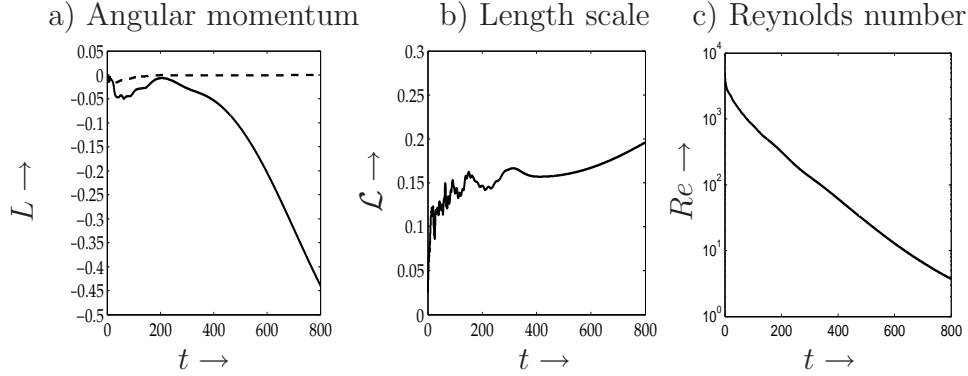


Figure 5.3 – Angular momentum L normalized with $L_{sb}(t = 0)$ (dashed line) and $L_{sb}(t)$ (solid line), integral length scale \mathcal{L} and Reynolds number Re based on the instantaneous energy and radius. Data correspond with the vorticity as shown in Fig. 5.1 with initial Reynolds number $Re = 5000$ and angular momentum $L = 0$.

state. Vorticity injection from the boundaries results in a significant reduction of the integral length scale. Minimizing the enstrophy results then in the formation of a quadrupole, which will gradually evolve towards a symmetric dipolar state. A new cycle is initiated as soon as the vorticity layers detach from the boundary again.

Note that the branch of solutions with $(m, n) = (2, 1)$ for $L = 0$ contains many other solutions, see Fig. 5.17f. Apparently, it is the symmetric quadrupole solution on this branch that plays a crucial role in the decay process. Later in the decay process the relative angular momentum normalized with $L_{sb}(t)$ increases significantly due to selective decay, see Fig. 5.3a (solid line); the corresponding minimal-enstrophy state is an asymmetric dipole, see Fig. 5.15b,c,d.

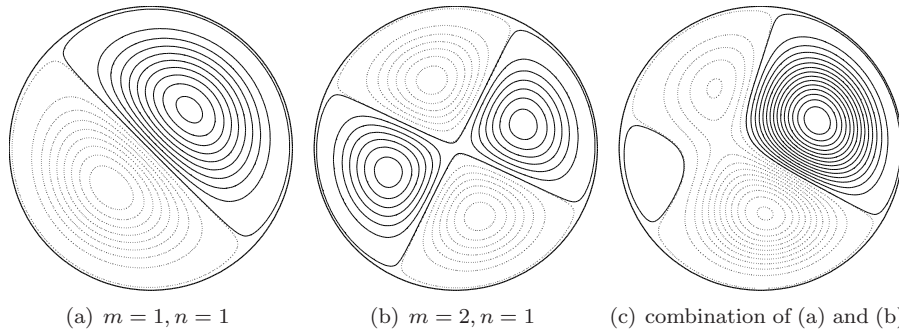


Figure 5.4 – Stream function distribution of a linear combination of the $(m, n) = (1, 1)$ and the $(m, n) = (2, 1)$ minimum-ensrophy solutions. The flow patterns do not contain angular momentum.

5.4 Initialization with angular momentum

Fig. 5.5 presents the evolution of the vorticity distribution in case the initial flow field contains net angular momentum, see table 5.1. From the vorticity plots and the stream function shown in Fig. 5.6 it can be observed that the flow relaxes directly towards the asymmetric dipole state. There is no sign of dipole-quadrupole transitions like in the case without initial angular momentum, as shown in Fig. 5.1. Fig. 5.7 gives the evolution of the angular momentum, integral length scale and Reynolds number. It is seen that the angular momentum normalized with $L_{sb}(t)$ shows some decay early in the flow evolution, but decays very slowly after $t \approx 20$. The angular momentum normalized with $L_{sb}(t)$ increases almost linearly with time due to selective decay. The integral length scale in Fig. 5.7b shows some fast oscillations for $t < 50$, which can be associated with the formation and detachment of the boundary layers. After $t > 50$ the integral length scale increases substantially, which can be associated with the relaxation of the internal flow towards an asymmetric dipole. The Reynolds number in Fig. 5.7c is larger than 500 for $t < 150$, which clearly indicates that the asymmetric dipole is formed in the non-linear regime. The formation of an asymmetric dipole in the presence of significant normalized angular momentum is consistent with the minimum-ensrophy principle. The flow smoothly relaxes to the branch of solutions with $(m, n) = (1, 1)$, as shown in Fig. 5.15, while the normalized angular momentum takes progressively larger values. Note that there is no sign of a transition between this branch of solutions and the neighbouring axisymmetric branch with $j_{11} < \gamma < j_{31}$. The formation of an asymmetric dipole and the absence of a quadrupole state has also been observed experimentally by Maassen *et al.* [66] for a lower Reynolds number $\text{Re} \approx 2000$.

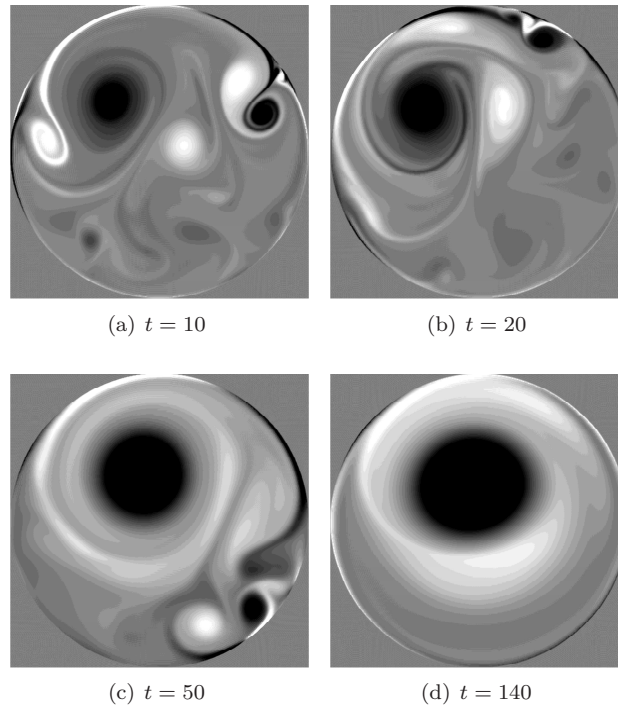


Figure 5.5 – Vorticity distribution of a $Re = 5000$ simulation initiated with normalized angular momentum $L = 0.18$. Initial angular momentum is added via the axisymmetric Stokes mode $(m, n) = (0, 0)$. Twenty gray scales are applied in a vorticity range $[-20, 20]$ (a,b), $[-10, 10]$ (c), $[-5, 5]$ (d), $[-1, 1]$ (e).

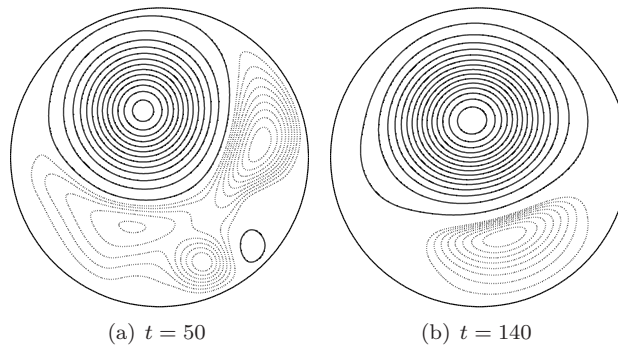


Figure 5.6 – Stream function that corresponds with vorticity fields shown in Fig. 5.5 for $t = 40$, and $t = 140$. Increments for negative (solid contours) and positive (dashed contours) values are different.

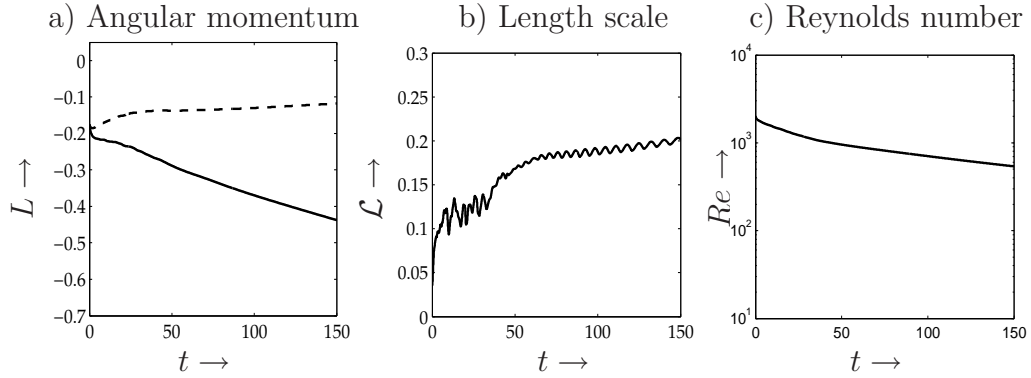


Figure 5.7 – Angular momentum L normalized with $L_{sb}(t=0)$ (dashed line) and $L_{sb}(t)$ (solid line), integral length scale \mathcal{L} and Reynolds number Re based on the instantaneous energy and radius. Data correspond with the vorticity as shown in Fig. 5.5.

5.5 Metastable minimum-ensrophy branch

Fig. 5.8 shows the vorticity distribution of a simulation that is initiated near an axisymmetric minimum-ensrophy solution in the branch $j_{11} < \gamma < j_{31}$ in the diagram shown in Fig. 5.16. On top of this solution a vorticity field is added that consist of 100 Gaussian vortices. During the first decay stage the vortices merge, which yields an almost axisymmetric solution around $t = 1$ in Fig. 5.8a. The stream function at $t = 1$ is given in Fig. 5.9. It can be observed that the global streamline pattern at $t = 1$ is indeed close to the minimum-ensrophy state in the branch $j_{11} < \gamma < j_{31}$. The axisymmetric flow pattern breaks, however, rapidly into a two-fold rotational symmetric state denoted by \mathbf{Z}_2 , see Fig. 5.8b. Afterwards the vorticity from the boundary layers moves into the interior while the \mathbf{Z}_2 symmetry is maintained for many turn-over times, see Fig. 5.8c,d. Finally, the \mathbf{Z}_2 symmetry is broken and the flow evolves towards an asymmetric dipolar structure towards the end of the non-linear regime. In Fig. 5.10 the distribution of the stream function is given. The highly asymmetric dipole structure can clearly be recognized in Fig. 5.10b. The angular momentum, integral length scale and Reynolds number versus time are given in Fig. 5.11. The angular momentum normalized with L_{sb} slowly decays monotonically with time, whereas the angular momentum normalized with $L_{sb}(t)$ increases almost linearly with time due to selective decay. The integral length scale Fig. 5.11b drops rapidly after $t \approx 10$. This can be associated with the injection of vorticity layers from the boundary in Fig. 5.8b,c and subsequent disruption of the large-scale structure of the flow in the interior. After the collapse the integral length scale increases gradually as the flow relaxes toward the asymmetric dipolar end-state.

Transition from the symmetric branch $j_{11} < \gamma < j_{31}$ with a local minimum in the ensrophy, towards the $(m, n) = (1, 1)$ branch of the diagram (shown in Fig. 5.16)

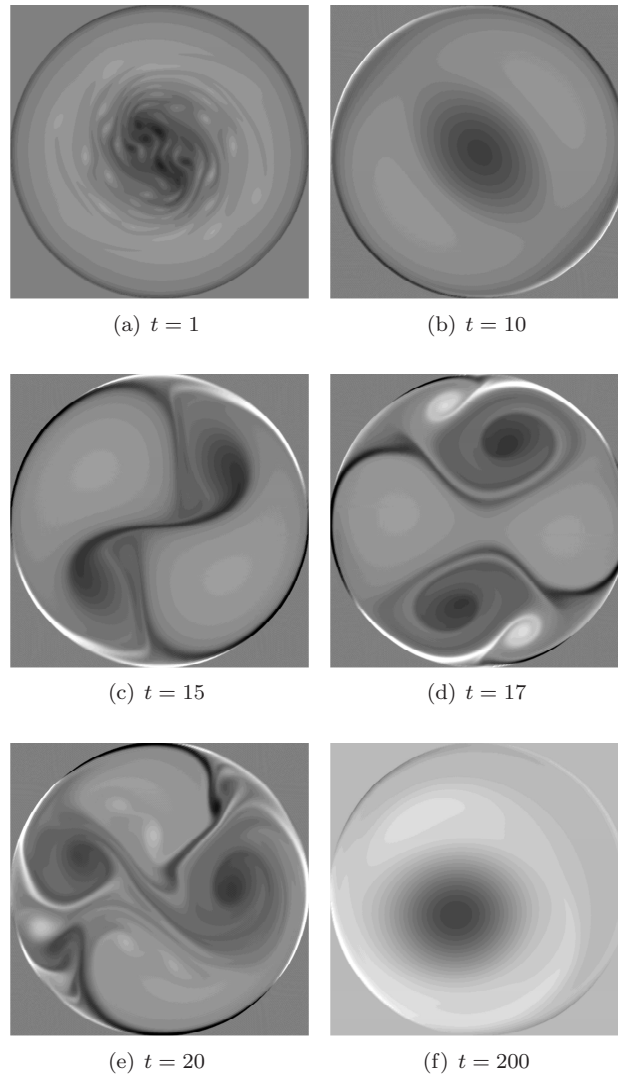


Figure 5.8 – Vorticity distribution of a $Re = 5000$ simulation initialized with 100 Gaussian vortices plus the minimum-entropy state with $\gamma = 6.025$ (for definitions, see appendix 5.B). The normalized angular momentum of the initial flow $L = 0.22$. Twenty gray scales are applied in a vorticity range $[-20, 20]$ (a,b), $[-10, 10]$ (c), $[-5, 5]$ (d), $[-1, 1]$ (e).

with an absolute minimum in the enstrophy, would imply a breaking of the rotational symmetry. Apparently the rotational symmetry breaks via \mathbf{Z}_2 symmetric state first and is then followed by a smooth relaxation towards an end-state so-

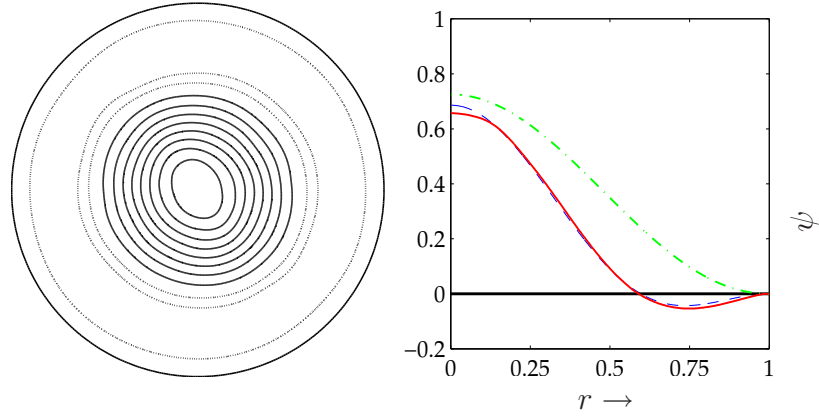


Figure 5.9 – Stream function at $t = 1$ plotted with increments of 0.1. In the panel on the right-hand side a cross-section of the stream function is given along the line $0 < r < 1$ and $\phi = 0$ (solid line), minimum-entropy solution in the branch $j_{11} < \gamma < j_{31}$ of the diagram in Fig. 5.16 containing axisymmetric solutions (dashed line) and a comparison with the fundamental Stokes modes (dashed-dot line). All solutions are normalized such that the energy is equal to one. The normalized angular momentum of the minimum-entropy solution and the flow at $t = 1$ are the same.

lution in the $(1, 1)$ -branch. This transition corresponds with a zigzag excursion in the diagram in Fig. 5.16. The breaking of rotational symmetry into a \mathbf{Z}_2 sym-

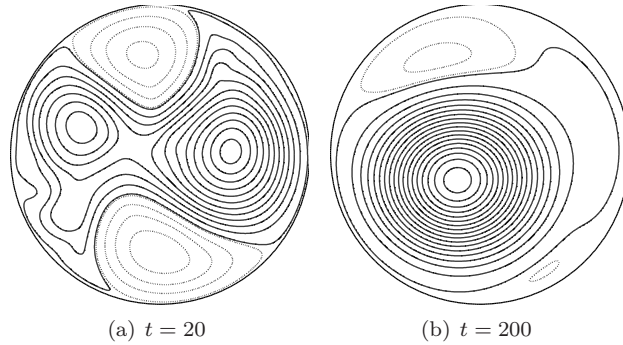


Figure 5.10 – Stream function that corresponds with the vorticity distributions shown in Fig. 5.8 for $t = 20$ and $t = 200$. In panel (a) negative (solid) and positive (dashed) values are drawn with the same increments. In panel (b) increments for positive stream function values are smaller for visualization purposes.

metric state is also found by Sarid *et al.* [91] for 2D Euler flow simulations and

2D electron plasma experiments. Furthermore, Sarid *et al.* observed a breaking of \mathbf{Z}_2 symmetry later in the flow evolution. The end-state in their simulations and experiments strongly depends on the angular momentum and circulation (free-slip boundaries) of the initial flow, as well.

It can be concluded that the minimum-entropy solutions in the branch $j_{11} < \gamma < j_{31}$ are metastable in the sense that they are stable for a few turn-over times, but they become unstable for longer times due to the presence of an absolute minimum solution branch with $(m, n) = (1, 1)$ in the vicinity, see the diagram 5.16. It is verified that axisymmetric solutions in the branch $0 < \gamma < j_{11}$, with an absolute minimum in the entropy are stable.

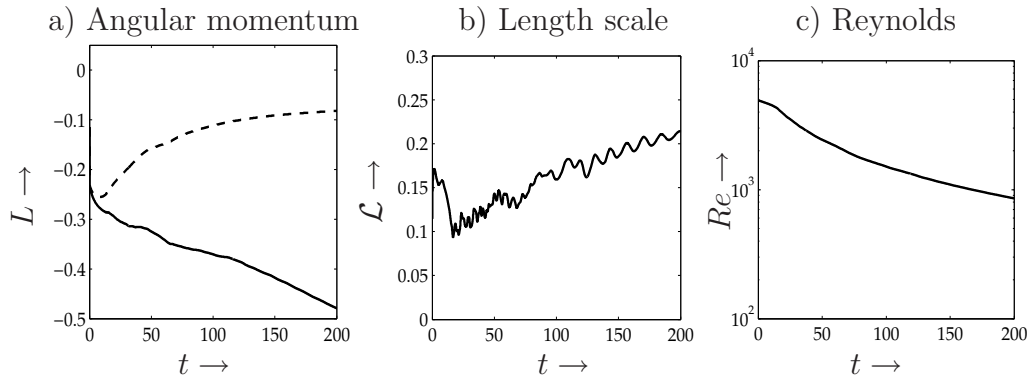


Figure 5.11 – Angular momentum L normalized with $L_{sb}(t=0)$ (dashed line) and $L_{sb}(t)$ (solid line), integral length scale \mathcal{L} and Reynolds number Re based on the instantaneous energy and radius. Data correspond with the vorticity shown in Fig. 5.8.

5.A Appendix: Selective decay

An important mechanism in freely evolving flow is the selective decay due to viscous diffusion [69, 70]. To acquire understanding of this mechanism we will examine a viscous diffusion problem in a circular geometry with no-slip boundaries. In cylindrical coordinates (r, ϕ) the problem is formulated in vorticity form,

$$\frac{\partial \omega}{\partial t} = \nu \Delta \omega \quad \text{for} \quad 0 \leq r \leq a, 0 \leq \phi < 2\pi. \quad (5.10)$$

The no-slip boundary condition (1.3) is considered at $r = a$. In section (1.1.1) it is shown that the no-slip boundary condition can conveniently be described in terms of the stream function,

$$\begin{aligned} \psi &= 0, \\ \psi_r &= 0, \end{aligned} \quad (5.11)$$

where ψ_r denotes the derivative in the radial coordinate direction. In addition a periodic boundary condition:

$$\begin{aligned} \psi(r, \phi + \pi) &= \psi(r, \phi - \pi), \\ \psi_\phi(r, \phi + \pi) &= \psi_\phi(r, \phi - \pi), \end{aligned} \quad (5.12)$$

is considered, where ψ_ϕ is the derivative in the angular coordinate direction. Because the vorticity is related to the stream function ψ by a Poisson equation $\omega = -\Delta\psi$, problem (5.10) should actually be regarded as a fourth-order problem in the stream function. For convenience we consider it as a second-order problem in the first place and solve later the Poisson problem with the boundary conditions (5.11) to obtain the stream function. The Laplacian in cylindrical coordinates (r, ϕ) reads $\Delta = \partial_{rr} + \frac{1}{r}\partial_r + \frac{1}{r^2}\partial_{\phi\phi}$. Application of separation of variables $\omega(r, \phi, t) = R(r)\Phi(\phi)T(t)$ gives

$$\frac{\Delta [R(r)\Phi(\phi)]}{R(r)\Phi(\phi)} = \frac{T'(t)}{\nu T(t)} = -\gamma^2 \quad (5.13)$$

and

$$r^2 \frac{R''(r)}{R(r)} + r \frac{R'(r)}{R(r)} + \gamma^2 r^2 = -\frac{\Phi''(\phi)}{\Phi(\phi)} = m^2, \quad (5.14)$$

where γ and m are the constants of separation. The time dependent part can readily be solved, giving $T(t) = \exp(-\nu\gamma^2 t)$. For the angular dependent part of the solution it is found that $\Phi = \alpha_m \cos(m\phi) + \beta_m \sin(m\phi)$. The periodic boundary condition (5.11) only allows discrete values for the separation constant $m = 0, 1, 2, 3, \dots$. For the r -dependent part it holds that,

$$R''(r) + \frac{1}{r}R'(r) + \left(\gamma^2 - \frac{m^2}{r^2}\right)R(r) = 0, \quad (5.15)$$

which is essentially the Bessel differential equation, see *e.g.* Arfken and Weber [2]. It has solutions in the form of Bessel functions of the first kind $J_m(\gamma r)$. We take $R(r) = \chi_m \gamma^2 J_m(\gamma r)$ (γ^2 in the prefactor is merely a choice for convenience later in the development). Reassembling the total solution for the vorticity gives,

$$\omega = \sum_{m=0}^{\infty} \gamma^2 J_m(\gamma r) (\alpha_m \cos(m\phi) + \beta_m \sin(m\phi)) \exp(-\nu \gamma^2 t), \quad (5.16)$$

where we absorb the coefficient χ_m of the r -dependent part of the solution into α_m and β_m . Note that no boundary condition at $r = a$ has been applied yet, since the no-slip boundary condition (5.11) cannot be defined in terms of the vorticity. Therefore, we have to render the stream function ψ , which is now governed by the following Poisson equation,

$$\Delta \psi = - \sum_{m=0}^{\infty} \gamma^2 J_m(\gamma r) (\alpha_m \cos(m\phi) + \beta_m \sin(m\phi)) \exp(-\nu \gamma^2 t) \quad (5.17)$$

for $0 \leq r \leq a$ and $0 \leq \phi < 2\pi$, with accompanying boundary conditions $\psi = 0$ and $\psi_r = 0$ at $r = a$. Inspiration for a particular solution $\tilde{\psi}$ can be found in the Bessel differential equation (5.15) itself, yielding

$$\tilde{\psi} = \sum_{m=0}^{\infty} J_m(\gamma r) (\alpha_m \cos(m\phi) + \beta_m \sin(m\phi)) \exp(-\nu \gamma^2 t). \quad (5.18)$$

Now the Poisson problem can be transformed in a Laplace problem for the homogeneous part of the solution

$$\Delta \psi = 0, \quad 0 \leq r \leq a, \quad (5.19)$$

with boundary conditions at $r = a$

$$\psi = - \sum_{m=0}^{\infty} J_m(\gamma a) (\alpha_m \cos(m\phi) + \beta_m \sin(m\phi)) \exp(-\nu \gamma^2 t) \quad (5.20)$$

and

$$\psi_r = \sum_{m=0}^{\infty} (\gamma J_{m+1}(\gamma a) - \frac{m}{a} J_m(\gamma a)) (\alpha_m \cos(m\phi) + \beta_m \sin(m\phi)) \exp(-\nu \gamma^2 t) \quad (5.21)$$

for $0 \leq \phi < 2\pi$. The bounded solution of the Laplace problem (5.19) on a circle is given by

$$\psi = a_0 + \sum_{m=1}^{\infty} a_m r^m \cos(m\phi) + b_m r^m \sin(m\phi), \quad (5.22)$$

which can readily be obtained by separation of variables and taking into account the angular periodicity (5.12). Using the orthogonality of the Fourier system $\{1, \cos(m\phi), \sin(m\phi)\}$ we obtain from the boundary condition (5.20) for ψ at $r = a$,

$$\begin{aligned} a_m &= -\alpha_m a^{-m} J_m(\gamma a) \exp(-\nu \gamma^2 t), \\ b_m &= -\beta_m a^{-m} J_m(\gamma a) \exp(-\nu \gamma^2 t) \end{aligned} \quad (5.23)$$

and from the boundary condition (5.21) for ψ_r at $r = a$ we find

$$\begin{aligned} a_m &= \alpha_m \left[\frac{\gamma}{m a^{m-1}} J_{m+1}(\gamma a) - a^{-m} J_m(\gamma a) \right] \exp(-\nu \gamma^2 t), \\ b_m &= \beta_m \left[\frac{\gamma}{m a^{m-1}} J_{m+1}(\gamma a) - a^{-m} J_m(\gamma a) \right] \exp(-\nu \gamma^2 t). \end{aligned} \quad (5.24)$$

For consistency of (5.23) with (5.24) it is required that $J_{m+1}(\gamma a) \equiv 0$, hence the constant of separation γ has discrete values denoted by

$$\gamma_{mn} = \frac{j_{(m+1)n}}{a}, \quad (5.25)$$

where $j_{(m+1)n}$ represents zero number $n = 1, 2, 3, \dots$ of the $(m+1)$ -order Bessel function of the first kind. The total solution of the Stokes problem (5.10) becomes

$$\psi = \sum_{m=0}^{\infty} \sum_{n=1}^{\infty} \psi_{mn} \exp(-\nu \gamma_{mn}^2 t), \quad (5.26)$$

with

$$\begin{aligned} \psi_{mn} &= \alpha_{mn} \left[J_m(\gamma_{mn} r) - \frac{r^m}{a^m} J_m(\gamma_{mn} a) \right] \cos(m\phi) + \\ &\quad \beta_{mn} \left[J_m(\gamma_{mn} r) - \frac{r^m}{a^m} J_m(\gamma_{mn} a) \right] \sin(m\phi) \end{aligned} \quad (5.27)$$

and for the vorticity

$$\omega = \sum_{m=0}^{\infty} \sum_{n=1}^{\infty} \gamma_{mn}^2 J_m(\gamma_{mn} r) [\alpha_{mn} \cos(m\phi) + \beta_{mn} \sin(m\phi)] \exp(-\nu \gamma_{mn}^2 t). \quad (5.28)$$

The coefficients α_{mn} and β_{mn} can be determined by an appropriate initial condition. Orthogonality conditions of the Fourier-Bessel series [2] are useful for this purpose.

It can be observed in (5.26) and (5.28) that the dissipation rate of mode ψ_{mn} or ω_{mn} is determined by the separation constant or Stokes eigenvalue γ_{mn} of the problem (5.25). The hierarchy in the dimensionless eigenvalues $j_{1n} < j_{2n} < j_{3n} < \dots$, implies that the axisymmetric modes corresponding with j_{1n} decay slower compared with the modes that have an angular periodicity $m = 1, 2, 3, \dots$. Note that only the axisymmetric modes contain angular momentum. The second hierarchy

$j_{m1} < j_{m2} < j_{m3} < \dots$ implies that the modes with the same angular periodicity, but more variation in the radial direction dissipate faster. The Stokes dimensional eigenvalue γ corresponds with a characteristic length scale of each mode, note that the dimension of $[\gamma] = m^{-1}$. Therefore, it can also be expected on dimensional grounds and (5.10) that a higher value of the eigenvalue will result in a faster viscous decay rate of the mode.

5.B Appendix: Minimum-entrophy principle on a circular domain

In this section a minimum-entrophy principle [58, 69, 70] is applied for flows in a circular geometry with a no-slip wall. Based on this principle a variational problem will be formulated and a derivation of the set of solutions will be given. Furthermore, the solutions will be organized in a diagram that may serve as a framework to understand the complicated structure of the end-state of decaying flow in a circular geometry. For an introduction to the variational technique applied here one can consult for instance Arfken and Weber [2].

We are seeking stationary values of the integral

$$Z[\psi] = \frac{1}{2} \int_{\mathcal{C}} \omega^2 dA = \int_{\mathcal{C}} \Upsilon(\psi_{xx}, \psi_{yy}) dA \quad (5.29)$$

where $\Upsilon(\psi_{xx}, \psi_{yy}) = \frac{1}{2}\omega^2$. In conjunction we consider constraints in the total kinetic energy

$$E[\psi] = \frac{1}{2} \int_{\mathcal{C}} \omega\psi dA = \int_{\mathcal{C}} \Xi(\psi, \psi_{xx}, \psi_{yy}) dA \equiv 1 \quad (5.30)$$

and in the total angular momentum

$$L[\psi] = 2 \int_{\mathcal{C}} \psi dA = \int_{\mathcal{C}} f(\psi) dA \equiv \text{constant}, \quad (5.31)$$

where $\Xi(\psi_{xx}, \psi_{yy}, \psi) = \frac{1}{2}\omega\psi$, $f(\psi) = 2\psi$, ω denotes the vorticity and ψ the stream function, with $\omega = -\Delta\psi$. By using the Lagrange multipliers λ_1 and λ_2 it is possible to absorb the constraints (5.30) and (5.31) in the variation of $Z[\psi]$, thus

$$\delta \left(\int_{\mathcal{C}} g(\psi, \psi_{xx}, \psi_{yy}) dA \right) = 0 \quad (5.32)$$

where $g(\psi, \psi_{xx}, \psi_{yy}) = \Upsilon(\psi_{xx}, \psi_{yy}) + \lambda_1 f(\psi) + \lambda_2 \Xi(\psi, \psi_{xx}, \psi_{yy})$. The corresponding Euler-Lagrange equation for this problem reads,

$$\frac{\partial g}{\partial \psi} + \frac{\partial^2}{\partial x^2} \frac{\partial g}{\partial \psi_{xx}} + \frac{\partial^2}{\partial y^2} \frac{\partial g}{\partial \psi_{yy}} = 0 \quad \text{on} \quad \mathcal{C}, \quad (5.33)$$

by mere substitution this yields,

$$\Delta^2 \psi - \lambda_2 \Delta \psi = -2\lambda_1 \quad \text{on} \quad \mathcal{C}. \quad (5.34)$$

For convenience we define $\gamma^2 = -\lambda_2$ and $\Gamma = 2\lambda_1$, hence

$$\Delta^2 \psi + \gamma^2 \Delta \psi = -\Gamma \quad \text{on} \quad \mathcal{C}, \quad (5.35)$$

where we consider no-slip boundaries on $\partial\mathcal{C}$ to close the problem. In terms of the vorticity (5.35) reads,

$$\Delta\omega + \gamma^2\omega = \Gamma \quad \text{on} \quad \mathcal{C} \quad (5.36)$$

A particular solution $\tilde{\omega}$ in the cylindrical coordinates (r, ϕ) is readily obtained,

$$\tilde{\omega} = \frac{\Gamma}{\gamma^2} \quad (5.37)$$

For the homogeneous $\bar{\omega}$ part holds a Helmholtz equation of the form,

$$\Delta\bar{\omega} + \gamma^2\bar{\omega} = 0 \quad \text{on} \quad \mathcal{C}, \quad (5.38)$$

which can easily be solved with separation of variables and assuming a periodic condition in the angular direction, see appendix 5.A. The total solution $\omega = \tilde{\omega} + \bar{\omega}$ is now given by,

$$\omega = \sum_{m=0}^{\infty} \gamma^2 J_m(\gamma r) [\alpha_m \cos(m\phi) + \beta_m \sin(m\phi)] + \frac{\Gamma}{\gamma^2}, \quad (5.39)$$

where $m = 0, 1, 2, 3, \dots$. Since the boundary condition is defined in terms of ψ and ψ_r we have to compute the stream function, which is now governed by a Poisson equation of the form

$$\Delta\psi = - \sum_{m=0}^{\infty} \gamma^2 J_m(\gamma r) [\alpha_m \cos(m\phi) + \beta_m \sin(m\phi)] - \frac{\Gamma}{\gamma^2}, \quad (5.40)$$

with accompanying boundary conditions $\psi = \psi_r = 0$ at $r = a$. A particular solution $\tilde{\psi}$ is given by

$$\tilde{\psi} = \sum_{m=0}^{\infty} J_m(\gamma r) [\alpha_m \cos(m\phi) + \beta_m \sin(m\phi)] - \frac{\Gamma}{4\gamma^2} r^2 + c_1, \quad (5.41)$$

where c_1 is a constant. The homogeneous part is then described by a Laplace equation,

$$\Delta\bar{\psi} = 0 \quad \text{on} \quad \mathcal{C}. \quad (5.42)$$

By considering the particular solution (5.41) one can formulate a boundary condition for the homogeneous part $\bar{\psi}$ at $r = a$,

$$\bar{\psi} = - \sum_{m=0}^{\infty} J_m(\gamma a) [\alpha_m \cos(m\phi) + \beta_m \sin(m\phi)] + \frac{\Gamma a^2}{4\gamma^2} - c_1 \quad (5.43)$$

and a boundary condition in $\bar{\psi}_r$ at $r = a$,

$$\bar{\psi}_r = \sum_{m=0}^{\infty} \left[\gamma J_{m+1}(\gamma a) - \frac{m}{a} J_m(\gamma a) \right] [\alpha_m \cos(m\phi) + \beta_m \sin(m\phi)] + \frac{\Gamma a}{2\gamma^2}. \quad (5.44)$$

5.B Appendix: Minimum-ensrophy principle on a circular domain 97

This problem can be solved by using the general (bounded) solution of the Laplace equation on a circle

$$\bar{\psi} = a_0 + \sum_{m=1}^{\infty} a_m r^m \cos(m\phi) + b_m r^m \sin(m\phi). \quad (5.45)$$

The coefficients a_m and b_m can be determined by using the orthogonality of the Fourier system $\{1, \cos(m\phi), \sin(m\phi)\}$ and the boundary conditions (5.43) and (5.44) at $r = a$.

For $m = 0$ the boundary condition for $\bar{\psi}$ gives $a_0 = -J_0(\gamma a)\alpha_0 + \frac{\Gamma a^2}{4\gamma^2} - c_1$, while the boundary condition for $\bar{\psi}_r$ requires that $\alpha_0 = -\frac{\Gamma a}{2\gamma^3 J_1(\gamma a)}$. The stream function for $m = 0$ is then given by,

$$\psi = -\frac{\Gamma a}{2\gamma^3 J_1(\gamma a)} [J_0(\gamma r) - J_0(\gamma a)] + \frac{\Gamma}{4\gamma^2} (a^2 - r^2), \quad (5.46)$$

and the vorticity by

$$\omega = -\frac{\Gamma a}{2\gamma J_1(\gamma a)} J_0(\gamma r) + \frac{\Gamma}{\gamma^2}. \quad (5.47)$$

Recall that Γ and γ are the Lagrange multipliers in the variational problem, related to the constraints in the total kinetic energy and enstrophy.

For $m > 0$ it follows that $a_m = -\alpha_m J_m(\gamma a) a^{-m}$, $b_m = -\beta_m J_m(\gamma a) a^{-m}$ and γ can only be chosen from the discrete set $\gamma = \gamma_{mn}$, which is defined by $J_{m+1}(\gamma_{mn} a) = 0$. The solution for $m > 0$ is

$$\begin{aligned} \psi = & -\frac{\Gamma a}{2\gamma_{mn}^3 J_1(\gamma_{mn} a)} [J_0(\gamma_{mn} r) - J_0(\gamma_{mn} a)] + \frac{\Gamma}{4\gamma_{mn}^2} (a^2 - r^2) \\ & + \alpha_{mn} [J_m(\gamma_{mn} r) - J_m(\gamma_{mn} a) \frac{r^m}{a^m}] \cos(m\phi) + \\ & \beta_{mn} [J_m(\gamma_{mn} r) - J_m(\gamma_{mn} a) \frac{r^m}{a^m}] \sin(m\phi), \end{aligned} \quad (5.48)$$

with vorticity,

$$\begin{aligned} \omega = & -\frac{\Gamma a}{2\gamma_{mn} J_1(\gamma_{mn} a)} J_0(\gamma_{mn} r) + \frac{\Gamma}{\gamma_{mn}^2} \\ & + \alpha_{mn} \gamma_{mn}^2 J_m(\gamma_{mn} r) \cos(m\phi) + \beta_{mn} \gamma_{mn}^2 J_m(\gamma_{mn} r) \sin(m\phi). \end{aligned} \quad (5.49)$$

Note that the parameter γ for $m > 0$ is determined by the boundary conditions, whereas for the axisymmetric case $m = 0$ the parameter γ acts as a Lagrange multiplier. For $m > 0$ two new parameters α_{mn} and β_{mn} appear and $\gamma = \gamma_{mn}$. Note that these new parameters, which are not present in the original formulation of the problem, are related to the phase of the solution in the angular direction. In the computation of the total kinetic energy these parameters essentially act as a single parameter of the form $\alpha_{mn}^2 + \beta_{mn}^2$. Therefore, there are in fact only

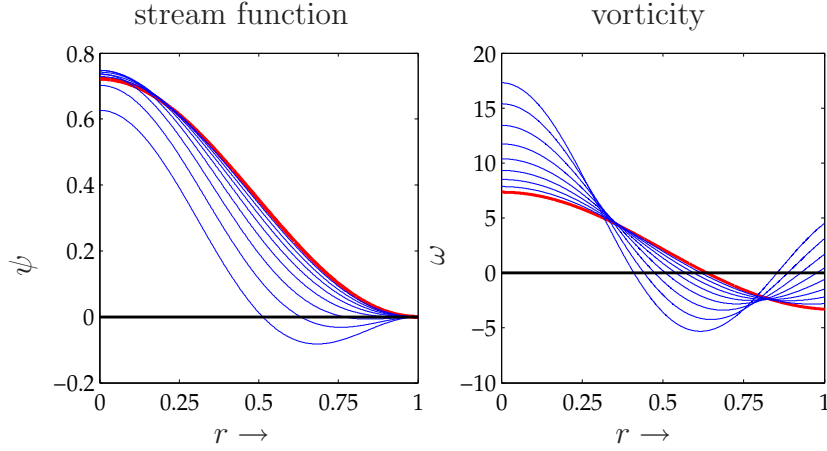


Figure 5.12 – Cross-sectional distributions of the stream function and vorticity for the axisymmetric case. The parameter γ is chosen between $j_{11} < \gamma < j_{12}$ and Γ is chosen such the total kinetic energy is normalized to unity. The thick line represents the case $\gamma = j_{11}/20$.

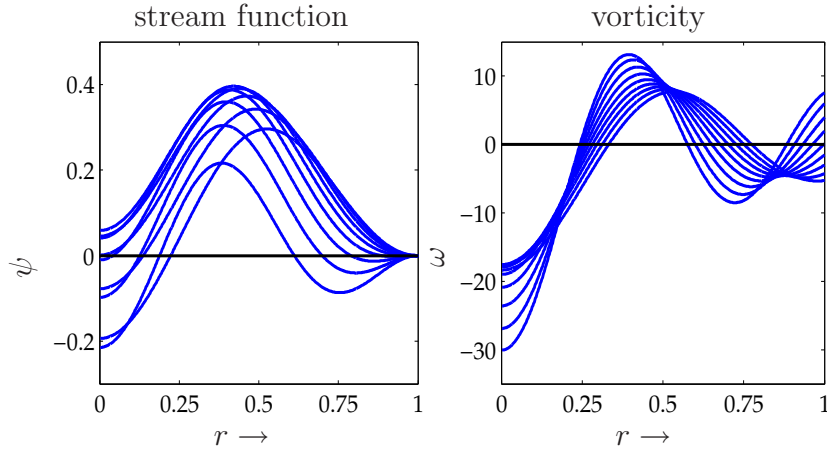


Figure 5.13 – Cross-sectional distributions of the stream function and vorticity for the axisymmetric case. The parameter γ is chosen between $j_{12} < \gamma < j_{13}$ and Γ is chosen such that the total kinetic energy is normalized to unity.

two undetermined parameters Γ and $\alpha_{mn}^2 + \beta_{mn}^2$ concerning the constraints in the total kinetic energy and angular momentum. It is also important to realize that the angular dependent part of the solution does not carry net angular momentum.

We start with a description of the axisymmetric solutions. Without loss of gener-

5.B Appendix: Minimum-entropy principle on a circular domain 99

ality the unit circle $a = 1$ will be considered. The Lagrange multiplier Γ is chosen such that the total kinetic energy is $E = 1$. Fig. 5.12 shows the stream function and the vorticity for $\gamma = j_{11}/20$ and for $j_{11} < \gamma < j_{12}$, where j_{1n} denotes the n -th zero of the first-order Bessel function, *i.e.* $J_1(j_{1n}) = 0$. It is observed that for $\gamma = j_{11}/20$ a domain filling structure appears that has a maximum in the centre and a minimum at the domain boundary. The other solutions for $0 < \gamma < j_{11}$ (not shown) have a similar appearance.

The first mode in the branch $j_{11} < \gamma < j_{12}$ shows resemblance with the previous mode. However, increasing γ until j_{12} we observe that the minimum moves from the domain boundary into the interior of the domain. Fig. 5.13 shows the branch

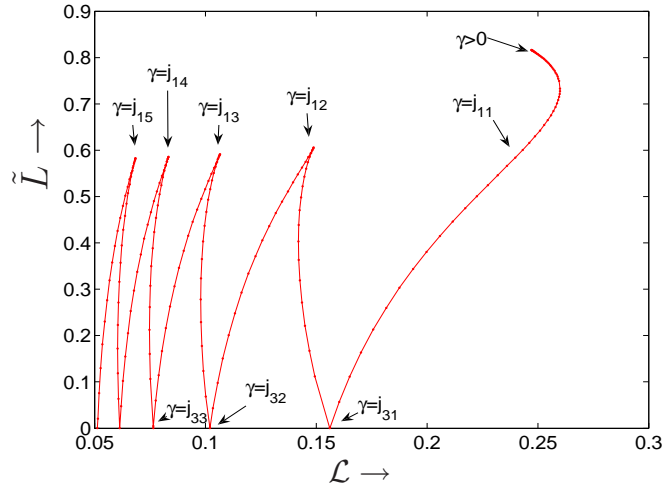


Figure 5.14 – Net angular momentum $\tilde{L} = |L|/L_{sb}$ normalized with L_{sb} versus the integral length scale \mathcal{L} for the axisymmetric solutions. Note that $0 < j_{11} < j_{31} < j_{12} < j_{32} < j_{13} < j_{33} < j_{14} < j_{34} < j_{15} < j_{35}$. The curves corresponding with $\gamma < j_{35}$ are not shown.

of solutions with $j_{12} < \gamma < j_{13}$. The stream function takes an entirely different shape compared to the branch $j_{11} < \gamma < j_{12}$ in Fig. 5.12. The bifurcation in the solutions at $\gamma = j_{1n}$ can be associated with the presence of γ in the nominator of the first term in the expression of the stream function (5.46) and vorticity (5.47).

Fig. 5.14 presents the axisymmetric solutions in a diagram with the normal-

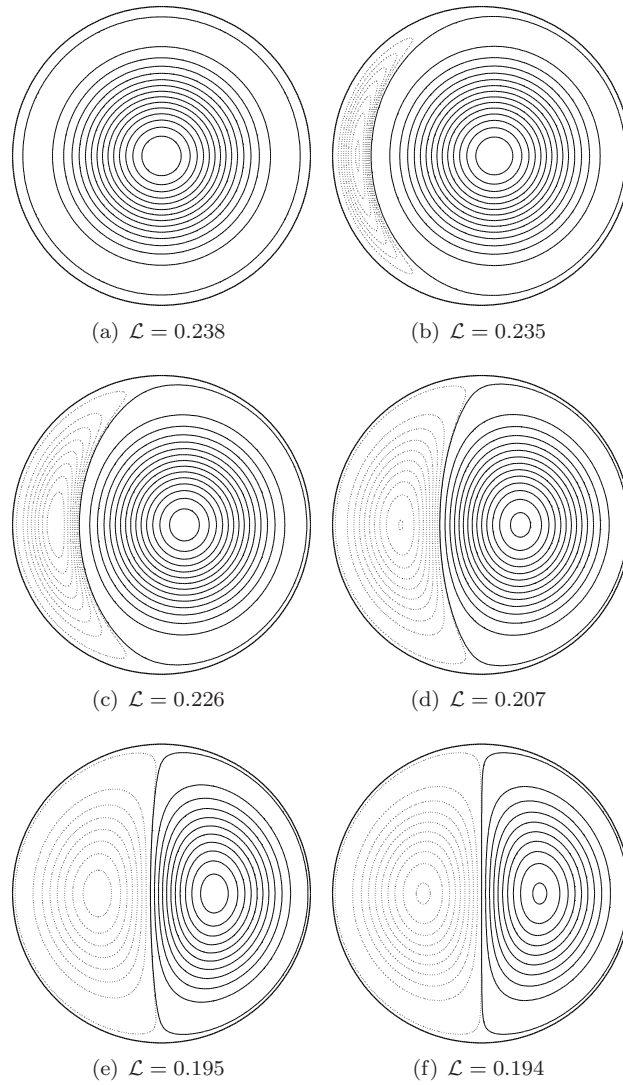


Figure 5.15 – Contour lines of ψ for the solution branch with $(m, n) = (1, 1)$ and $\gamma = j_{21}$. Panel (a) corresponds with the axisymmetric case with $\alpha_{11} = \beta_{11} = 0$ and $\Gamma \neq 0$. Panel (f) shows the fully periodic case with $\alpha_{11} \neq 0$, $\beta_{11} = 0$ and $\Gamma = 0$. The other solutions in the panels (b-e) are a linear combination of (a) and (f) with $\Gamma \neq 0$ and $\alpha_{11} \neq 0$ and $\beta_{11} = 0$. The angular momentum $L = 0.5763$ (a), 0.5580 (b), 0.5099 (c), 0.3473 (d), 0.1068 (e), respectively, and $L = 0$ (f). In panels (a-e) the increment size for the negative values of ψ differs from the increment size for the positive values of ψ . In panel (f) the increments are the same for both negative and positive values of ψ .

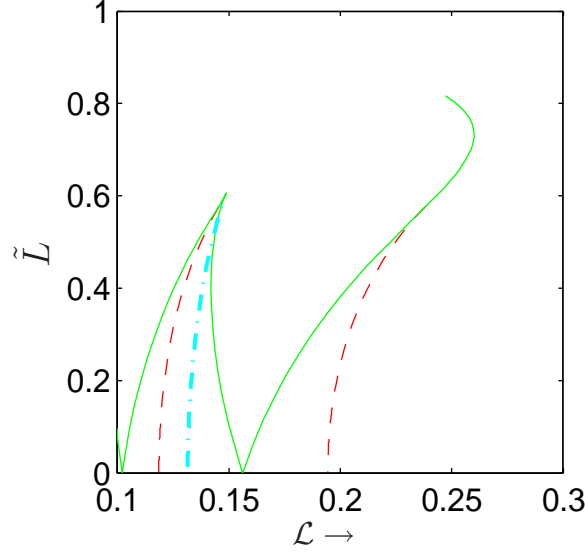


Figure 5.16 – Position of periodic solutions in the diagram with the normalized angular momentum versus the integral length scale. Axisymmetric solutions (solid), solutions with $(m, n) = (1, 2)$ (dashed, left) and $(1, 1)$ (dashed, right) and $(3, 1)$ (dashed-dot). The solutions $(3, 1)$ are situated at $\mathcal{L} \approx 0.156$ and $L = 0$. Periodic solutions branch from axisymmetric $m = 0$ curves at $\gamma = j_{(m+1)n}$.

ized angular momentum L versus the integral length scale \mathcal{L} . Note the ordering in the parameter γ along the different branches. The new branch of solutions starts at $\gamma = j_{1n}$. The axisymmetric solutions for $\gamma = j_{3n}$, do not contain angular momentum. Fig. 5.17a gives an example of the axisymmetric solution for $\gamma = j_{31}$. A sequence of solutions is generated with periodicity $(m, n) = (1, 1)$ with $\gamma = j_{21}$. The stream function distributions belonging to this branch are given in Fig. 5.15. Fig. 5.15a shows an axisymmetric solution that contains a significant amount of angular momentum. The stream function in Fig. 5.15f corresponds with the other limiting case on the branch with $\gamma = j_{21}$, which is essentially a Stokes mode, see Section (5.A). The other solutions are a linear combination of the symmetric dipole and the axisymmetric component, where the relative contribution is controlled by the parameters Γ and $\alpha_{11}^2 + \beta_{11}^2$, see (5.48) and (5.49).

Fig. 5.16 shows the position (dashed line on right-hand side) of this branch of solutions in the diagram. For comparison the purely axisymmetric solutions presented in Fig. 5.14 are also given (solid lines). Solutions with higher periodicity, e.g. $(m, n) = (1, 2)$, $(2, 1)$ and $(3, 1)$ emerge at much smaller integral length scales, corresponding with $\gamma = j_{22}$, $\gamma = j_{31}$ and $\gamma = j_{41}$, respectively. A very interesting branch of solutions with $(m, n) = (2, 1)$ can be found at $\gamma = j_{31}$. All the solu-

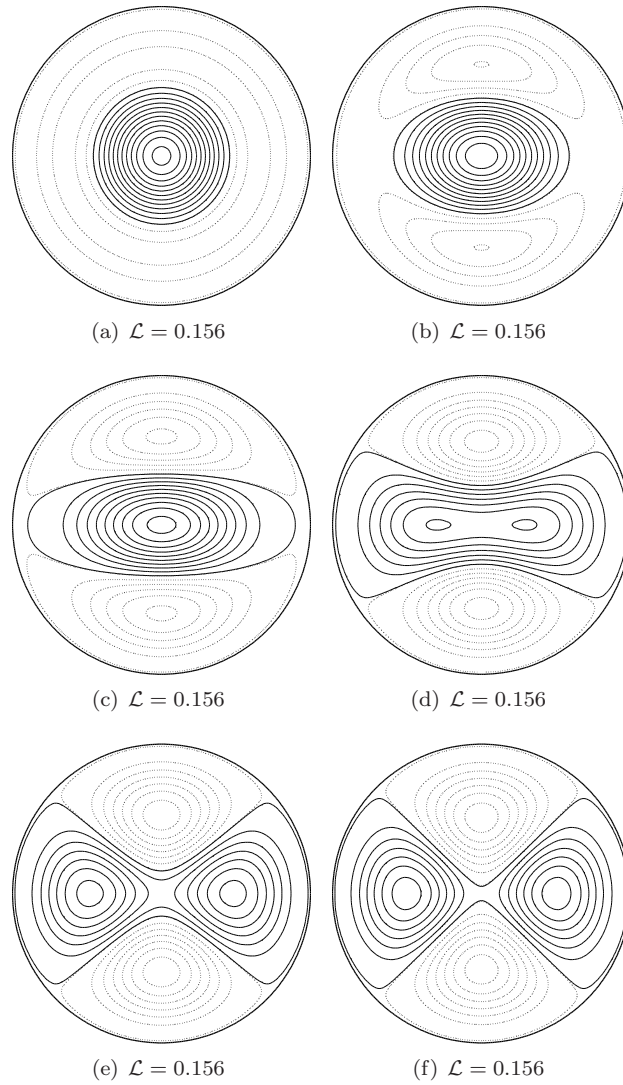


Figure 5.17 – Branch of solutions for $(m, n) = (2, 1)$ and $\gamma = j_{3n}$. All solutions have the same integral length scale $\mathcal{L} = 0.156$ and do not contain angular momentum.

tions on this branch correspond with a specific value of the integral length scale $\mathcal{L} = 0.156$ whereas the angular momentum L is zero. Fig. 5.17 gives the stream function distributions of the $(m, n) = (2, 1)$ branch. Note that even the axisymmetric solution in Fig. 5.17a does not contain angular momentum. The angular dependent part with periodicity $m = 2$ (a quadrupole) is essentially the Stokes

5.B Appendix: Minimum-entropy principle on a circular domain 103

mode that corresponds with an eigenvalue of $\gamma = j_{31}$. Other examples of $m = 3$ periodic solutions are given in Fig. 5.18.

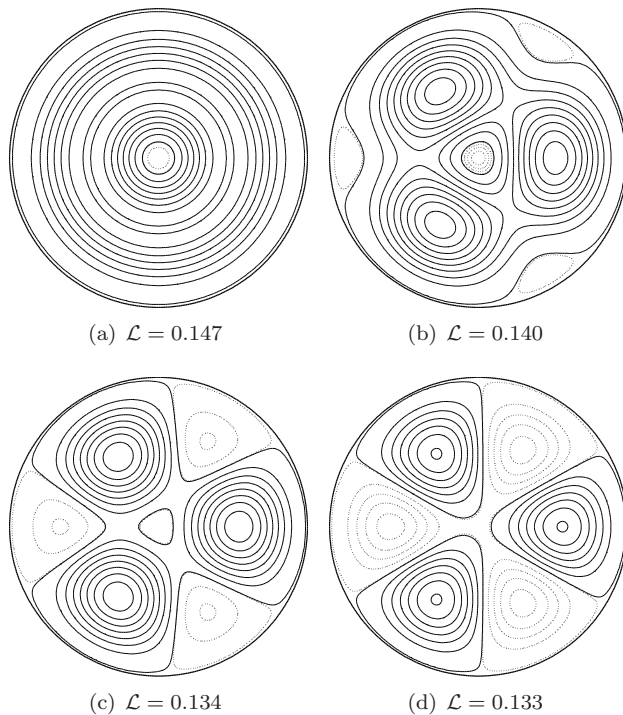


Figure 5.18 – Branch of solutions for $(3, 1)$. Angular momentum $L = 0.577$ (a), 0.453 (b), 0.261 (c) and 0.0723 (d).

Chapter 6

Spin-up in an elliptic geometry ⁱ

6.1 Introduction

Many characteristic phenomena of two-dimensional (2D) turbulence, such as the formation of coherent structures, vorticity filamentation, the turbulent dual cascades, are usually analyzed theoretically or studied numerically in the absence of rigid boundaries. Moreover, in experimental studies it is often assumed that rigid walls are located at a sufficient distance from the measurement area so that any influence of the walls is assumed negligible. Interaction of 2D flows with a no-slip boundary can, however, dramatically affect the evolution of both decaying and forced 2D turbulence, see for a recent overview [40]. In the present chapter we focus on the spontaneous production of angular momentum L (the precise definition will follow), and associated spontaneous symmetry breaking of the flow, due to the interaction of decaying 2D turbulence with elliptical, no-slip sidewalls.

One of the first remarkable results in this field hinting at the special role of the angular momentum were obtained numerically by Li *et al.* [60, 62]. These authors reported that the decay scenario of 2D turbulence in a circular geometry with a no-slip boundary strongly depends on the net angular momentum contained by the initial flow field. Any angular momentum production due to flow-wall interactions seems insignificant for this particular geometry. It was found that the late-time state strongly depends on the amount of angular momentum introduced during the initialization of the flow. In particular, an initial flow field without significant angular momentum yields after a rapid self-organization process a quadrupolar structure filling the circular container. This structure eventually evolves towards a dipolar structure in the late-time flow evolution. On the other hand, an initial turbulent velocity field containing some net angular momentum evolves into a

ⁱThe contents of this chapter is an adapted version of Keetels *et al.* [47]

large monopolar structure that eventually fills the entire container. The numerical predictions of Li *et al.* [61, 62] have been confirmed experimentally by Maassen *et al.* [65]. Typical initial integral-scale Reynolds numbers in the numerical and experimental studies were $\text{Re} = UW/\nu \approx 2 \times 10^3$, with U the rms velocity, W the size of the container, and ν the kinematic viscosity of the fluid.

Similar simulations and experiments have been conducted for decaying 2D turbulence in square domains by Clercx *et al.* [19, 21]. These studies gave an essentially different picture. It was observed that the no-slip boundaries of the square container exert a net torque on the fluid such that the flow, which has initially no significant amount of angular momentum, acquires angular momentum during the decay process. As a consequence, rapid production of angular momentum can result in a large monopolar or tripolar vortex completely filling the domain later on in the flow evolution, a clear sign of spontaneous symmetry breaking of the flow. It was reported that in an ensemble of simulations with an initial Reynolds number of $\text{Re} = 2 \times 10^3$ a part of the runs showed strong spin-up effects [19]. However, for an ensemble of runs with initially $\text{Re} = 10^4$ revealed that all the simulations show a flow evolution following the scenario with sudden and strong spin-up [21], although the flow in the container after it has spun up consists basically of a sea of smaller-scale vortices on top of a domain-filling swirling flow. Approximately one half of the runs showed the emergence of a clockwise swirl, and the other half an anti-clockwise motion, thus on average symmetry breaking is absent, as is to be expected.

6.2 Angular momentum production

In a recent study of the circular case [96] it was shown that the production of angular momentum on a circle is negligible for higher Reynolds numbers, up to $\text{Re} = 5 \times 10^4$, as well. Montgomery [73] suggests, that the elliptical geometry in particular would be a good starting point to further investigate the behaviour of bounded 2D fluids. A hint to explain the dramatic influence of the shape of the no-slip boundary may be found in the angular momentum balance,

$$\frac{dL}{dt} = \frac{1}{\rho} \oint_{\partial\mathcal{D}} p(\mathbf{r}, t) \mathbf{r} \cdot d\mathbf{s} + \frac{1}{\text{Re}} \oint_{\partial\mathcal{D}} \omega(\mathbf{r}, t) (\mathbf{r} \cdot \mathbf{n}) ds \quad (6.1)$$

where the angular momentum is defined as

$$L = \int_{\mathcal{D}} \mathbf{r} \times \mathbf{u} dA = \int_{\mathcal{D}} (xv - yu) dA. \quad (6.2)$$

Here, we introduced a Cartesian coordinate system (x, y) with origin in the centre of the container, and $\mathbf{u} = (u, v)$ with respect to this coordinate system. Furthermore, p represents the pressure, ρ is the fluid density and $\omega = \frac{\partial v}{\partial x} - \frac{\partial u}{\partial y}$ is the vorticity associated with the 2D velocity field \mathbf{u} . The first term on the right-hand

side of (6.1) represents the pressure contribution and the second term the effect of viscous shear and normal stresses. An important result can directly be conjectured from (6.1): the pressure term is essentially zero on the boundary of the circular domain, since $\mathbf{r} \cdot d\mathbf{s} \equiv 0$. This signifies that although the pressure distribution over the domain boundary may be asymmetric it does not yield a net torque to the interior fluid. For flows on the square domain it is, however, reported by Clercx *et al.* [21] that it is essentially the pressure term that guides the spin-up process as it is orders of magnitude larger than the viscous stress contribution represented by the second term on the right-hand side in (6.1).

To investigate the generalization towards an elliptic geometry it is useful to represent (6.1) in the cylindrical elliptic coordinate system (η, ξ) , where a constant ξ and variable η in the range $0 < \eta < 2\pi$ describe an elliptic curve. For convenience we keep the major-axis $a \equiv 1$ while the minor-axis $b = 1 - \delta$ is in the range $0 < b \leq 1$ in the following. The angular momentum balance then reads,

$$\frac{dL}{dt} = \frac{\delta(\delta - 2)}{2\rho} \oint_{\partial D} p(\eta) \sin(2\eta) d\eta + \frac{(1 - \delta)}{\text{Re}} \oint_{\partial D} \omega(\eta) d\eta. \quad (6.3)$$

The pressure term in (6.3) is of order δ and will grow linearly with the deviation from the circle geometry. The contribution of the viscous stresses remains small. Note that in an elliptic geometry a broken symmetry in the pressure distribution over the domain boundary can, in principle, yield a global spin-up of the fluid in the interior. Summarizing: by making a small change δ from a circular to an elliptic geometry we can tune the relative contribution of the pressure term and the viscous stresses in the angular momentum balance.

For normalization of the angular momentum it is important to know the maximum amount of angular momentum that can be present on an elliptic domain for a given amount of the total kinetic energy $E = \frac{1}{2} \int_D (u^2 + v^2) dA$. For arbitrary geometries (and irrespective of the boundary conditions) it is helpful to introduce a limit to the angular momentum with a Schwarz inequality yielding,

$$L \leq \|\mathbf{r}\|_2 \|\mathbf{u}\|_2 = \|\mathbf{r}\|_2 \sqrt{2E} \quad (6.4)$$

where $\|\cdot\|_2$ denotes the L_2 norm. The right-hand side of inequality (6.4) equals the amount of angular momentum if the fluid is in solid body rotation. Impermeability of the elliptic boundary prevents that the fluid can obtain a full solid body state. It is, however, possible to derive an upper bound for the angular momentum that is consistent with the impermeability of the elliptic boundary. By virtue of the incompressibility condition $\nabla \cdot \mathbf{u} = 0$ we can introduce a stream function according to $u = \partial_y \psi$ and $v = -\partial_x \psi$. An impermeable boundary can be modelled by setting $\psi = 0$ at the boundary. Now it is convenient to reformulate the angular momentum and total kinetic energy as $L = 2 \int_D \psi dA$ and $E = \frac{1}{2} \int_D \omega \psi dA$. Using standard variational techniques [2] it is straightforward to show that the variational problem $L[\psi]$ with constraint $E[\psi] = 1$ yields a Poisson equation, $\nabla^2 \psi = -2\Omega$ with $\psi = 0$ on the boundary. The Lagrange multiplier Ω equals the angular velocity in the

case of solid body rotation on the circle. The solution normalized with the amount of angular momentum of the same fluid in solid body rotation reads,

$$\tilde{L} = \frac{2}{b/a + a/b} \quad (6.5)$$

where a and b represent the major and minor half-axes of the ellipse, respectively. Fig. 6.1 shows the solutions of the Poisson problem on the ellipse and the corresponding upper bound for the angular momentum. The streamline pattern has the appearance of a single cell filling the entire container.

Keeping in mind the tendency to axisymmetrization of a domain filling vortex, we also consider an alternative streamline pattern (Fig. 6.1, bottom). It is computed by a conformal map (modified Joukowski) of solid body rotation on a circle to an elliptic geometry. A single concentric cell appears in the centre, while the streamlines become eccentric when moving radially outward.

Both patterns show that for small deviations of the minor-axis from the unit circle ($b > 0.7$) the amount of angular momentum that can be reached is more than 90% of solid body rotation. For larger eccentricities, i.e. $\delta \gtrsim 0.3$, on the other hand, the angular momentum vanishes much faster. Recall that the upper bound is derived by only demanding impermeability of the boundary, allowing a free-slip velocity at the boundary. Incorporation of a no-slip boundary condition in the variational problem is not possible. Demanding an extra condition, i.e. zero circulation, $\Gamma = \int_{\mathcal{D}} \omega dA = 0$, yields the same Poisson equation though with Cauchy boundary conditions, which are too restrictive on a closed surface [2].

6.3 Numerical method

The numerical results are obtained by a Fourier spectral solver combined with an immersed boundary technique, known as “volume-penalization” or “Brinkman penalization” to incorporate the no-slip boundary condition. The concept proposed by Arquis & Caltagirone [3] is to model a solid obstacle with no-slip boundaries as a porous obstacle with an extremely small permeability. The flow domain Ω_f is embedded in a computational domain Ω , such that $\Omega_f = \Omega \setminus \overline{\Omega_s}$, where Ω_s represents the volume of the porous objects. The interaction with the porous objects is modelled by adding a Darcy drag term to the incompressible Navier-Stokes equations locally inside Ω_s . This gives the penalized Navier-Stokes equation defined for $\mathbf{x} \in \Omega$

$$\partial_t \mathbf{u} + (\mathbf{u} \cdot \nabla) \mathbf{u} + \nabla p - \nu \Delta \mathbf{u} + \frac{1}{\epsilon} H \mathbf{u} = 0, \quad (6.6)$$

which are accompanied by the continuity equation for $\mathbf{x} \in \Omega$

$$\nabla \cdot \mathbf{u} = 0, \quad (6.7)$$

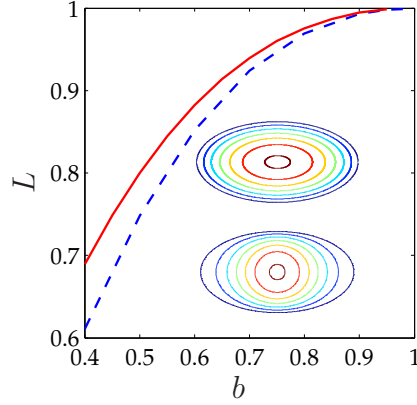


Figure 6.1 – Upper bound (solid line) for the angular momentum in an elliptic geometry, normalized with angular momentum of the fluid in solid body rotation, versus size of the minor half-axis b while the major half-axis $a = 1$ is fixed. Inset shows the streamlines for $b = 0.5$ for the Poisson solution (top) and the streamlines obtained by conformal mapping of a uniform rotation on the circle to an ellipse (bottom). The dashed line denotes angular momentum of the conformal mapping result.

where ϵ is the penalization parameter and H represents a mask function defined as

$$H = \begin{cases} 1 & \text{if } \mathbf{x} \in \overline{\Omega_s} \\ 0 & \text{if } \mathbf{x} \in \Omega_f. \end{cases}$$

Note that inside the obstacle Ω_s Darcy drag is added and inside the flow domain Ω_f the usual Navier-Stokes equations is considered. The initial velocity is defined inside the flow domain Ω_f . Inside the obstacle the initial condition can be extended to the porous obstacle by setting the initial velocity equal to zero inside the domain Ω_s . As a result, the initial condition is properly defined on the entire computational domain Ω . In this study the mask function is chosen such that the elliptic flow domain is sufficiently embedded inside the computational domain Ω . By simply changing the shape of the mask function it is possible to solve another elliptic geometry with a different eccentricity. This is employed by fixing the major half-axis $a = 1$ and varying the minor-axis b . In contrast to other immersed boundary techniques the method is fully theoretically justified [14], [1]. The penalization error is proportional to $\sqrt{\epsilon}$. Various numerical benchmark studies are available [1, 51, 92] and some 2D turbulence studies have already adopted the method [12, 96]. The Fourier-spectral scheme with volume-penalization applied in the present study is validated by a detailed convergence analysis on vortex-wall collisions [48]. It was found that it is possible to make the penalization error smaller than the truncation error. Note that the penalization parameter is actually an arbitrary parameter. If an appropriate time-scheme is applied unusual restrictions on the time-step are

avoided as well.

Important features of the method are the straightforward implementation of (curved) no-slip boundaries and the efficient computation of 2D turbulence on arbitrary closed domains with parallelized Fourier pseudospectral codes. The flow is initialized by the same procedure as used in the study of Clercx *et al.* [21] on spontaneous angular momentum production in a square geometry. The initial condition consists of 100 nearly equal-sized Gaussian vortices with a radius 0.05 normalized with the major half-axis a of the ellipses ($a = 1$) and vortex amplitude $\omega_{max} \simeq 100$ normalized with rms velocity $U = 1$ and the major half-axis. Half of the vortices have positive circulation and the other vortices have negative circulation. The vortices are placed on a regular lattice, well away from the boundaries. The symmetry is slightly broken by slight displacement of the vortex centres. In Fourier transform space certain coefficients are set equal to zero, such that the initial angular momentum is zero within machine precision. A smoothing function [21] is applied to ensure that the initial flow is consistent with the no-slip boundary condition.

The ensemble simulations are conducted with a total number of 1024^2 Fourier modes. The penalization parameter is $\epsilon = 10^{-8}$ and the time-step is $\delta t = 10^{-4}$. The following values for minor half-axis b have been considered: $b = 1.0, 0.95, 0.9, 0.8$ and 0.7 . For each case 12 ensemble runs are performed. The flow is initialized such that the rms velocity $U = 1$. The majority of the runs has an initial Reynolds number of $Re = aU/\nu = 10^4$. For one case, $b = 0.9$, the Reynolds number is increased to $Re = 2 \times 10^4$. These runs require a larger resolution up to 2048^2 Fourier modes. To check if convergence is achieved lower spatial resolution computations have been performed for the same initial condition for each value of the minor-axis b . Furthermore, it is verified that the enstrophy dissipation length scale, defined as $2\pi (\nu^3/\chi)^{1/6}$, with χ denoting the enstrophy dissipation rate per unit area, is well resolved. The required resolutions are consistent with the convergence study of the numerical scheme based on vortex-wall interaction [46, 48].

6.4 Decaying 2D turbulence in elliptic geometries

Snapshots of the vorticity field from a decaying turbulence simulation in an elliptic domain with minor-axis $b = 0.8$ are displayed in Fig. 6.2. The initial integral-scale Reynolds number is $Re = 10^4$, which eventually decreased to $Re \approx 2 \times 10^3$ at the end of the simulation. The first stage of the decay process is characterized by intense vortex-wall interactions and vortex merger events in the interior of the flow domain. Later the vortex density decreases, while a large-scale monopolar vortex starts to fill the interior of the elliptic domain. In Fig. 6.3 the Reynolds number $Re = aU/\nu = a\sqrt{2E(t)}/ab\pi/\nu$ and integral length scale $\mathcal{L}(t) = \sqrt{E(t)/Z(t)}$ (where $Z(t) = \frac{1}{2} \int_{\mathcal{D}} \omega^2 dA$ denotes the total enstrophy) are given. The Reynolds number is larger than 2000 for $\tau < 500$, implying that the large-scale vortex develops in the non-linear regime. (Note for $\tau \rightarrow \infty$ the flow is finally governed

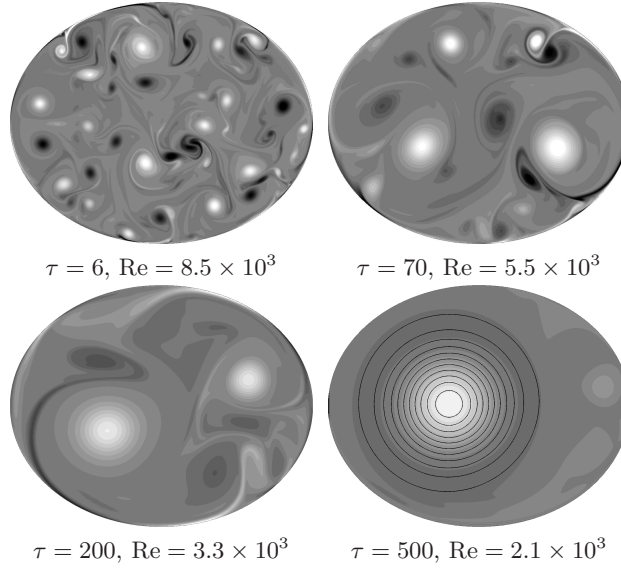


Figure 6.2 – Vorticity plots of a run with an initial Reynolds number $Re = 10^4$ and minor-axis $b = 0.8$. White indicates positive vorticity, black negative. For $\tau = 500$ also the contour lines of the stream function ψ are shown with an increment of 0.02. Time is made dimensionless by the turnover time of the initial vortices. Spatial resolution is 1024^2 .

by viscous dynamics, which selects the slowest dissipating mode or fundamental Stokes mode.) The integral length scale grows very rapidly in the beginning of the simulation due to merger events and dissipation of enstrophy in the interior. The growth rate of the integral length scale is suppressed between $80 < \tau < 300$ due to production of enstrophy at the domain boundaries. Finally the integral length scale increases rapidly, which can be associated with the relaxation to the large-scale vortex in Fig. 6.2 at $\tau = 500$.

Note that the emergence of a large monopolar vortex in the interior of the flow domain, as shown in Fig. 6.2, inevitably implies a net angular momentum. The angular momentum can be normalized by using $L_{sb} = \|\mathbf{r}\|_2 \|\mathbf{u}\|_2$ with $\|\mathbf{r}\|_2 = \frac{1}{2} \sqrt{b(1+b^2)\pi}$ and $\|\mathbf{u}\|_2 = \sqrt{2E}$ either determined by the initial energy E_0 or the instantaneous energy $E(t)$. The first normalization does not take into account viscous dissipation, and although the normalized angular momentum will be virtually constant after spin-up, it eventually decays to zero as the flow dissipates. On the other hand, the second normalization procedure compensates for viscous decay, and in the long-time limit ($\tau \gg 10^3$) the normalized angular momentum will always approach a certain finite value due to viscous relaxation. Fig. 6.4 shows the normalized angular momentum versus time for two sizes of the minor-axis. Note

that the left-hand panel in Fig. 6.4 shows the corresponding curves for the run presented in Fig. 6.2. It can be observed in Fig. 6.4 that the angular momentum normalized with $L_{sb} = \|\mathbf{r}\|_2 \sqrt{2E_0}$ (solid line) is produced early in the evolution and becomes more or less constant after $\tau \gtrsim 300$. Note that in this paper the quasi-stationary end-state of the non-linear regime is considered. In the limit of $\tau \rightarrow \infty$ the angular momentum will eventually vanish due to viscous decay. The

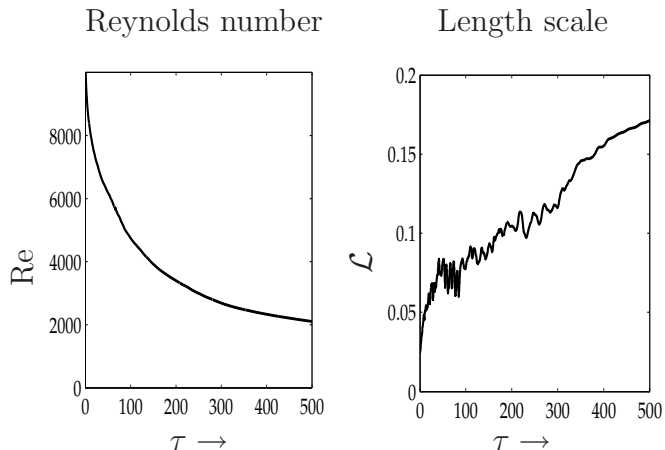


Figure 6.3 – Reynolds number Re and the integral length scale \mathcal{L} of the simulation shown in Fig. 6.2.

corresponding curve for the angular momentum of the run shown in Fig. 6.2 normalized with $L_{sb}(t) = \|\mathbf{r}\|_2 \sqrt{2E(t)}$ (dashed line) reveals that at $\tau = 500$ more than 70% of uniform-like rotation has been reached. All runs for $b = 0.8$ show fairly rapid spin-up followed by a slow spin-down due to long-term dissipation. While the total kinetic energy is continuously dissipated the flow maintains normalized angular momentum by assuming a more uniform-like rotation. The oscillations of the angular momentum, as observed in several runs during the spin-up process in an elliptic geometry with minor axis $b = 0.8$, are related to the formation of a domain-sized tripole that interacts with the domain boundary. This phenomenon has been observed and explained earlier in the square bounded geometry [21], and we suspect that a similar mechanism is responsible for the oscillations in the angular momentum signal for the flow in the elliptic geometry. The right-hand panel in Fig. 6.4 shows two examples of the angular momentum versus time for $b = 0.9$, so for an ellipsis with a smaller eccentricity. Not all the runs for this case show strong spin-up events (six runs show spin-up with an amplitude of $A \approx 0.5$ and six runs show only weak spin-up, $A \approx 0.2$) and the ensemble averaged amplitude is smaller than for the $b = 0.8$ case. In Fig. 6.5 the vorticity and stream function is given for a run showing strong spin-up and a run with weak spin-up. Note that the

corresponding time series of the angular momentum is presented in the right-hand panel of Fig. 6.4 for the case $b = 0.9$. It can be observed in Fig. 6.5 that a strong spin-up can be associated with the development of a strongly asymmetric dipole. On the other hand, in case of a weak spin-up an asymmetric quadrupole configuration can be recognized inside the elliptic container. Recall, that this quadrupolar structure is also found in the end-state of the non-linear regime (but far from the Stokes regime) in a circular geometry ($b = 1.0$) where spin-up is virtually absent [62, 65, 66, 96]. This observation is confirmed by the present simulations for $b = 1.0$: no runs in the ensemble of 12 runs show spin-up. Spin-up becomes rare for the intermediate case $b = 0.95$ (two runs with amplitude $A \approx 0.3$ in an ensemble of twelve runs).

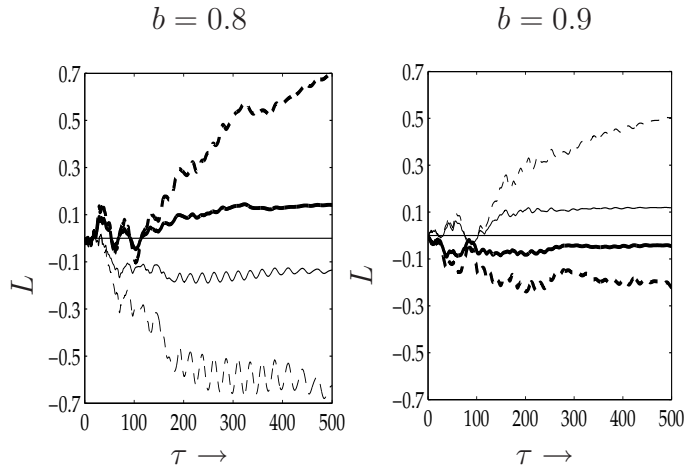


Figure 6.4 – Angular momentum in an elliptic geometry versus time. Angular momentum is normalized with uniform rotation using L_{sb} at $\tau = 0$ (solid line) and $L_{sb}(t)$ (dashed line). Thick lines in left-hand panel correspond with the run shown in Fig. 6.2.

Fig. 6.6 shows the probability density function (pdf) of the derivative of the angular momentum $\dot{L}(t)$, which is essentially equal to the net torque on the container. It can be deduced from this figure that on average the net torque is Gaussian distributed (the histogram of the torque of a specific run can strongly deviate from Gaussian behaviour, especially on the tails of the distribution). Table 6.1 reports the ensemble averaged amplitude $\langle A \rangle$ and standard deviation σ of the derivative of the angular momentum. The standard deviation σ of the Gaussian fit curves corresponds to the second-order moment of the ensemble averaged distribution. It appears that σ depends linearly on the deviation of b from the unit circle for $\delta = 1 - b \lesssim 0.2$. Recall, that this scaling behaviour can be related to the prefactor (proportional to δ) in the pressure contribution in (6.3). The standard deviation

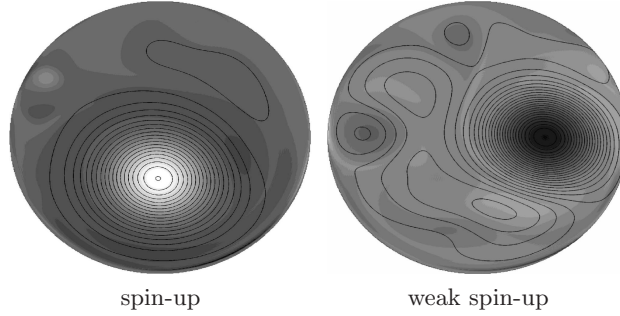


Figure 6.5 – Vorticity and stream function of two runs with slightly different initial conditions in an elliptic geometry with minor-axis $b = 0.9$ at $\tau = 500$. The run in the left-hand panel shows a strong spin-up event (corresponding with the thin lines in Fig. 6.4 case $b = 0.9$), while the run shown in the right-hand panel shows only weak spin-up (corresponding with the thick lines in Fig. 6.4 case $b = 0.9$). White indicates positive vorticity and black negative vorticity. For both runs the vorticity ranges from $\omega = -5$ to $\omega = +5$. Isolines represent the stream function with an increment of 0.01.

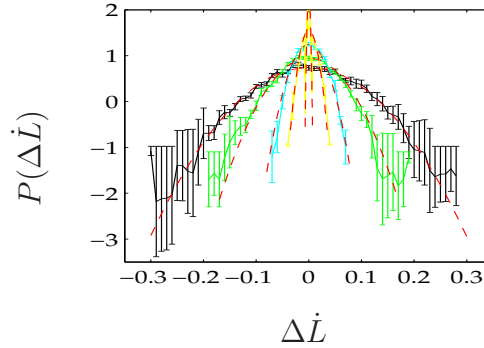


Figure 6.6 – Semi-logarithmic plot of the pdf (solid lines) of $\dot{L}(t)$ for different sizes of minor-axis b . The first pdf in the centre corresponds with $b = 1.0$, when moving outward b equals 0.95, 0.9, 0.8, 0.7, respectively. The pdf is averaged over a time interval $\tau = [5, 100]$. Error bars are based on runs in an ensemble of 12 runs for each value of b . Gaussian fit (dashed) to the ensemble averages.

for the case $b = 0.7$ ($\delta = 0.3$) seems (considering a 10 % error margin in σ) to be larger than expected from the prefactor alone. Note that a spin-up of the flow could enhance symmetry breaking on the domain boundary and thus increase, in return, the magnitude of the pressure contribution in (6.3).

In order to investigate the Reynolds number dependence, a smaller number of ensemble runs is performed for $\text{Re} = 2 \times 10^4$ with the minor-axis $b = 0.9$. It is

observed that the intensity of the spin-up process does not increase significantly. The standard deviation of \dot{L} determined over the same time-interval as used in Fig. 6.6 is $\sigma_{\dot{b}=0.9} = 2.5 \times 10^{-2}$, which lies within a ten percent error margin of σ computed for $\text{Re} = 10^4$. Furthermore, the frequency of strong spin-up events (four) within the ensemble (nine runs) is also similar to the $\text{Re} = 10^4$ case.

6.5 Conclusion

The results presented in this paper are helpful to understand the strikingly different behaviour of the angular momentum in square versus circular geometries. By using a novel volume-penalization technique it is possible, starting with a circular geometry, to gradually introduce some eccentricity. It is demonstrated that a small transition from the circle results in a linear increase of the magnitude of the torque (in terms of the standard deviation), which can be related to the relative importance of the pressure contribution in the balance that guides the angular momentum production. In this respect the observations reported on the absence of significant spin-up in a circular geometry and the associated ambivalence in the end-state [60, 62, 96] are robust, *i.e.* the eccentricity cannot be regarded as a bifurcation parameter in this respect. Recall that it might be conjectured that introduction of very small eccentricity may result in a symmetry breaking of the flow and significantly enhance the magnitude of the integral over the domain boundaries in (6.3). Apparently it is, however, the prefactor in front of the pressure contribution in (6.3) that tunes the magnitude of the torque and in addition the strength of the spin-up. When moving from a circular towards a non-circular geometry this gives a gradual transition from virtually no spin-up towards a regime where all the runs in an ensemble with slightly different initial conditions show strong and rapid spin-up events. Between those limiting cases there exists a critical sensitivity to the initial conditions. Some runs in the ensemble show strong spin-up, whereas the other runs in the ensemble demonstrate very weak or virtually no spin-up. Recall that the initial flow of all the ensemble runs does not contain angular momentum within machine precision accuracy. Small variation of the initial conditions are introduced by a slight displacement of the core of the Gaussian vortices on a regular lattice. It is surprising that these small differences in the initial conditions can result in a markedly different end-state of the decay process. The number of spin-up events increases significantly for increasing eccentricities.

In previous reports it is anticipated that the pressure contribution depends only weakly on the Reynolds number, since the pressure will obviously reach finite values in the limit of infinite Reynolds numbers [21]. The analysis of the torque for the ensemble study at a significantly higher Reynolds number ($\text{Re} = 2 \times 10^4$) supports this conjecture. In addition, the probability that the flow will demonstrate strong and rapid spin-up is not markedly affected by the Reynolds number of the flow. It may be interesting to note that apparently the discontinuity of the domain

Table 6.1 – Statistics of the spin-up for different values of the minor-half axes b . Ensemble averaged amplitude $\langle A \rangle$ defined as the maximum for $\tau < 500$ of the normalized angular momentum $L_{sb}(t)$. Conditional average $\langle A \rangle_c$ over the runs in the ensemble that show strong spin-up of the flow. Standard deviation σ of \dot{L} for different sizes of the minor-axis b . The error in $\langle A \rangle$ is 20 % and in σ 10%. Number of runs $\#$ in an ensemble of twelve runs showing relatively strong spin-up of the flow.

b	1.0	0.95	0.9	0.8	0.7
$\langle A \rangle$	0.07	0.17	0.31	0.58	0.68
$\langle A \rangle_c$	-	0.29	0.52	0.58	0.68
σ	0.002	0.011	0.022	0.045	0.073
$\#$	0	2	6	12	12

boundaries (corners) is not essential for breaking the symmetry of the flow. By changing the eccentricity it is possible to tune the relative importance of the pressure and viscous stresses in the angular momentum balance. The present study convincingly shows that angular momentum production is essentially due to the pressure contribution at the boundaries. As a consequence, the results of statistical mechanical studies that usually consider inviscid flow with free-slip boundaries may be more generally relevant for the quasi-stationary final states of viscous flow in bounded domains with no-slip sidewalls, though in a qualitative sense. A statistical mechanical prediction of the quasi-stationary end-state of inviscid flow in an elliptic geometry with free-slip boundaries, in the spirit of Pointin and Lundgren [87] and Chavanis and Sommeria [16], would therefore be an interesting endeavor.

6.A Appendix: angular momentum in an elliptic geometry

For appropriate normalization it is important to know the maximum amount of angular momentum $L = \int_{\mathcal{D}} \mathbf{r} \times \mathbf{u} dA = \int_{\mathcal{D}} (xv - yu) dA$ that can be present on an elliptic domain for a given amount of the total kinetic energy $E = \frac{1}{2} \int_{\mathcal{D}} (u^2 + v^2) dA$. Here, we use a Cartesian coordinate system (x, y) with origin in the centre of the container, and $\mathbf{u} = (u, v)$ with respect to this coordinate system. For arbitrary geometries (and irrespective of the boundary conditions) an absolute upper bound for the angular momentum is obtained by applying a Schwarz inequality to the definition of the angular momentum,

$$L \leq \|\mathbf{r}\|_2 \|\mathbf{u}\|_2 = \|\mathbf{r}\|_2 \sqrt{2E} \quad (6.8)$$

where $\|\cdot\|_2$ denotes the L_2 norm. The upper bound, on the right-hand side of (6.8), represents the angular momentum of the fluid with an equal amount of kinetic energy in solid-body rotation. From inequality (6.8) follows that the amount

of angular momentum of a flow pattern which satisfies the the impermeability condition at the boundary is equal to or less than the angular momentum of an equi-energy solid-body state. Note that a circular domain is special in this respect, since a solid-body rotation of the fluid satisfies already the impermeability condition. In other geometries, the impermeability of the boundaries prevents that the fluid can obtain a full solid-body state. Therefore, the maximum amount of angular momentum that can be contained in the flow is reduced. In this section the upper bound for the angular momentum is derived that is consistent with the impermeability of the elliptic boundary.

By virtue of the incompressibility condition $\nabla \cdot \mathbf{u} = 0$ we can introduce a stream function according to $u = \partial_y \psi$ and $v = -\partial_x \psi$. It is convenient to rewrite the angular momentum as

$$L = 2 \int_{\mathcal{D}} \psi dA, \quad (6.9)$$

and the total kinetic energy as,

$$E = \frac{1}{2} \int_{\mathcal{D}} \omega \psi dA, \quad (6.10)$$

where the vorticity associated with the velocity field \mathbf{u} is $\omega = \frac{\partial v}{\partial x} - \frac{\partial u}{\partial y} = -\Delta \psi$. The variational problem is to find a stationary value for the integral

$$L[\psi] = \int_{\mathcal{D}} f(\psi) dA, \quad (6.11)$$

with the constraint in the total kinetic energy,

$$E[\psi] = \int_{\mathcal{D}} \phi(\psi, \psi_{xx}, \psi_{yy}) dA \equiv 1. \quad (6.12)$$

with $f(\psi) = 2\psi$ and $\phi(\psi, \psi_{xx}, \psi_{yy}) = \frac{1}{2}\omega\psi = -\frac{1}{2}\psi\Delta\psi$. The notation ψ_x means the derivative of ψ in the x -direction. Using a Lagrange multiplier λ it is possible to absorb the constraint in the total variation of $L[\psi]$, yielding

$$\delta \left(\int_{\mathcal{D}} [f(\psi) + \lambda \phi(\psi, \psi_{xx}, \psi_{yy})] dA \right) = 0. \quad (6.13)$$

Treating the integrand as a new function $g(\psi_{xx}, \psi_{yy}, \psi) = f(\psi) + \lambda \phi(\psi_{xx}, \psi_{yy}, \psi)$ gives the Euler-Lagrange equation [2] for this particular problem

$$\frac{\partial g}{\partial \psi} + \frac{\partial^2}{\partial x^2} \frac{\partial g}{\partial \psi_{xx}} + \frac{\partial^2}{\partial y^2} \frac{\partial g}{\partial \psi_{yy}} = 0. \quad (6.14)$$

Straightforward substitution of g gives a Poisson problem

$$\Delta \psi = \frac{2}{\lambda} = -2\Omega \quad \text{on} \quad \mathcal{D}, \quad (6.15)$$

where $\Omega = -1/\lambda$ equals the angular velocity in the case of solid-body rotation. A unique, stable solution of the Poisson problem exists for either a Dirichlet or a Neumann boundary condition. Impermeability of the domain boundaries requires the Dirichlet condition ψ to be constant along the boundary. For convenience we choose

$$\psi = 0 \quad \text{on} \quad \partial\mathcal{D}. \quad (6.16)$$

To solve the Poisson problem in an elliptic geometry it is helpful to use elliptical coordinates.

$$x = c \cosh\xi \cos\eta, \quad y = c \sinh\xi \sin\eta \quad (6.17)$$

for $0 \leq \xi < \infty$ and $0 \leq \eta < 2\pi$. A constant value for ξ corresponds with an ellipse with major half-axes a and minor half-axes b

$$a = c \cosh\xi, \quad b = c \sinh\xi. \quad (6.18)$$

Increasing η monotonously from $\eta = 0$ towards $\eta = 2\pi$ describes a counter-clockwise cycle over the ellipse, see Fig. 6.7. The parameter c is the distance between the foci of the confocal ellipses described by the elliptic coordinates.

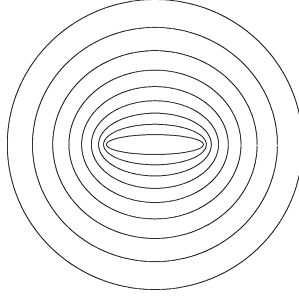


Figure 6.7 – Illustration of the elliptical coordinates (6.17). Isolines for ξ is constant. The contourlines are shown with an increment size of +0.2. The contour line in the centre corresponds with $\xi = 0.2$. Larger values of ξ correspond with ellipses with larger axes and smaller eccentricity.

In elliptical coordinates the Poisson problem on the ellipse can be written as,

$$\frac{1}{h_\xi^2}(\psi_{\xi\xi} + \psi_{\eta\eta}) = -2\Omega \quad \text{for} \quad 0 \leq \xi \leq \xi_b, \quad 0 \leq \eta < 2\pi \quad (6.19)$$

where $h_\xi^2 = c^2(\cosh^2\xi - \cos^2\eta)$ is the scale factor between the Cartesian and elliptical coordinate systems and ξ_b describes the elliptic boundary. The impermeability condition is applied at the boundary,

$$\psi = 0 \quad \text{for} \quad \xi = \xi_b, \quad 0 \leq \eta < 2\pi. \quad (6.20)$$

Periodic boundary conditions are considered in the η -direction

$$\psi(\xi, \eta - \pi) = \psi(\xi, \eta + \pi) \quad \text{for} \quad 0 \leq \xi \leq \xi_b, \quad 0 \leq \eta < 2\pi. \quad (6.21)$$

In addition it is required that for $\xi = 0$

$$\begin{aligned} \psi(0, \eta) &= \psi(0, -\eta) & \text{for} & \quad 0 \leq \eta < 2\pi \\ \psi_\xi(0, \eta) &= -\psi_\xi(0, -\eta) & \text{for} & \quad 0 \leq \eta < 2\pi. \end{aligned} \quad (6.22)$$

Note that as $\xi \rightarrow 0$, the ellipse becomes more elongated until at $\xi = 0$ it converges to the line segment between the foci. The conditions on ψ for $\xi = 0$ imply continuity of ψ and the derivative in the ξ -direction (note that the direction of the ξ derivative above and under the line segment between the foci is defined in opposite directions). By using the particular solution $\tilde{\psi} = -\frac{\Omega c^2}{4}(\cosh 2\xi + \cos 2\eta)$ of (6.19) (which does not fulfill the boundary condition at ξ_b) it is possible to transform the Poisson problem to a Laplace problem:

$$\begin{aligned} \psi_{\xi\xi} + \psi_{\eta\eta} &= 0 & \text{for} & \quad 0 \leq \xi \leq \xi_b, \quad 0 \leq \eta < 2\pi \\ \psi &= \frac{\Omega c^2}{4}(\cosh 2\xi_b + \cos 2\eta) & \text{for} & \quad \xi = \xi_b, \quad 0 \leq \eta < 2\pi \end{aligned} \quad (6.23)$$

which also needs to fulfill the matching conditions (6.21) and (6.22). By using separation of variables it is straightforward to derive the general solution of the Laplace equation in elliptical coordinates, yielding

$$\begin{aligned} \psi(\xi, \eta) &= \alpha_0 + \sum_{m=1}^{\infty} (\alpha_m \cos(m\eta) e^{m\xi} + \\ &\beta_m \sin(m\eta) e^{m\xi_b} + \delta_m \cos(m\eta) e^{-m\xi} + \gamma_m \sin(m\eta) e^{-m\xi}). \end{aligned} \quad (6.24)$$

Note that the periodicity in the η -direction is already included in (6.24). The matching conditions at $\xi = 0$ further require $\beta_m = -\gamma_m$ and $\alpha_m = \delta_m$ for all m . Finally, by applying the orthogonality of the system $\{1, \cos(m\eta), \sin(m\eta)\}$ and the boundary condition at $\xi = \xi_b$ all the coefficients can be determined. Summing the solution of the homogeneous solution (Laplace) and the particular solution $\tilde{\psi}$ yields the solution of the Poisson problem (6.19):

$$\psi = \frac{\Omega c^2}{4}(\cosh(2\xi_b) - \cosh(2\xi) + \cos(2\eta)) \left[\frac{\cosh(2\xi)}{\cosh(2\xi_b)} - 1 \right]. \quad (6.25)$$

The angular momentum can be computed by integration of (6.25), yielding

$$L = \frac{\Omega \pi c^4}{16} \left(\frac{\sinh 4\xi_b}{2} - \tanh 2\xi_b \right). \quad (6.26)$$

Recall that the absolute upper bound of the fluid irrespective of the boundary conditions is given by the Schwarz inequality (6.8). Therefore it is convenient to normalize the angular momentum with $\|\mathbf{u}\|_2 \|\mathbf{r}\|_2$, representing the amount

of angular momentum carried by the fluid in solid-body rotation. By virtue of (6.10) and (6.15) and the definition of the vorticity, the L_2 -norm of the velocity $\|\mathbf{u}\|_2 = \sqrt{2E}$ can be expressed as,

$$\|\mathbf{u}\|_2 = \sqrt{2\Omega L}. \quad (6.27)$$

For $\|\mathbf{r}\|_2$ is straightforwardly obtained that,

$$\|\mathbf{r}\|_2 = \frac{\sqrt{\pi}}{2} \sqrt{ab} \sqrt{a^2 + b^2} = \frac{\sqrt{\pi} c^2}{4} \sqrt{\sinh 4\xi_b}, \quad (6.28)$$

where a and b are the major and minor half-axes of the elliptic boundary with constant $\xi = \xi_b = \operatorname{arctanh}(b/a)$. Now the normalized angular momentum becomes,

$$\tilde{L} = \frac{L}{\|\mathbf{u}\|_2 \|\mathbf{r}\|_2} = \tanh 2\xi_b = \frac{2}{b/a + a/b}. \quad (6.29)$$

Chapter 7

Spin-up at high Reynolds numbers in a square geometry

7.1 Introduction

Both the experiments and numerical simulations at moderate integral-scale Reynolds numbers on a square bounded domain of Clercx *et al.* [19, 21] and Maassen *et al.* [66] have shown that angular momentum produced during the early decay stage results in the formation of a domain-sized monopolar or tripolar vortex structure later in the decay process. The question addressed in this chapter is, whether the spontaneous spin-up process is a feature of the particular range of Reynolds numbers considered in previous studies, viz. $Re = 1000 - 2000$ in Refs. [19, 66] and $Re = 5000 - 20000$ in Ref. [21], or is it a process of fundamental importance for significantly higher integral-scale Reynolds numbers as well? The main conjecture might be that the injection of high-amplitude vorticity filaments emerging from the no-slip boundaries can disrupt the formation of background circulation early in the decay process or prevent the subsequent formation of large-scale vortex structures.

Since vortex-wall interaction is an important process in fully developed 2D turbulence in domains with lateral no-slip walls, the features of individual dipole-wall collisions as considered in chapter one are relevant to consider. In particular the observation that the amount of angular momentum production during an oblique dipole-wall collision does not depend significantly on the initial Reynolds number [18]. This can be related to a finite value of the pressure contribution in the angular momentum balance (1.18) whereas the role of viscous stresses becomes minimal for high Reynolds numbers. Based on the alternative form of the angular

momentum balance (1.19) and the scaling of the vorticity and vorticity gradients at the wall during a dipole-wall collision in the limit of vanishing viscosity proportional to $\text{Re}^{-1/2}$ and Re^{-1} respectively, it can be expected that the pressure contribution in the angular momentum balance becomes finite and the magnitude of the viscous stress term falls with $\text{Re}^{-1/2}$. Since the simulations in an elliptic geometry clearly reveal that it is essentially the pressure term that drives the spin-up it is strongly anticipated that the production of angular momentum is not restricted to a particular range of Reynolds numbers.

In this chapter high-resolution simulations are conducted for fully developed 2D decaying turbulence in order to verify if spin-up is actually present for significantly higher Reynolds numbers than considered previously on a square bounded domain. Several characteristics of the spin-up process are determined for high Reynolds number flow, such as the magnitude of the torque and the resulting spin-up. Furthermore, it is examined if a characteristic dimensionless time can be related to the spin-up of the flow.

7.2 Setup of the simulations

The same type of initial conditions have been applied as considered in the previous chapters on decaying flow. It consists of 100 Gaussian vortices with an equal strength positioned in a checkerboard-like configuration. The initial position of the vortices is slightly distorted by a random displacement in order to break the symmetry, see for more details [21]. The angular momentum of the initial conditions is removed within machine precision accuracy. A smoothing function is applied to ensure that the initial flow is consistent with the no-slip boundary condition. The parameters of the simulations are assembled in table 7.1.

Table 7.1 – Overview of the simulations on a square domain. The Reynolds number Re is based on the rms velocity and half-width of the domain $W = 1$. N denotes the spatial resolution, N_{act} is the number of active Fourier coefficients, ϵ the penalization parameter and δt the time-step.

#	Re	N	N_{act}	ϵ	δt
10	10^4	1024	682	10^{-8}	1.0×10^{-4}
5	5×10^4	2048	1364	10^{-8}	5.0×10^{-5}
5	10^5	4096	2730	10^{-8}	2.5×10^{-5}

7.3 Confined 2D decaying turbulence

Fig. 7.1 shows several snapshots of the vorticity distribution of decaying flow with an initial Reynolds number of $Re = 10^5$. The dimensionless time unit τ represents the number of turnover times of the Gaussian vortices of the initial condition. The vorticity snapshot taken from the vigorous early stage of the turbulent decay process at $\tau = 7$ shows several characteristic features such as merging of like-sign vortices in the centre of the container and the formation of medium-sized dipoles. During several collisions of vortex structures with the domain boundaries high-amplitude vorticity filaments are injected into the interior of the flow domain and roll up into new vortex cores. These new small-scale vortices contain high-amplitude vorticity. The second stage of the decay process, for which a typical example of the vorticity distribution is displayed in Fig. 7.1 at $\tau = 20$, is characterized by the formation of increasingly larger coherent structures. Injection of small-scale vorticity from the no-slip domain boundaries and subsequent formation of new vortex cores continues. Fig. 7.2 gives the stream function that corresponds with the vorticity fields in Fig. 7.1. The streamlines reveal the development of a large-scale flow pattern during the decay process. Since the angular momentum can equivalently be expressed as $L = 2 \int \psi dA$ it is obvious that the flow has acquired net angular momentum. This is strikingly different compared to the final state of decaying turbulence on a periodic domain, for which the angular momentum is trivially zero. As a consequence, the final state of the decay process is a large-scale dipolar vortex structure [70].

The overall picture of the decay process in a no-slip box considered here for $Re = 10^5$ is similar to the $Re = 10^4$ case reported in Clercx *et al.* [21]. An important difference is, however, the presence of a much larger number of (small-scale) vortices in the high-Reynolds number case. The size of these small-scale vortices is substantially less than the size of the Gaussian vortices constituting the initial vorticity field. The diameter of these Gaussian vortices is approximately one-tenth of the container size. To demonstrate that the small-scale vortex structures are indeed a result of flow-wall interaction, a comparison with a numerical simulation on a double periodic domain is shown in Fig. 7.3. The initial condition and the Reynolds number for the periodic computation are the same as for the no-slip case. Note the large number of small-scale vortices distributed over the entire no-slip box. Such small-scale vortices are virtually absent in the periodic case. This observation signifies that these vortices are indeed formed due to flow-wall interaction events.

Also in the late-time evolution several differences are discovered between the present results with $Re = 10^5$ and those with $Re = 10^4$, presented in Clercx *et al.* [21]. Around $\tau = 200$ a monopolar or a tripolar structure emerges that completely fills the domain for $Re = 10^4$. For the high-Reynolds number decay process considered here it is observed that the radius of the dominant vortex structure appearing around the same time is significantly smaller. Also in the late-time evolution the number of vortices in the high Reynolds number case is much larger.

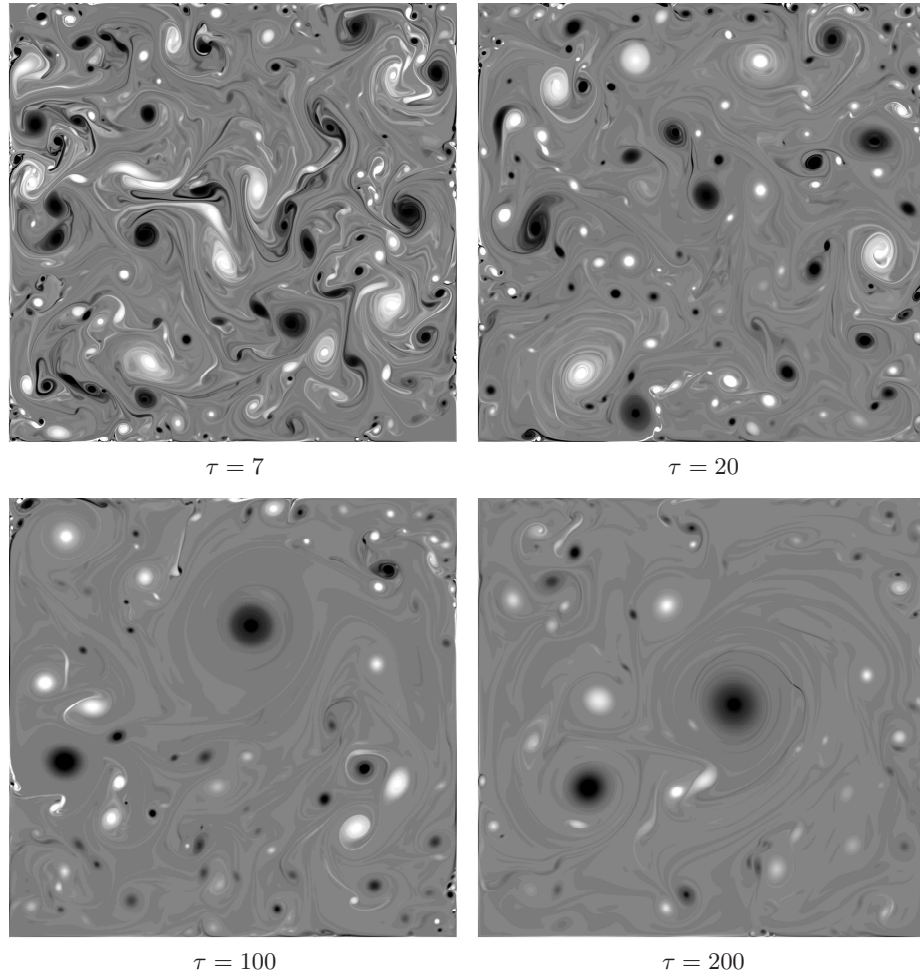


Figure 7.1 – Vorticity snapshots of a simulation with an initial Reynolds number $Re = 10^5$. The simulation is performed with 4096^2 Fourier modes. The time is given in terms of τ , which is the turnover time of the initial vortices positioned in an array of 10×10 vortices (position slightly distorted for breaking symmetry). Thirty grey levels are applied from $\omega = -80$ to $\omega = +80$. The normalized angular momentum is $|L| = 0.01, 0.08, 0.28$ and 0.25 for $\tau = 7, 20, 100$ and 200 , respectively.

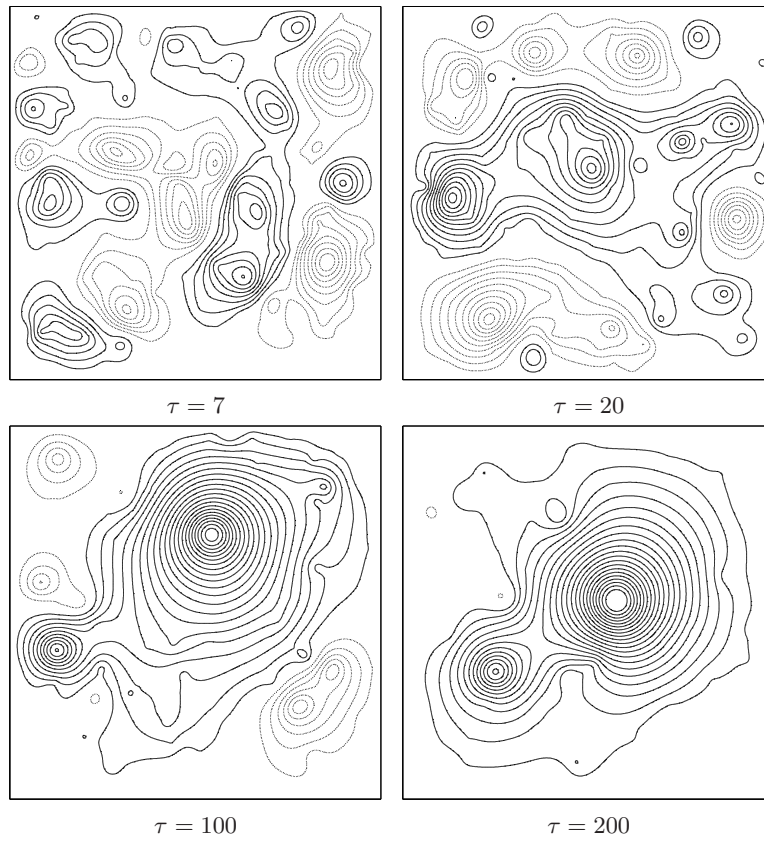


Figure 7.2 – Stream function plots corresponding with the vorticity fields shown in Fig. 7.1. Increments size is 0.04. The normalized angular momentum is $|L| = 0.01, 0.08, 0.28$ and 0.25 for $\tau = 7, 20, 100$ and 200 , respectively.

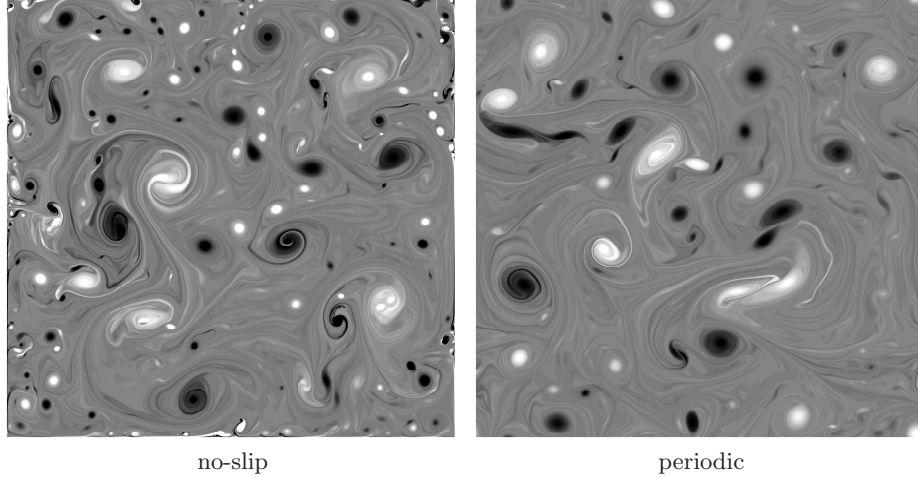


Figure 7.3 – Comparison of vorticity snapshots at $\tau = 15$ from two simulations with (a) no-slip and (b) periodic boundary conditions. The Reynolds number for both simulations is $\text{Re} = 10^5$ and 4096^2 Fourier modes are used. The initial conditions are identical. Red indicates positive vorticity, blue negative vorticity. The vorticity values range from $\omega = -80$ to $\omega = +80$.

Note that although the radius of the dominant vortex is smaller, the associated stream function displayed in Fig. 7.2 reveals the development of a global circulation cell in the interior of the container, which contains net angular momentum. Fig. 7.4 shows the total kinetic energy and enstrophy of the flow versus the dimensionless time τ . During the vigorous first stage of the decay process the energy dissipates very rapidly due to the production of small-scale vorticity at the domain boundaries and consequent increase of the enstrophy, see (1.10) and term T_1 in (1.12). The energy dissipation in the no-slip case is much larger compared with the periodic case. For decaying turbulence on a periodic domain the enstrophy is bounded by its initial value, since the terms T_1 and T_3 in the enstrophy balance (1.12) are absent and $T_2 \leq 0$. This implies that $|\frac{dE(t)}{dt}| \leq \frac{2Z(t=0)}{\text{Re}}$ thus the energy dissipation rate falls off proportional to Re^{-1} in the periodic case. Note that the enstrophy of the flow on a periodic domain, represented by the dotted line in Fig. 7.4b, decays very rapidly due to the vorticity gradient amplification process, see term R_1 in (1.15), and subsequent increase of the term T_2 in (1.12). Due to the production of enstrophy by flow-wall interaction the amount of enstrophy is substantially larger for wall bounded flow. This results in a significantly faster dissipation rate of the total kinetic energy, see Fig. 7.4a.

The enstrophy production of a dipole-wall collision scales proportional to $\text{Re}^{0.75}$ and $\text{Re}^{0.5}$, see (1.45) and (1.46), for moderate and high Reynolds numbers, respec-

tively. This corresponds with an energy dissipation rate proportional to $\text{Re}^{-0.25}$ and $\text{Re}^{-0.5}$. It is important to realize that the Reynolds number of individual vortex-wall collisions Re_d , based on the translation speed of the vortices and the vortex radii, in the fully developed 2D turbulence case is an order of magnitude smaller than the integral Reynolds number of fully developed turbulent flow. The Reynolds number of the individual vortex-wall collisions is $10^1 \lesssim \text{Re}_d \lesssim 10^3$ and $10^2 \lesssim \text{Re}_d \lesssim 10^4$ for $\text{Re} = 10^4$ and $\text{Re} = 10^5$, respectively. The typical translation speed of the vortices is based on the rms velocity of the flow $U \approx 1$ and the range of vortex radii, obtained from the vorticity snapshots like in Fig. 7.1.

The ratio of the enstrophy-levels observed for different initial Reynolds numbers in the range $10^4 < \text{Re} < 10^5$, shown in Fig. 7.4b, are consistent with the scaling behaviour of the enstrophy as observed in the dipole-wall collision problem. Also the amount of energy dissipation is consistent: *e.g.* the amount of energy dissipation at $\tau = 400$ is $\delta E \approx 1.6, 1.3$ and 1.0 for $\text{Re} = 10^4, 5 \times 10^4$ and 10^5 , respectively, which scales almost proportional to $\text{Re}^{-0.25}$. This corresponds with the scaling observed in the dipole-wall problem for the moderate Reynolds numbers regime. Note that only three values of the integral Reynolds number have been considered for the practical reason that the high-Reynolds number computations are very CPU demanding, therefore a more quantitative conclusion cannot be obtained from the present data. Nevertheless, it is clearly shown that 2D turbulence bounded by no-slip sidewalls is strongly dissipative compared with 2D turbulence on a double periodic domain. It may be anticipated, from the high Reynolds number dipole-wall collision observations, that in the infinite Reynolds number limit the energy dissipation may vanish faster, proportional to $\text{Re}^{-0.5}$. To observe this scaling regime the integral Reynolds number should be one or two orders of magnitude larger such that the vortex based Reynolds number is in the order of $\text{Re}_d \approx 20000$ or higher.

Fig. 7.5 shows the angular momentum versus the dimensionless time τ . The run with an initial Reynolds number $\text{Re} = 10^4$ is consistent with the findings of Clercx *et al.* [21], who revealed a vary rapid increase of the angular momentum of the flow and a subsequent relatively slow decay during the late-time evolution. In some of the high-Reynolds number simulations considered here the angular momentum evolves in a similar way as for the $\text{Re} = 10^4$ case. In other runs it is found that the angular momentum can show more disordered behaviour (see Fig. 7.5). During the intermediate decay stage the flow can suddenly spin-down and subsequently spin-up again. In the latter case the circulation of the large-scale flow can be in either the same or in the opposite direction, similar to the observations in forced 2D turbulence simulations (with much smaller integral-scale Reynolds number) [40, 72]. In the case of a spin-down event the angular momentum retains small values only briefly before it revives again. After this regime with more or less irregular behaviour the large-scale circulation of the flow is persistent (besides a very slow overall decay on very long times).

Table 7.2 presents the ensemble averaged properties of the spin-up process for

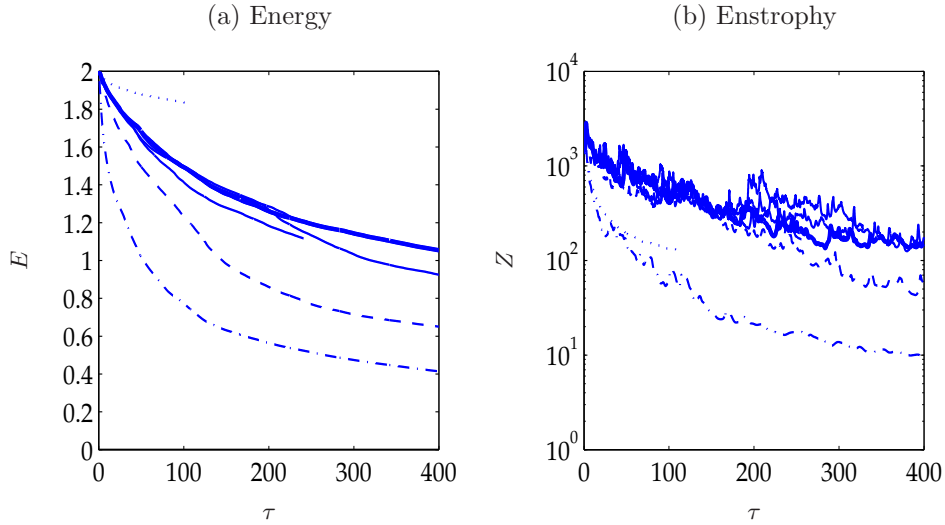


Figure 7.4 – Time evolution of the total kinetic energy (a) and enstrophy (b) versus dimensionless time τ for different initial Reynolds numbers. Decaying turbulence on a domain with no-slip boundaries with $Re = 10^5$ (solid lines), $Re = 5 \times 10^4$ (dashed line) and $Re = 10^4$ (dashed-dot line). Decaying flow on a double periodic domain with $Re = 10^5$ (dots). Thick solid line corresponds with the run shown in Fig. 7.1 and Fig. 7.2.

three different Reynolds numbers. The maximum of the angular momentum is normalized with both $L_{sb}(t=0)$ and $L_{sb}(t)$. The normalization with $L_{sb}(t)$ compensates for the fact that the energy decays significantly faster for the $Re = 10^4$ compared to the two higher Reynolds cases, see Fig. 7.4a. Table 7.2 also contains the ensemble averaged values of the spin-up time. Three different dimensionless times have been considered based on different properties of the flow. Recall that the dimensionless time τ as used in Fig. 7.4 is based on the turnover time of the initial vortices. A different dimensionless time has been applied by Chasnov [15] in a study on the Reynolds number dependence of energy and enstrophy dissipation in decaying 2D turbulence on a double periodic domain,

$$\tau^* = \int_0^{t_1} \langle \omega^2 \rangle^{1/2} dt = \frac{1}{2W} \int_0^{t_1} \|\omega\|_2 dt = \frac{1}{\sqrt{2}W} \int_0^{t_1} \sqrt{Z} dt. \quad (7.1)$$

Time τ^* can be interpreted as an appropriate measure of the actual number of turnovers of the vortices in the flow at time t_1 . It is possible to express the kinetic energy in the form of an inequality, see Eq. (7.3) in the appendix, which clearly identifies τ^* as an important time unit in the decay process. Dissipation of vorticity and the formation of high-amplitude vorticity cores in the presence of no-slip walls, see Fig. 7.3a, results in a strong reduction of the average turnover time of the vortex population.

A third non-dimensional time T_g is based on the global turn over rate of the flow,

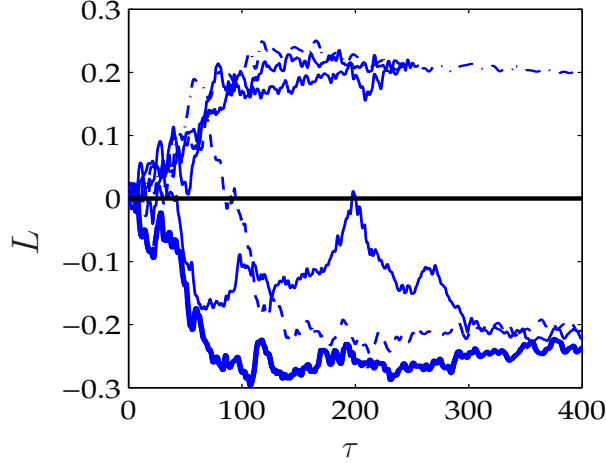


Figure 7.5 – Time evolution of the angular momentum normalized with $L_{sb}(\tau = 0)$ versus dimensionless time τ for different initial Reynolds numbers. Decaying turbulence on a domain with no-slip boundaries with $\text{Re} = 10^5$ (solid line), $\text{Re} = 5 \times 10^4$ (dashed line) and $\text{Re} = 10^4$ (dashed-dot line). Thick solid line corresponds with the run shown in Fig. 7.1 and Fig. 7.2.

which is characterized by the rms velocity and the half-width of the domain W ,

$$T_g = \frac{1}{2W^2} \int_0^{t_1} \|\mathbf{u}\|_2 dt. \quad (7.2)$$

From table 7.2 it can be deduced that high-Reynolds number flows show an equally strong spin-up compared with the moderate Reynolds number flows with $\text{Re} = 10^4$. Also the spin-up time measured in terms of the initial turnover time of the vortices τ or the global turnover time T_g does not show significant Reynolds number dependence. Note that the variation of the spin-up time between the ensemble runs is very large, see for example Fig. 7.5. The number of small-scale turnovers τ^* during the spin-up of the flow increases, on the other hand, with the Reynolds number. Note that enhanced enstrophy production (see Fig. 7.4) and subsequent formation of small-scale vortices results in a significant reduction of the overall turnover rate of the vortex population. Apparently the latter effect does not result in a faster spin-up of the flow for higher Reynolds numbers. This indicates that it is mainly the turnover of the dominant vortices and the associated formation of a large-scale flow pattern that determine the spin-up rate of the flow. Another interesting issue is that the magnitude of the torque measured by the standard deviation σ of the time-derivative of the angular momentum does not demonstrate significant dependence on the Reynolds number, as can be seen in the last column

Table 7.2 – Statistics of the spin-up variables for three different Reynolds numbers. Ensemble averaged maximum of the absolute value of the angular momentum $\langle L_{max} \rangle$ defined as the maximum for $\tau < 400$. This value is normalized with the angular momentum corresponding with solid-body rotation of the initial flow field $L_{sb}(\tau = 0)$ and based on an equivalent solid-body rotation computed with the rms velocity at the time the maximum is observed. Spin-up time measured in terms of the turnover time of the initial vortices τ , the actual turnover time of the vortices τ^* and the global turnover time T_g . Standard deviation σ of the net torque i.e. \dot{L} averaged over the period $\tau < \tau_s$ where τ_s denotes the time the maximum in the absolute value of the angular momentum is observed.

Re	$\frac{\langle L_{max} \rangle}{L_{sb}(\tau=0)}$	$\frac{\langle L_{max} \rangle}{L_{sb}(\tau)}$	τ	τ^*	T_g	σ
10^4	0.19 ± 0.05	0.35 ± 0.07	180 ± 50	600 ± 200	45 ± 20	0.10 ± 0.01
5×10^4	0.24 ± 0.05	0.36 ± 0.07	150 ± 50	1000 ± 300	50 ± 15	0.13 ± 0.02
10^5	0.23 ± 0.05	0.32 ± 0.07	150 ± 50	1300 ± 500	50 ± 15	0.10 ± 0.02

in table 7.2. This confirms the conjecture that the pressure contribution in the angular momentum balance (1.18) becomes finite in the high Reynolds number limit, whereas the contribution of the viscous stresses will vanish in the same limit. It has been verified that the pressure term is at least two orders of magnitude larger than the contribution of the viscous stresses in the range $10^4 < \text{Re} < 10^5$ and $\tau < 400$.

It is observed in the numerical study of Clercx and Bruneau [18] that the angular momentum production during an oblique dipole-wall collision does not exhibit significant Reynolds number dependence. The range of Reynolds numbers covered by the study of Clercx and Bruneau is $625 < \text{Re} < 5000$, where the Reynolds number is based on the half-width of the domain and rms velocity of the flow. This corresponds with a vortex-based Reynolds number in the range $500 < \text{Re}_d < 4000$ [18]. The vortex-based Reynolds number of the 2D turbulence simulations considered here is in the same order of magnitude. Therefore, it can be concluded that the absence of significant Reynolds number dependence on the magnitude of the torque in the present simulations is consistent with the angular momentum production of an oblique dipole-wall collision.

Concluding remarks

The high-Reynolds number simulations presented in this chapter and the previous chapter clearly reveal that spontaneous production of angular momentum is a generic feature of 2D flows in non-circular domains. Therefore, it is not a low Reynolds number artifact. The angular momentum development can be associated with the formation of a large-scale (background) flow pattern in the container. It is found that the spin-up rate of the flow does not show significant dependence on the Reynolds number. This observation can be related to a Reynolds number

independent value of the rms of the torque during the spin-up of the flow. A similar result is obtained from oblique dipole-wall collision simulations, where it is seen that the amount of angular momentum productions reaches a finite value for sufficiently high Reynolds numbers.

7.4 Appendix: a note on the characteristic time-scale

An important time-scale in decaying turbulence is the time-scale τ^* as defined in (7.1). The physical interpretation of Chasnov [15] is already given in the previous section. Here we obtain an inequality that clearly demonstrates that τ^* is closely related to the decay process.

Theorem 1. *The total kinetic energy $E(t)$ of viscous flow on a bounded domain $\Omega \subset \mathbb{R}^2$ with the smallest Stokes eigenvalue λ verifies for $t_1 \in (0, \infty)$ the following property*

$$E(t) \leq E_0 \exp \left[-2\nu \sqrt{\lambda/E_0} \int_0^{t_1} \sqrt{Z} dt \right]. \quad (7.3)$$

Proof: By using the Poincare inequality $\|\mathbf{u}\|_2^2 \leq \lambda^{-1} \|\nabla \mathbf{u}\|_2^2 = \lambda^{-1} \|\omega\|_2^2$ and time-integration of (1.10) yields,

$$E(t) \leq E_0 \exp(-2\nu\lambda t). \quad (7.4)$$

Rewriting (1.10) and applying the Poincare inequality once gives,

$$\frac{d}{dt} \frac{\|\mathbf{u}\|_2^2}{\|\mathbf{u}_0\|_2^2} = -2\nu \frac{\|\omega\|_2^2}{\|\mathbf{u}_0\|_2^2} \leq -2\nu\lambda^{1/2} \frac{\|\mathbf{u}\|_2}{\|\mathbf{u}_0\|_2} \frac{\|\omega\|_2}{\|\mathbf{u}_0\|_2}.$$

From inequality (7.4) it is realized that $\|\mathbf{u}\|/\|\mathbf{u}_0\| \leq 1$ such that it follows that

$$\frac{d}{dt} \frac{\|\mathbf{u}\|_2^2}{\|\mathbf{u}_0\|_2^2} + 2\lambda^{1/2}\nu \frac{\|\omega\|_2}{\|\mathbf{u}_0\|_2} \frac{\|\mathbf{u}\|_2^2}{\|\mathbf{u}_0\|_2^2} \leq 0.$$

Then Gronwall's inequality in the following form finishes the proof.

Lemma 1. *(Gronwall's inequality) If $\alpha(t)$ is real-valued and non-negative on $(0, \infty)$, and if the function $y(t)$ satisfies the following differential inequality:*

$$\frac{dy}{dt} + \alpha(t)y \leq 0, \quad (7.5)$$

then $y(t)$ is bounded on $(0, \infty)$ by

$$y(t) \leq y(0) \exp \left(- \int_0^{t_1} \alpha(t) dt \right). \quad (7.6)$$

Chapter 8

Forced 2D turbulence on a bounded domain

In this chapter we consider the statistical properties of forced 2D turbulence in a square domain with no-slip boundaries. In numerical studies on forced 2D turbulence in a periodic box, it is common practice to use additional friction mechanisms in order to achieve a statistically steady state, see Chapter 1. As observed in the high-resolution simulations of Boffetta [11] the presence of friction has dramatic consequences for the statistical properties of the smallest scales of motion. In the present simulations the no-slip boundary provides a natural sink for the kinetic energy that can balance the injection of energy by the external forcing such that a steady state is achieved. In this way the use of a volumetric drag force can completely be avoided. Therefore, it is challenging to determine the statistical properties of the small-scales in the interior of a domain with no-slip boundaries. Furthermore, it is anticipated that the no-slip boundaries are able to prevent energy accumulation on the largest scales of motion and the subsequent formation of a condensate. Smith and Yakhot [100,101] found that in a condensation regime the self-similarity of the small-scale statistics is lost. It is examined in this chapter whether the no-slip boundaries sufficiently prevent the accumulation of energy in domain-size coherent vortices and subsequently sustain the self-similarity at the small scales.

A difficulty that may keep the small-scale structure from obtaining KBL scaling is the injection of high-amplitude vorticity filaments from the boundaries into the bulk of the flow. Note that this process may affect the isotropy and local homogeneity of the flow. Furthermore, Clercx and van Heijst [22] provide evidence that in decaying turbulence boundary layer detachment can result in an inverse energy cascade in the wall region. Wells *et al.* [106] used a forcing mechanism by oscillating the container with a certain frequency. This process can result in the production of vorticity at the domain boundaries that detach and move subsequently into the

interior of the flow domain. The energy spectra of Wells *et al.* suggest that these vorticity layers feed both an inverse energy cascade and a direct enstrophy cascade. In the present study the container remains fixed and we apply an external forcing mechanism. An important question is, whether the detachment of boundary layer vorticity has an important effect on the enstrophy transfer rate of the internal fluid.

8.1 Setup of the simulations

The forcing is defined in terms of q in the vorticity equation (1.5). Note that this corresponds with a solenoidal forcing function \mathbf{f} in Eq. (1.1). The forcing is given by a Markov chain process

$$q(t_n, \mathbf{x}) = c_r q(t_{n-1}, \mathbf{x}) + |A_p|(1 - c_r^2)^{1/2} w(\mathbf{x}) \quad (8.1)$$

where

$$c_r = \frac{1 - \delta t / \tau_c}{1 + \delta t / \tau_c} \quad (8.2)$$

is the correlation factor with correlation time τ_c and $|A_p|$ the amplitude, which is static in time. The function $w(\mathbf{x})$ takes completely random values at each time step δt . The spatial structure of $w(\mathbf{x})$ is generated by considering the Fourier transform

$$w(\mathbf{x}) = \sum_{k_1 \leq |\mathbf{k}| \leq k_2} \exp(i\theta_{\mathbf{k}}) \exp(i\mathbf{k} \cdot \mathbf{x}). \quad (8.3)$$

The phase $\theta_{\mathbf{k}} \in [0, 2\pi]$ is drawn at each time step δt from a uniform distribution that is independent for each wave vector in the shell $k_1 < |\mathbf{k}| < k_2$. This forcing protocol, originally introduced by Lilly [63], is commonly used in numerical simulation of 2D turbulence. In the present study also the amplitude of wave vectors with $k_x = 0$ or $k_y = 0$ is set equal to zero such that the forcing does not exert a net torque on the fluid. Table 8.1 presents the parameters for the simulations.

Table 8.1 – *The parameters of the forced simulation: Number of Fourier coefficients N and active number N_{act} , time-step δt , kinematic viscosity ν , penalization parameter ϵ , forcing wavenumbers k_1 and k_2 , amplitude $|A_p|$, correlation time c_r and half-width of the square domain W .*

N	N_{act}	δt	ν	ϵ	k_1	k_2	$ A_p $	τ_c	W
2048	1364	4×10^{-5}	10^{-4}	10^{-8}	7	9	6	10^{-2}	1

8.2 Statistically steady state

In Fig. 8.1 the evolution of the total kinetic energy and enstrophy are given. It can be deduced that the flow slowly converges towards a statistically steady state. The maximum of the Reynolds number $Re(t)$ is approximately 25000. Note that in the case of periodic boundary conditions the applied forcing mechanism would result in an unbounded growth of the total kinetic energy. In section 1.2 it has

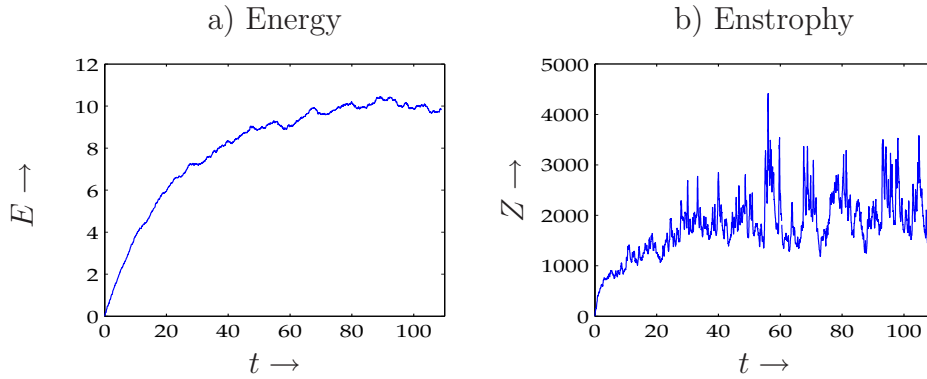


Figure 8.1 – Total kinetic energy (a) and enstrophy (b) versus time of a forced turbulence simulation. The parameters of the simulation are given in table 8.1.

been shown that a statistically steady state in the absence of bottom friction implies that the energy input by the forcing is balanced by viscous dissipation $\langle (\mathbf{f}, \mathbf{u}) \rangle = 2\nu \langle Z \rangle$. The production of vorticity at the domain boundaries results in a sufficiently high dissipation rate of kinetic energy that is able to balance the energy injection of the external forcing. The peaks in enstrophy in Fig. 8.1b are mainly a result of intensive flow-wall interactions. It is verified that the terms T_1 and T_2 in the enstrophy balance (1.12) are two orders of magnitude larger than the term T_3 which quantifies the vorticity injection of the external forcing. This means that the steady state in the total kinetic energy is indeed achieved by production of vorticity at the domain boundaries. Fig. 8.2 shows the angular momentum of the flow versus time. It can be seen that the flow acquires net angular momentum that strongly fluctuates in time. The external forcing is constructed such that it does not exert a net torque on the fluid. Therefore, the production of angular momentum is a spontaneous result of flow-wall interaction.

In Fig. 8.3 snapshots of the vorticity field and the corresponding stream function are given for two different times. Several vortices can be recognized with different sizes and strengths. The larger vortices are a result of the forcing whereas the smallest vortices are a result of the high-amplitude vorticity filaments from the boundaries that roll up into new small-scale vortices. In the present simulations the large-scale flow patterns can be associated with the strongest vortices in Fig. 8.3.

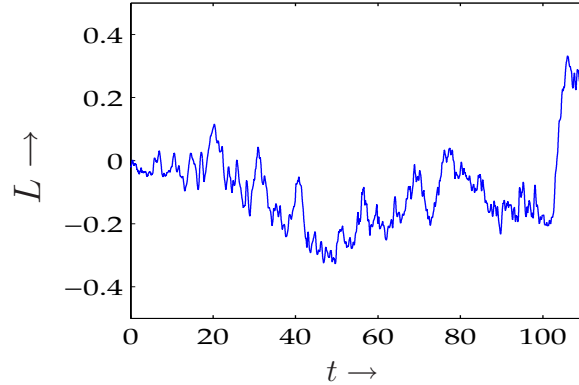


Figure 8.2 – Angular momentum L normalized with $L_{sb}(t = 0)$ with respect to time of a forced turbulence simulation. The external forcing does not exert torque on the flow. More details of the simulation can be found in in table 8.1.

Since the angular momentum can be written as $L = 2 \int \psi dA$, it is obvious that the angular momentum changes sign between $t = 90$ and $t = 110$. The energy does not pile up in the dominant vortices due a strong dissipation of energy during the interaction with the no-slip sidewalls. The formation of a condensate as observed in the simulations of Smith and Yakhot [100,101] is absent. In their simulations of forced 2D turbulence on a periodic domain without bottom friction almost all the vorticity is eventually contained in a single dipolar vortex. The no-slip boundary clearly prevents the accumulation of energy in domain-sized coherent structures and hence the formation of a condensate.

In Molenaar *et al.* [72] it was found, for forced 2D flow on square domain with no-slip boundaries, that a different forcing protocol results in a continuous cycle of condensate formation and subsequent disruption of the large-scale organization of the flow. The disruption of the internal flow is a result of the detachment of vorticity layers from the domain boundaries. It was found that during the spin-up cycle the total kinetic energy and the normalized angular momentum are strongly correlated in time. Although, there is a sign-reversal of the normalized angular momentum at the end of the present simulation around $t = 110$ this is not reflected in the total kinetic energy. Similar behaviour is observed in the high Reynolds number decaying turbulence simulations considered in Chapter 7, compare for instance Fig. 7.5 and Fig. 7.4. The absence of significant correlation between the normalized angular momentum and the total kinetic energy in the flow considered here can be related to several difference in the setup of the present simulation and the simulations considered by Molenaar *et al.* [72]: *i*) the forcing is completely isolated to a wavenumber band in Fourier transform space *i.e.* there is no excitation of the

flow at large scales, *ii*) the external forcing does not exert any torque and, *iii*) the Reynolds number is an order of magnitude larger.

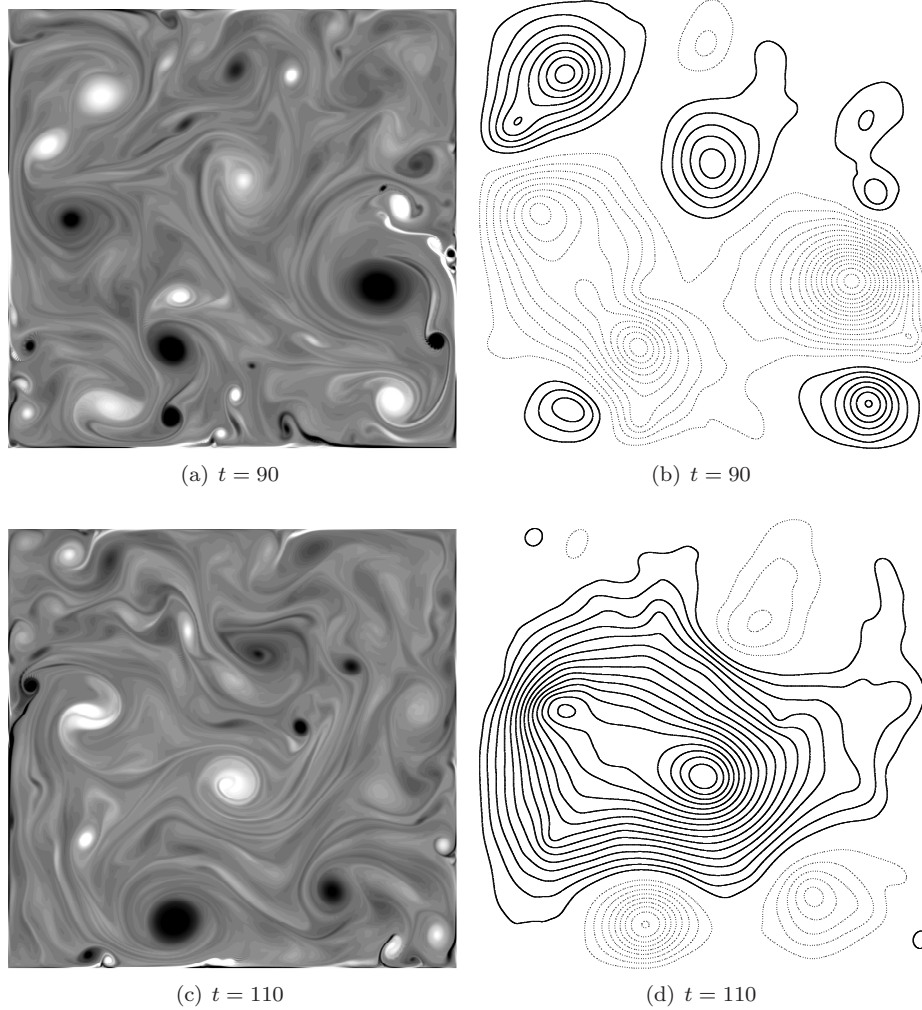


Figure 8.3 – Two snapshots of the vorticity distribution and the stream function of a forced turbulence simulation. The vorticity ranges from $\omega = -120$ to $\omega = +120$ with 30 grey levels. The stream function is shown with an interval of 0.1. The solid isolines correspond with positive values of ψ and the dashed isolines represent negative values of ψ .

8.3 Structure functions and self-similarity

The spatial structure of the flow can be analyzed by considering velocity increments over a separation vector \mathbf{r} ,

$$\delta u_i(\mathbf{x}, \mathbf{r}) = u_i(\mathbf{x} + \mathbf{r}) - u_i(\mathbf{x}). \quad (8.4)$$

Note that one can consider both longitudinal and transverse velocity components along the separation vector \mathbf{r} . If it is assumed that the flow is locally homogeneous, isotropic and exhibiting self-similarity, the velocity increments scale like a power law

$$\delta u_i(r) \sim r^h \quad (8.5)$$

with h a constant exponent and $r = |\mathbf{r}|$. The ensemble averages over the velocity increments of the form

$$S_p(\mathbf{x}, \mathbf{r}) = \langle (\delta u_i)^p \rangle \quad (8.6)$$

are called structure functions of order p . In the case of self-similarity the structure functions in a locally homogeneous isotropic flow scale according to

$$S_p(r) \sim r^{\zeta_p} \quad (8.7)$$

with $\zeta_p = hp$ the scaling exponent. For small separations in 2D Euler flow it can be shown analytically that $\zeta_p = p$ or $h = 1$ [8]. This result can also be obtained on the same dimensional grounds as discussed in section 1.2 for the derivation of the shape of energy spectrum in the enstrophy cascade range. Thus assuming that the scaling of the structure functions is determined by an enstrophy transfer rate χ and the separation length r . Note that the vorticity increments that scale on dimensional grounds like $\delta\omega \sim \delta u_i/r \sim r^h/r$, become independent of r in the enstrophy inertial range, since $h = 1$.

For the inverse energy cascade range dimensional reasoning based on a constant energy transfer rate yields that $\zeta_p = p/3$ or $h = 1/3$. Deviation from the self-similar scaling of the structure functions (8.7) in the inertial ranges is known as intermittency.

8.4 Second-order moments

If one assumes that the flow is both locally homogeneous and isotropic it is possible to express the transverse second-order structure function $S_2^\perp(r)$ in terms of the longitudinal second-order structure function $S_2^\parallel(r)$,

$$S_2^\perp(r) = \left(1 + \frac{r}{2} \frac{d}{dr}\right) S_2^\parallel(r) \quad (8.8)$$

where $r = |\mathbf{r}|$, see *e.g.* Pope [88]. By using Eq. (8.8) it is possible to verify whether the small-scale statistics is consistent with the crucial KBL assumption that the flow is locally homogeneous and isotropic. The procedure is straightforward: first one computes both structure functions and then one computes an estimate for $S_2^\perp(r)$ by using $S_2^\parallel(r)$ and relationship (8.8). Strong deviations between the estimate for $S_2^\perp(r)$ and the direct determination of $S_2^\perp(r)$ indicate the presence of anisotropy or local inhomogeneity in the flow.

Fig. 8.4 shows the second-order structure functions for both the velocity and vorticity. The structure functions are computed in a square box in the centre of the domain. Various box sizes with a half-width ranging from 0.3 to 0.6 have been considered, as well. No significant differences have been observed for the statistical quantities in the present study. Fig. 8.4 also shows a comparison of the transverse second-order structure function, the computed estimate obtained with Eq. (8.8), and the longitudinal second-order structure function. The result is in good agreement for the scales smaller than the forcing scale, which supports the assumption that the flow can be considered as statistically isotropic and locally homogeneous. The structure function $S_2^\perp(r)$ is proportional with r^2 for the smallest separations and flattens when moving to the forcing length scale.

It can be shown that the scaling exponent ζ_p of the structure functions is bounded by the corresponding order

$$\zeta_p \leq p, \quad (8.9)$$

see *e.g.* [88] and [97]. Therefore the comparison with the power-law exponent of the energy spectrum has some limitations. Table 8.2 provides an overview of the relationship between the energy spectrum and the structure function. Since the slope of the second-order velocity structure function, shown in Fig. 8.4a is close to the upper bound (8.9) a straightforward interpretation of the velocity structure function is not possible.

It is observed in Fig. 8.4b that the second order structure function of the vorticity is proportional with $r^{1.5}$ for the smallest scales and flattens for separations near the forcing scale l_f . It provides more information about the scaling exponents of the energy spectrum, since the slope of the second-order structure function of the vorticity is well separated from the upper bound (8.9). It can then be deduced from Fig. 8.4b and table (8.2) that the corresponding energy spectrum has a slope of k^{-3} near the forcing and becomes steeper for higher wavenumber, $k^{-4.5}$,

which is significantly steeper than the inertial range prediction in the enstrophy cascade range by KBL. A possible explanation is the presence of a non negligible amount of viscous dissipation. This can be examined by computing the dissipation scale $l_d = (\nu^3/\chi_{loc})^{1/6}$, where the local enstrophy dissipation rate is defined as $\chi_{loc} = -\nu A^{-1} \int_{\mathcal{B}} |\nabla\omega|^2 dA$ and \mathcal{B} denotes the measurement section in the interior of the domain. The ensemble averaged value for l_d is approximately 5×10^{-3} , which is consistent with the position of the steep section of the vorticity structure function in Fig. 8.4b. From these numbers it can be deduced that the enstrophy cascade extends over less than two decades between the forcing scale and the dissipation scale. Therefore, the role of viscous dissipation in the range between l_d and l_f cannot be excluded. This may explain the behaviour of the second-order structure function of the vorticity in Fig. 8.4b. On the other hand, in several studies it is anticipated that energy spectra steeper than k^{-3} or second-order vorticity structure functions steeper than r^0 result from the presence coherent structures in the flow see *e.g.* Benzi *et al.* [8]. The high-resolution simulation of Kevlahan and Farge [50] of isolated vortex-merger events, in which many intensive spiraling vorticity filaments are created, also show typically steeper energy spectra. Fig. 8.3 clearly reveals the presence of coherent vortices and spiraling filamentary structures in the vorticity field. Therefore, the observed deviation from the KBL-theory not necessarily has be explained by viscous dissipation in the enstrophy cascade range in the present simulation, it might reflect the dominant role of coherent structures on the small-scale statistics.

Table 8.2 – Relationship between the scaling of energy spectrum of the form $E(k) \propto k^{-\alpha}$ and the second-order structure function $S_2(r) \propto r^p$. If $0 < \alpha < 3$ then $\alpha = 1 + p$ and if $\alpha > 3$ then $p = 2$.

α	1	5/3	2	2.5	3	5
p	0	2/3	1	1.5	2	2

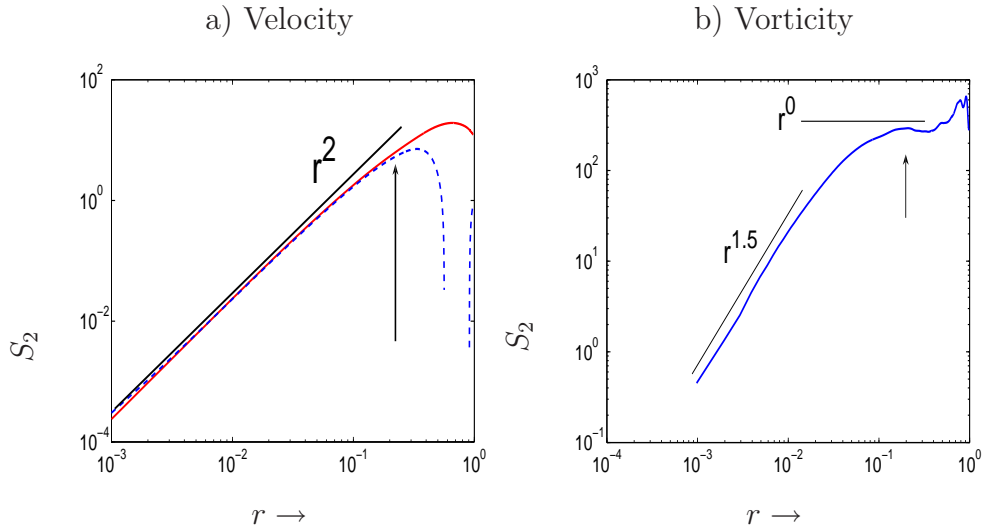


Figure 8.4 – Transverse second-order structure function of the velocity and the vorticity. The arrow denotes the position of the length-scale of the forcing. The dashed line in panel (a) corresponds with the isotropic estimate for the transverse second-order structure function based on the longitudinal structure function. The structure functions are computed in a square box with a half-width 0.5 in the centre of the flow domain.

8.5 Intermittency and extended self-similarity

The self-similar scaling of the form (8.7) is motivated by the scale invariance of the Euler equations. It is assumed that viscous flow in the limit of $\nu \rightarrow 0$ will obtain self-similar scaling. In the previous section it is found that the forcing scale and the dissipation scale are only weakly separated. Therefore, the presence of viscous dissipation can be expected to be relevant for all separations smaller than the forcing scale. Since the Stokes equation is not scale invariant it can be expected that self-similarity will no longer hold.

A straightforward method to analyze scale dependence is based on the probability density function (pdf) of the vorticity increments at different separations. Note that the second-order structure function at a given separation length is essentially the second-order moment of the probability density function of the corresponding increments.

Fig. 8.5 presents the pdf of the vorticity increments for seven separations in the range $r < l_f$. It is observed that the pdf has a similar shape for all separations. A Gaussian core can be recognized with exponential tails. The similarity in the shape of the pdf suggests scale invariant statistics. Note that the pdfs have been normalized with the second-order moment, which is essentially the second-order structure function that is shown in Fig. 8.4b. The convergence of the pdf on the

tails of the distribution is, however, too poor to draw any firm conclusions about the scale invariance.

A more accurate method for the detection of intermittency effects is proposed by Benzi *et al.* [7]. These authors showed that locally homogeneous, isotropic turbulence obeys a more general scaling relation of the form

$$S_p(r) \sim S_3^{\tilde{\zeta}_p}. \quad (8.10)$$

The scaling (8.10) extends the inertial range property (8.7) which is strictly valid for $r_d < r < l_f$ deep into the dissipation range. The relative scaling exponent $\tilde{\zeta}_p$ allows a more accurate determination and hence a more reliable detection of the presence of either extended self-similarity or intermittency. The relative scaling

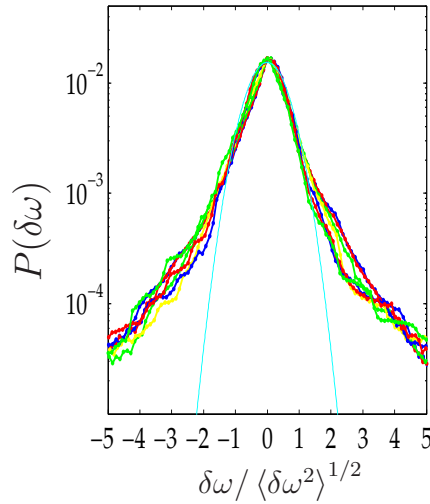


Figure 8.5 – Probability density function of the vorticity increments for separations $r < l_f$. A Gaussian distribution is given for comparison.

exponent can now be expressed as $\tilde{\zeta}_p = p/3 + \gamma_p$, where γ_p is a measure of the degree of intermittency. Babiano *et al.* [4] determined the relative scaling exponent $\tilde{\zeta}_p$ for both the inverse energy cascade and direct enstrophy cascade range. It was observed that in the enstrophy cascade range the intermittency correction γ_p was negligible, so that $\tilde{\zeta}_p = p/3$. In the inverse energy cascade range strong intermittency correction was found to be necessary. The magnitude of the intermittency correction in the inverse energy cascade is close to the corresponding value of the intermittency correction observed in 3D turbulence. Babiano *et al.* [4] developed an intermittency model for γ_p based on the scaling behaviour of local averages of the non-linear transfer rate of the enstrophy. It correctly explains the observed absence of intermittency in the enstrophy cascade range and the presence of strong

intermittency in the inverse energy cascade range.

Fig. 8.6a shows the structure functions with respect to the separation length r and in Fig. 8.6b the structure functions are plotted versus the third-order structure function. It can be seen that the extended self-similarity holds up to order $p = 8$. For $p = 10$ strong deviations can be observed. This may be explained by the lack of convergence for such high-order structure functions. In Belin *et al.* [6] some estimates can be found for the number of data points that are required to compute the structure functions within sufficient accuracy. According to these estimates it is possible to determine the structure functions up to order six for the present data. For the higher-order structure functions it is anticipated that the convergence is too poor to draw firm conclusions.

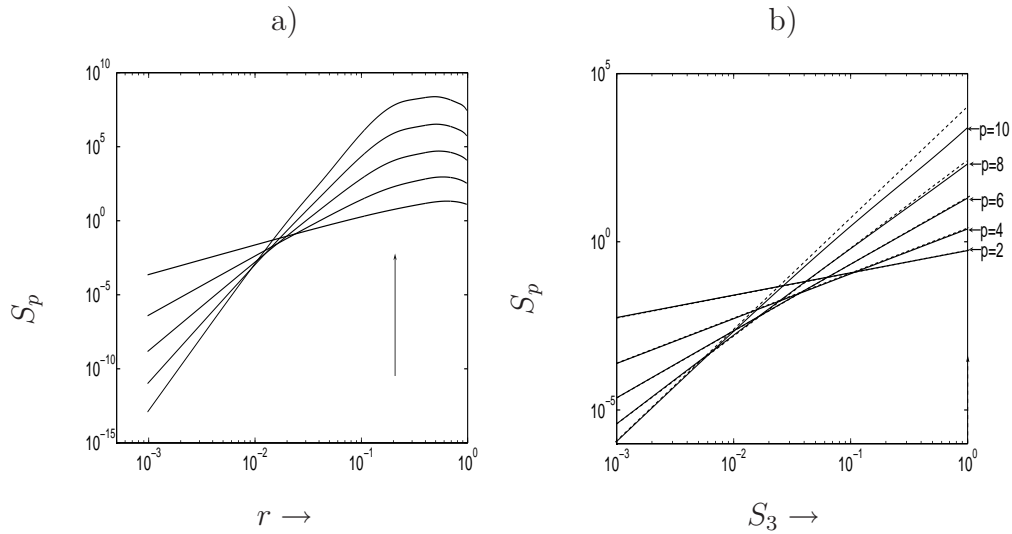


Figure 8.6 – Transverse structure functions S_p of the velocity versus the separation r (a) and versus the third-order structure function of the absolute value of the transverse velocity increments. The arrow denotes the forcing scale. Dashed lines in panel (b) correspond with a slope of $p/3$.

8.6 Enstrophy transfer

Bernard [9] derived an analytical expression for a mixed velocity-vorticity structure function in the limit of $\nu \rightarrow 0$,

$$\frac{\langle (\delta u_{||})(\delta \omega)^2 \rangle}{r} = -2\chi \quad (8.11)$$

with χ denoting the ensemble averaged enstrophy dissipation rate. It can be seen as the equivalent of the well-known 4/5 law of 3D turbulence. The mixed third-order structure function in (8.11) can be interpreted as a measure of the non-linear transfer rate of enstrophy. The role of the longitudinal velocity increments can be related to the alignment between the rate of strain tensor and the vorticity gradient vector observed in Eq. (1.16), which describes the non-linear amplification of the vorticity gradients.

In the derivation of relation (8.11) it is assumed that the flow is locally homogeneous and isotropic. In Fig. 8.4a it has been verified that these conditions can be assumed in the interior of the flow domain. Therefore, relation (8.11) can safely be applied to obtain an estimate for the enstrophy transfer rate. In Fig. 8.7 the mixed third-order structure function is shown with respect to the separation length and with respect to the third-order structure function of the vorticity. In the forcing range a sign-change of the mixed third-order structure function can be observed in Fig. 8.7a. This can be related to the injection of vorticity by the external forcing. No other sign changes are observed in Fig. 8.7a, which indicates that a direct enstrophy cascade is developed from the forcing range to the dissipation ranges. The effect of vorticity injection from the domain boundaries is not recognized in the form of a secondary forcing scale. The mixed third-order structure function does not clearly show the inviscid scaling (8.11) proportional with r^1 . Since the dissipation scales l_d and l_f are not well separated, so that viscous dissipation may affect the scaling. To overcome the dissipation effect the mixed third-order structure function is plotted versus the third-order structure function of the vorticity in Fig. 8.7b. In the KBL framework for the enstrophy inertial range the vorticity structure functions are independent of the separation length. It can be deduced from Fig. 8.7b that the enstrophy flux demonstrates scaling that is consistent with (8.11) in the limit of $\nu \rightarrow 0$. This signifies that the scaling for separations $r < l_f$ is consistent with the KBL picture of the direct cascade of enstrophy towards the smallest scale of motion. There is no sign that the vorticity injection from the sidewalls acts as a separate forcing length-scale for the internal flow.

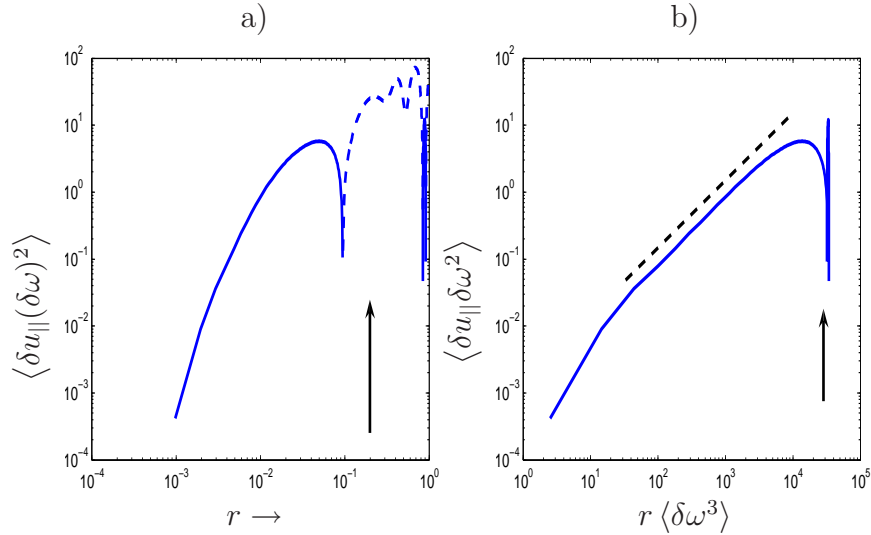


Figure 8.7 – Mixed third-order structure function versus separations r (a) and versus third order structure function computed with the absolute value of the vorticity increments (b). The dashed line in panel (b) corresponds with a slope of +1.

Concluding remarks

A statistically steady state is achieved in forced 2D flow in a square box with no-slip sidewalls. High-amplitude vorticity filaments are injected into the flow domain, which could possibly affect the homogeneity and isotropy of the flow. It is observed, however that in the interior of the flow domain the flow recovers local homogeneity and isotropy at small-scales. The extended self-similarity of the flow at small-scales is maintained. This can be related to the absence of the formation of a condensate due to interaction with the no-slip walls. A similar observation is reported by Kramer [53] for flows in a channel with a periodic and a non-periodic direction with no-slip walls. In the present flow simulations it is observed that a direct enstrophy cascade range develops in the interior of the domain. This is an interesting observation since usually the direct cascade of enstrophy is studied in the presence of bottom friction, which is completely absent in the present simulations. The second-order structure function of the vorticity shows significant deviation from the KBL theory. This might be explained by the presence of coherent structures and spiralling vortex filaments in the internal flow. On the other hand, the separation between the forcing length-scale and the dissipation length scale is too limited to draw a firm conclusion.

Chapter 9

Conclusions and prospects

It is found that the Fourier spectral approach with volume-penalization is very useful for pursuing direct numerical simulation (DNS) of high Reynolds number 2D flows in complex geometries. Normal and oblique dipole wall collisions served as challenging benchmark problems to analyze the convergence properties of the scheme.

The DNS computations in a circular geometry at moderate Reynolds number show similar behaviour as the numerical simulations of Li and Montgomery [60] and the experiments of Maassen *et al.* [65] in stratified flows. It is found that significant production of angular momentum is absent on the circle. Therefore, the angular momentum of the initial condition has important consequences for the late-time evolution of the flow. Based on a minimum enstrophy principle a diagram is constructed that systematically explains the development of very typical flow patterns. In an elliptic geometry it is observed that the magnitude of the torque can be scaled with the eccentricity of the ellipse. The circle and the square can be seen as the two limiting cases. It is indeed observed that in an elliptic geometry in the limit of vanishing eccentricity the magnitude of the torque becomes minimal. This can be explained by the scaling behaviour of the pressure contribution in the angular momentum balance with respect to the eccentricity. For sufficiently high values of the eccentricity the spin-up process can be compared with the square case *i.e.* all runs in an ensemble show strong spin-up of the flow, which is associated with the formation of monopolar (strongly asymmetric dipole) or tripolar vortices. In the intermediate range of eccentricities it is remarkably observed that a slight displacement of the initial vortices results in either a quadrupolar end-state like in the circular case or in a strong spin-up of the flow like in the square case. This implies a striking dependence of the end-state on the details of the initial condition.

High-Reynolds number simulations on a square domain reveal that spontaneous production of angular momentum is not a low-Reynolds number artifact. The magnitude of the torque, the spin-up strength and spin-up time do not show significant dependence on the Reynolds number for $10^4 < \text{Re} < 10^5$. This observation is con-

sistent with the observation of angular momentum production during an oblique dipole-wall collision. It can also be related to the role of the pressure contribution in the angular momentum balance, which becomes finite in the limit of vanishing viscosity. The characteristic spin-up time of the flow is related to the turnover of the dominant vortices formed in the first decay stage and the associated formation of the large-scale circulation cell. It is also shown that the energy dissipation rate is relatively high compared with decaying 2D turbulence on a periodic domain. This can be related with the production of high-amplitude vorticity at the no-slip walls. The scaling relations of the enstrophy production and the energy dissipation rate obtained from isolated dipole-wall collisions can explain the rapid energy decay of fully developed 2D flow at high Reynolds numbers.

Additional simulations are conducted where the flow is maintained by an exter-

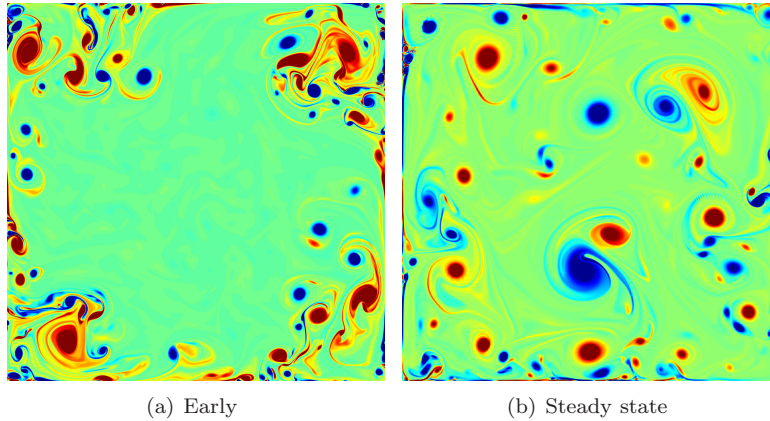


Figure 9.1 – Two snapshots of the vorticity field in an oscillating spin-up. The time-averaged Reynolds number is approximately 40000. The simulation is performed with 1364^2 active Fourier modes, time-step $\delta t = 2 \times 10^{-4}$ and penalization parameters $\epsilon = 10^{-8}$.

nal stochastic forcing mechanism. It is observed that a statistically steady state develops due to flow-wall interaction and energy injection in the bulk of the flow. The use of volumetric drag forces can be avoided completely. Therefore, 2D turbulence on domain bounded with no-slip sidewalls is an interesting test case of the classical KBL-theory. It is found that a direct cascade of enstrophy is indeed present in the interior of the flow domain. Furthermore, it is found that extended self-similarity (ESS) holds in the bulk of the flow. In the condensate regime on a double periodic domain strong departures from (ESS) at small-scales have been reported, see Smith and Yakhot [101]. In a confined geometry with no-slip walls energy accumulation at the large scales is prevented. This might explain why ESS is not violated at the small scales of the flow.

An interesting prospect is the use of oscillating spin-up to maintain the flow, see

Wells *et al.* [106]. In their experiments and simulations an extra oscillation is added to the background rotation of a square container. This results in the formation of boundary layers that subsequently detach from the sidewalls. In Fig. 9.1 an example of oscillating spin-up is given. The data of Wells *et al.* [106] indicates that the vorticity layers that detach from the wall result in the formation of a dual cascade. In future investigation it would be interesting to perform these simulation at higher Reynolds numbers. Furthermore, it is important actually to measure the spectral fluxes in both the near-wall region and the bulk of the flow.

Bibliography

- [1] Angot P., Bruneau C.H. & Fabrie P. A penalization method to take into account obstacles in viscous flow. *Numer. Math.* **81** (1999) 497.
- [2] Arfken G.B. & Weber H.J. *Mathematical Methods for Physicists*. Elsevier, Academic Press (2005).
- [3] Arquis E. & Caltagirone J.P. Sur les conditions hydrodynamique au voisinage d'une interface milieu fluide-milieu poreux: application à la convection naturelle. *C. R. Acad. Sci. Paris* **299** (1984) 1.
- [4] Babiano A., Dubrulle B. & Frick P. Scaling properties of numerical two-dimensional turbulence. *Phys. Rev. E* **52** (1995) 3719.
- [5] Batchelor G.K. Computation of the energy spectrum in two-dimensional turbulence. *Phys. Fluids. Suppl* **12** (1969) 233.
- [6] Belin F., Tabeling P. & Willaime H. Exponents of structure functions in a low temperature helium experiment. *Physica D.* **93** (1996) 52.
- [7] Benzi R., Ciliberto S., Tripicciono R., Baudet C., Massaioli F. & Succi S. Extended self-similarity in turbulent flows. *Phys. Rev. E* **48** (1993) R29.
- [8] Benzi R., Paladin G. & Vulpiani A. Power spectra in two-dimensional turbulence. *Phys. Review A.* **42** (1990) 3654.
- [9] Bernard D. Three-point velocity correlation functions in two-dimensional forced turbulence. *Phys. Rev. E.* **60** (1999) 6184.
- [10] Beta C., Schneider K. & Farge M. Wavelet filtering to study mixing in 2D isotropic turbulence. *Commun. Nonlinear Sci. Numer. Simulat.* **8** (2003) 537.
- [11] Boffetta G. Energy and enstrophy fluxes in the double cascade of 2D turbulence. *J. Fluid. Mech* **589** (2007) 253.
- [12] Bruneau C.H. & Kellay H. Experiments and direct numerical simulations of two-dimensional turbulence. *Phys. Rev. E* **71** (2005) 046305.

- [13] Canuto C., Hussaini M.Y., Quarteroni A. & Zang T.A. *Spectral Methods in Fluid Dynamics*. Springer-Verlag, Berlin (1987).
- [14] Carbou G. & Fabrie P. Boundary layer for a penalization method for viscous incompressible flow. *Adv. Differ. Equat.* **8** (2003) 1453.
- [15] Chasnov J.R. On the decay of two-dimensional homogeneous turbulence. *Phys. Fluids* **9** (1997) 171.
- [16] Chavanis P.H. & Sommeria J. Classification of self-organized vortices in two-dimensional turbulence: the case of a bounded domain. *J. Fluid Mech.* **314** (1996) 267.
- [17] Clercx H.J.H. A spectral solver for the Navier-Stokes equations in the velocity-vorticity formulation for flows with two non-periodic directions. *J. Comput. Phys.* **137** (1997) 186.
- [18] Clercx H.J.H. & Bruneau C.H. The normal and oblique collision of a dipole with a no-slip boundary. *Comp. Fluids* **35** (2006) 245.
- [19] Clercx H.J.H., Maassen S.R. & van Heijst G.J.F. Spontaneous spin-up during the decay of 2D turbulence in a square container with rigid boundaries. *Phys. Rev. Lett.* **80** (1998) 5129.
- [20] Clercx H.J.H., Maassen S.R. & van Heijst G.J.F. Decaying two-dimensional turbulence in square containers with no-slip or stress-free boundaries. *Phys. Fluids* **11** (1999) 611.
- [21] Clercx H.J.H., Nielsen A.H., Torres D.J. & Coutsias E.A. Two-dimensional turbulence in square and circular domains with no-slip walls. *Eur. J. Mech. B/Fluids* **20** (2001) 557.
- [22] Clercx H.J.H. & van Heijst G.J.F. Energy spectra for decaying 2D turbulence in a bounded domain. *Phys. Rev. Lett.* **85** (2000) 306.
- [23] Clercx H.J.H. & van Heijst G.J.F. Dissipation of kinetic energy in two-dimensional bounded flows. *Phys. Rev. E.* **65** (2002) 066305.
- [24] Cottet G.H. & Koumoutsakos P. *Vortex Methods: Theory and Practice*. Cambridge University Press (2000).
- [25] Cottet G.H., Koumoutsakos P. & Ould-Salihi M.L. Spatially varying cores for viscous vortex methods. *J. Comput. Phys.* **162** (2000) 164.
- [26] Daube O. Resolution of the 2D Navier-Stokes equations in velocity-vorticity form by means of an influence matrix technique. *J. Comput. Phys.* **103** (1992) 402.

- [27] Domingues M., Roussel O. & Schneider K. On space-time adaptive schemes for the numerical solution of partial differential equations. *ESIAM Proc.* **16** (2007) 182.
- [28] Don W.S. Numerical study of pseudospectral methods in shock wave applications. *J. Comput. Phys.* **1110** (1994) 103.
- [29] Falco P., Griffa A., Poulain P.M. & Zambianchi E. Transport properties in the Adriatic Sea as deduced from drifter data. *J. Phys. Ocean.* **30** (2000) 2055.
- [30] Farge M. & Schneider K. Coherent vortex simulation (CVS), a semi-deterministic turbulence model using wavelets. *Flow, Turbul. Combust.* **66** (2001) 393.
- [31] Farge M., Schneider K. & Kevlahan N.K.R. Non-Gaussianity and coherent vortex simulation for two-dimensional turbulence using an adaptive orthogonal wavelet basis. *Phys. Fluids* **11** (1999) 2187.
- [32] Fröhlich J. & Schneider K. An adaptive wavelet–vaguelette algorithm for the solution of PDEs. *J. Comput. Phys.* **130** (1997) 174.
- [33] Galdi G.P. An introduction to the Navier-Stokes initial-boundary value problem. In *Fundamental Directions in Mathematical Fluid Mechanics*, Advances in Mathematical Fluid Mechanics. Birkhäuser Verlag, Berlin (2000).
- [34] Goni G.J., Carzoli A.L., Roubicek A.J., Olson D.B. & Brown O. Algalhas ring dynamics from TOPEX/POSEIDON satellite altimeter data. *J. Marin. Resear.* **55** (1997) 861.
- [35] Gottlieb D. & Gottlieb S. Spectral methods for discontinuous problems. In D. Griffiths & G. Watson, eds., *Proc. 20th Biennial Conference on Numerical Analysis*, page 65. University of Dundee (2003).
- [36] Gottlieb D. & Shu C. General theory for the resolution of the Gibbs phenomenon. vol. 39. Accademia Nazionale Dei Lincey, ATTI Dei Convegna Lincey 147 (1998).
- [37] Gottlieb D., Shu C.W., Solomonoff A. & Vandeven H. On the Gibbs phenomenon I: recovering exponential accuracy from the Fourier partial sum of a nonperiodic analytic function. *J. Comput. Appl. Math.* **43** (1992) 81.
- [38] Gottlieb D. & Tadmor E. Recovering pointwise values of discontinuous data within spectral accuracy. In S. Abarbanel, ed., *Proc. Progress and Supercomputing in Computational Fluid Dynamics*, vol. 6, page 357. Birkhäuser, Boston (1985).

- [39] Hairer E., Nørsett S.P. & Wanner G. *Solving Ordinary Differential Equations II.* in *Stiff and Differential-Algebraic Problems*, 2nd ed. Springer-Verlag, Berlin (1996).
- [40] van Heijst G.J.F., Clercx H.J.H. & Molenaar D. The effects of solid boundaries on confined two-dimensional turbulence. *J. Fluid Mech.* **554** (2006) 411.
- [41] Hopfinger E.J. & van Heijst G.J.F. Vortices in rotating fluids. *Ann. Rev. Fluid Mech.* **25** (1993) 241.
- [42] Humi M. The case for 2D-turbulence in Antarctic data. *Nuovo Cimento Soc. Ital. fis. C. Geophys. Space Phys.* **26** (2003) 159.
- [43] Joyce G. & Montgomery D. Negative temperature states for the two-dimensional guiding centre plasma. *J. Plasma. Phys.* **10** (1973) 107.
- [44] Jung J.H. & Shizgal B.D. Generalization of the inverse polynomial reconstruction method in the resolution of the Gibbs phenomenon. *J. Comput. Appl. Math.* **172** (2004) 131.
- [45] Keetels G.H., Clercx H.J.H. & van Heijst G.J.F. A Fourier spectral solver for confined Navier-Stokes flow. *Int. J. Mult. Comp. Eng.* **6** 53.
- [46] Keetels G.H., Clercx H.J.H. & van Heijst G.J.F. Fourier spectral solver for wall-bounded flow using volume-penalization. In *Simulation of Multiphysics Multiscale Systems, 4th International Workshop, Beijing* (2007).
- [47] Keetels G.H., Clercx H.J.H. & van Heijst G.J.F. Spontaneous angular momentum generation of 2D flows in an elliptic geometry (2008). Submitted to *Phys. Rev. E*.
- [48] Keetels G.H., D'Ortona U., Kramer W., Clercx H.J.H., Schneider K. & van Heijst G.J.F. Fourier spectral and wavelet solvers for the incompressible Navier-Stokes equations with volume penalization: convergence of a dipole-wall collision. *J. Comp. Phys.* **227** (2007) 919.
- [49] Kellay H. & Goldburg W.I. Two-dimensional turbulence: a review of some recent experiments. *Rep. Prog. Phys.* **65** (2002) 845.
- [50] Kevlahan N.K.R. & Farge M. Vorticity filaments in two-dimensional turbulence: creation, stability and effect. *J. Fluid. Mech.* **346** (1997) 49.
- [51] Kevlahan N.K.R. & Ghidaglia J.M. Computation of turbulent flow past an array of cylinders using a spectral method with Brinkman penalization. *Eur. J. Mech. B/Fluids* **20** (2001) 333.
- [52] Kraichnan R.H. Inertial ranges in two-dimensional turbulence. *Phys. Fluids* **10** (1967) 1417.

- [53] Kramer W. *Dispersion of Tracers in Two-Dimensional Bounded Turbulence*. Ph.D. thesis, Eindhoven University of Technology, Eindhoven (2007).
- [54] Kramer W., Clercx H.J.H. & van Heijst G.J.F. Vorticity dynamics of a dipole colliding with a no-slip wall. *Phys. Fluids* **19** (2007) 126603.
- [55] Kravchenko A.G., Moin P. & Moser R. Zonal embedded grids for numerical simulation of wall-bounded turbulent flows. *J. Comput. Phys.* **127** (1996) 412.
- [56] Kress W. & Lötstedt P. Time step restrictions using semi-explicit methods for the incompressible Navier-Stokes equations. *Comput. Method. Appl. M.* **195** (2006) 4433.
- [57] Lax P.D. Accuracy and resolution in the computation of solutions of linear and nonlinear equations. In *Proc. Recent Advances in Numerical Analysis*, page 107. Mathematical Research Center, University of Wisconsin, Academic Press (1978).
- [58] Leith C.E. Diffusion approximation for two-dimensional turbulence. *Phys. Fluids* **11** (1968) 671.
- [59] Leith C.E. Minimum enstrophy vortices. *Phys. Fluids* **27** (1984) 1388.
- [60] Li S. & Montgomery D. Decaying two-dimensional turbulence with rigid walls. *Phys. Lett. A* **218** (1996) 281.
- [61] Li S., Montgomery D. & Jones W. Inverse cascades of angular momentum. *J. Plasma. Phys.* **56** (1996) 615.
- [62] Li S., Montgomery D. & Jones W. Two-dimensional turbulence with rigid circular walls. *Theor. Comput. Fluid Dyn.* **9** (1997) 167.
- [63] Lilly D. Numerical simulation of two-dimensional turbulence. *Phys. Fluids Suppl. II* **12** (1969) 233.
- [64] Lindborg E. Can the atmospheric energy spectrum be explained by two-dimensional turbulence? *J. Fluid. Mech.* **388** (1998) 259.
- [65] Maassen S.R., Clercx H.J.H. & van Heijst G.J.F. Decaying quasi-2D turbulence in a stratified fluid with circular boundaries. *Europhys. Lett.* **46** (1999) 339.
- [66] Maassen S.R., Clercx H.J.H. & van Heijst G.J.F. Self-organization of quasi-two-dimensional turbulence in stratified fluids in square and circular containers. *Phys. Fluids* **14** (2002) 2150.

- [67] Maassen S.R., Clercx H.J.H. & van Heijst G.J.F. Self-organization of decaying quasi-two-dimensional turbulence in stratified fluid in rectangular containers. *J. Fluid Mech.* **495** (2003) 19.
- [68] Madja A., McDonough J. & Osher S. The Fourier method for nonsmooth initial data. *Math. Comput.* **32** (1978) 1041.
- [69] Matthaeus W.H. & Montgomery D. Selective decay hypothesis at high mechanical and magnetic Reynolds numbers. *Ann. (N.Y.) Acad. Sci.* **357** (1980) 203.
- [70] Matthaeus W.H., Stribling W.T., Martinez D. & Oughton S. Selective decay and coherent vortices in two-dimensional incompressible turbulence. *Phys. Rev. Lett.* **66** (1991) 2731.
- [71] Miller J. Statistical mechanics of Euler's equation in two dimensions. *Phys. Rev. Lett.* **65** (1990) 2137.
- [72] Molenaar D., Clercx H.J.H. & van Heijst G.J.F. Angular momentum of forced 2D turbulence in a square no-slip domain. *Physica D* **196** (2004) 329.
- [73] Montgomery D. vol. 250 of *Lecture Notes in Pure and Applied Mathematics*, chap. 5. Chapman & Hall/CRC, New York (2006).
- [74] Montgomery D., Matthaeus W.H., Stribling W.T., Martinez D. & Oughton S. Relaxation in two dimensions and the "sinh-Poisson" equation. *Phys. Fluids A* **4** (1992) 3.
- [75] Montgomery D., Shan X. & Matthaeus W.H. Navier-Stokes relaxation to sinh-Poisson states at finite Reynolds numbers. *Phys. Fluids A* **5** (1993) 2207.
- [76] Morton B.R. The generation and decay of vorticity. *Geophys. Astrophys. Fluid Dyn.* **28** (1984) 277.
- [77] Nam K., Ott E., Antonsen T.M. & Guzdar P.N. Lagrangian chaos and the effect of drag on the enstrophy cascade. *Phys. Rev. Lett.* **84** (2000) 5134.
- [78] Obabko A.V. & Cassel K.V. Navier-Stokes solutions of unsteady separation induced by a vortex. *J. Fluid Mech.* **465** (2002) 99.
- [79] Onsager L. Statistical hydrodynamics. *Nuovo Cimento Suppl* **6** (1949) 279.
- [80] Orlandi P. Vortex dipole rebound from a wall. *Phys. Fluids A* **2** (1990) 1429.
- [81] Orszag S.A. Numerical methods for the simulation of turbulence. *Phys. Fluids, Suppl. II* **12** (1969) 250.

- [82] Ould-Salihi M.L., Cottet G.H. & El Hamraoui M. Blending finite-difference and vortex methods for incompressible flow computations. *J. Sci. Comput.* **22** (2000) 1655.
- [83] Paccou A., Chiavassa G., Liandrat J. & Schneider K. A penalisation method applied to the wave equation. *C. R. Mécanique* **333** (2005) 79.
- [84] Paret J. & Tabeling P. Intermittency in the two-dimensional inverse cascade of energy: Experimental observations. *Phys. Fluids* **10** (1998) 3126.
- [85] Peridier V.J., Smith F.T. & Walker J.D.A. Vortex-induced boundary layer separation. Part 1. The unsteady limit problem $Re \rightarrow \infty$. *J. Fluid. Mech.* **232** (1991) 99.
- [86] Peridier V.J., Smith F.T. & Walker J.D.A. Vortex-induced boundary layer separation. Part 2. Unsteady interacting boundary-layer theory. *J. Fluid. Mech.* **232** (1991) 133.
- [87] Pointin Y.B. & Lundgren T.S. *Phys. Fluids* **19** (1976) 1459.
- [88] Pope S. *Turbulent Flows*. Cambridge University Press (2000).
- [89] Robert R. & Sommeria J. Statistical equilibrium states for two-dimensional flows. *J. Fluid. Mech.* **229** (1991) 291.
- [90] Rutgers M.A. Forced 2D turbulence: Experimental evidence of simultaneous inverse energy and forward enstrophy cascades. *Phys. Rev. Lett.* **81** (1998) 2244.
- [91] Sarid E., Teodorescu C., Marcus P.S. & Fajans J. Breaking of rotational symmetry in cylindrically bounded 2D electron plasmas and 2D fluids. *Phys. Rev. Lett.* **93** (2004) 215002.
- [92] Schneider K. Numerical simulation of the transient flow behaviour in chemical reactors using a penalisation method. *Comp. Fluids* **34** (2005) 1223.
- [93] Schneider K. & Farge M. Numerical simulation of a mixing layer in an adaptive wavelet basis. *C. R. Acad. Sci. Paris Série II b* **328** (2000) 263.
- [94] Schneider K. & Farge M. Adaptive wavelet simulation of a flow around an impulsively started cylinder using penalisation. *Appl. Comput. Harmon. A.* **12** (2002) 374.
- [95] Schneider K. & Farge M. Coherent vortex simulation (CVS) of dipole-wall interaction using volume penalisation. In *Advances in Turbulence X, Proc. of the Tenth European Turbulence Conference*, page 621 (2004).
- [96] Schneider K. & Farge M. Decaying two-dimensional turbulence in a circular container. *Phys. Rev. Lett.* **95** (2005) 244502.

- [97] Schneider K., Farge M. & Kevlahan N. Spatial intermittency in two-dimensional turbulence: a wavelet approach. In N. Tongring & R.C. Penner, eds., *Perspectives in Mathematics and Physics*, vol. 34 of *World Scientific*, page 302 (2003).
- [98] Schneider K., Farge M., Pellegrino G. & Rogers M. Coherent vortex simulation of three-dimensional turbulent mixing layers using orthogonal wavelets. *J. Fluid Mech.* **534** (2005) 39.
- [99] Shu C.W. & Wong P. A note on the accuracy of spectral methods applied to nonlinear conservation laws. *J. Sci. Comput.* **10** (1995) 357.
- [100] Smith L. & Yakhot V. Bose condensation and small-scale structure generation in a random force driven 2D turbulence. *Phys. Rev. Lett.* **71** (1993) 352.
- [101] Smith L. & Yakhot V. Finite-size effects in two-dimensional turbulence. *J. Fluid. Mech.* **274** (1994) 115.
- [102] Sommeria J. Experimental study of the two-dimensional inverse energy cascade in a square box. *J. Fluid. Mech.* **170** (1986) 139.
- [103] Tabeling P., Burkhardt S., Cardoso O. & Willaime H. Experimental-study of freely decaying two-dimensional turbulence. *Phys. Rev. Lett.* **67** (1991) 3772.
- [104] Tadmor E. & Tanner J. Adaptive mollifiers for high resolution recovery of piecewise smooth data from its spectral information. *Found. Comput. Math.* **2** (2002) 155.
- [105] Tran C.V. & Dritschel D.G. Vanishing enstrophy dissipation in two-dimensional Navier-Stokes turbulence in the inviscid limit. *J. Fluid Mech* **559** (2006) 107.
- [106] Wells M.G., Clercx H.J.H. & van Heijst G.J.F. Vortices in oscillating spin-up. *J. Fluid Mech.* **573** (2007) 339.
- [107] Yin Z., Clercx H.J.H. & Montgomery D.C. On an easily implemented parallel scheme for a 2D Fourier pseudospectral algorithm. *Comp. Fluids* **33** (2004) 509.

Summary

Fourier spectral computation of geometrically confined two-dimensional flows

Large-scale flow phenomena in the atmosphere and the oceans are predominantly two-dimensional (2D) due to the large aspect ratio of the typical horizontal and vertical length scales in the flow. The 2D nature of large-scale geophysical flows motivates the use of a conceptual approach known as "2D turbulence". It usually involves the (forced/damped) Navier-Stokes equations on a square domain with periodic boundaries or on a spherical surface. This setup may be useful for numerical studies of atmospheric flow. For the oceans, on the other hand, geometrical confinement due to the continental shelves is of crucial importance. The physically most relevant boundary condition for oceanographic flow is probably the no-slip condition. Previous numerical and experimental studies have shown that confinement by no-slip boundaries dramatically affects the dynamics of (quasi-)2D turbulence due to its role as vorticity source. An important process is the detachment of high-amplitude vorticity filaments from the no-slip sidewalls that subsequently affect the internal flow.

The first part of the thesis concerns the development and extensive testing of a Fourier spectral scheme for 2D Navier-Stokes flow in domains bounded by rigid no-slip walls. An advantage of Fourier methods is that higher-order accuracy can, in principle, be achieved. Moreover, these methods are fast, relatively easy to implement even for performing parallel computations. The no-slip boundary condition is enforced by using an immersed boundary technique called "volume-penalization". In this method an obstacle with no-slip boundaries is modelled as a porous medium with a small permeability. It has recently been shown that in the limit of infinitely small permeability the solution of the penalized Navier-Stokes equations converges towards the solution of the Navier-Stokes equations with no-slip boundaries. Therefore the penalization error can be controlled with an arbitrary parameter. A possible drawback is that the sharp transition between the fluid and the porous medium can trigger Gibbs oscillations that might deteriorate the stability and accuracy of the scheme. Using a very challenging dipole-wall collision as a benchmark problem, it is, however, shown that higher-order accuracy is retrieved by using a novel

post-processing procedure to remove the Gibbs effect.

The second topic of the thesis is the dynamics of geometrically confined 2D turbulent flows. The role of the geometry on the flow development has been studied extensively. For this purpose high resolution Fourier spectral simulations have been conducted where different geometries are implemented by using the volume-penalization method. A quantity that is of particular importance on a bounded domain is the angular momentum. On a circular domain production of angular momentum is virtually absent. Therefore the amount of angular momentum carried by the initial flow has important consequences for the evolution of the flow. The results of the simulations are consistent with previous numerical and experimental work on this topic performed in a lower Reynolds number regime. The typical vortex structures of the late time evolution of the flow are explained by means of a minimum enstrophy principle and the presence of weak viscous dissipation. For an elliptic geometry it is shown that strong spin-up events of the flow occur even for small eccentricities. The spin-up phenomenon can be related to the role of the pressure along the boundary of the domain. It is found that the magnitude of the torque exerted on the internal fluid can be scaled with the eccentricity. Furthermore, it is observed that angular momentum production in a non circular geometry is not restricted to moderate Reynolds numbers. Significantly higher Reynolds number flow computations in a square geometry clearly reveal strong and rapid spin-up of the flow.

Finally the scale-dependence of the vorticity and velocity statistics in forced 2D turbulence on a bounded domain has been studied. A challenging aspect is that a statistically steady state can be achieved by a balance between the injection of kinetic energy by the external forcing and energy dissipation at the no-slip sidewalls. It is important to note that on a double periodic domain a steady state is usually achieved by introducing volumetric drag forces. Several studies reported that this strongly affects the spatial scaling behaviour of the flow. Therefore it is very interesting to quantify the small-scale statistics in the bulk of statistically steady flow on a domain with no-slip boundaries in the absence of bottom drag. It is observed that the internal flow shows extended self-similar, locally homogeneous and isotropic scaling behaviour at small scales. It is further demonstrated that a direct enstrophy cascade develops in the interior of the flow domain. Some deviations from the classical scaling theory of 2D turbulence developed independently by Kraichnan, Batchelor and Leith may be associated to the presence of coherent structures in the flow. It is, however, anticipated that higher-resolution simulations are required in order to draw more decisive conclusions. The parallel Fourier spectral scheme with volume-penalization is very suitable for pursuing such simulations on high performance machines in the near future.

In summary the thesis contributes to both the development of numerical techniques and understanding of wall-bounded two-dimensional flows. The Fourier

spectral scheme with volume-penalization is found very suitable for pursuing direct numerical simulations in complex geometries. The high-resolution simulations considered in the thesis clearly reveal that spontaneous production of angular momentum due to interaction with non-circular domain boundaries is present for significantly higher Reynolds numbers than considered previously.

Dankwoord

Allereerst wil ik mijn vrouw Sandra bedanken voor haar steun gedurende het promotie onderzoek. Met name de laatste fase van de afronding waarin wij tevens in verwachting waren van onze zoon Cas is ook voor haar zwaar geweest.

Dit werk is totstand gekomen in nauwe samenwerking met mijn promotoren Herman Clercx en GertJan van Heijst. Bij iedere bespreking waren zij erg enthousiast over mijn resultaten en stelden dan steevast de vraag: wanneer kunnen we het artikel verwachten? Ik wil hen hartelijk bedanken voor hun aanmoediging. Mijn dank gaat ook uit naar de andere leden van de commissie: Kai Schneider, Bob Mattheij, Gijs Ooms, Klaas Kopinga, Jaap van der Vegt en Anton Darhuber.

Mijn paranimfen Marleen van Aartrijk en Werner Kramer hebben altijd voor mij klaar gestaan. Ze hebben me namelijk geholpen bij vele technische en wetenschappelijke problemen. Het is daarom een logische keuze om Marleen en Werner te vragen om mij bij te staan tijdens de openbare verdediging. Laurens van Bokhoven wil ik graag bedanken voor zijn steun tijdens het onderzoek en de avontuurlijke “bergwandelingen” .

Graag wil ik Kai Schneider en Umberto D’Ortona bedanken voor de langdurige samenwerking. Ik heb enorm genoten van de verschillende werkbezoeken aan Marseille en niet alleen vanwege de Bouillabaisse en de mooie duiklocaties.

Marjan Rodenburg wil ik hartelijk bedanken voor de vele help-me-uit-de-brand-diensten die ze verleend heeft. Zelfs in het weekend stond ze voor mij klaar om bijvoorbeeld een betalingsprobleem te verhelpen tijdens een conferentie in de VS. Met Ruben Trieling, Jan Lodewijks en Leon Kamp heb ik diverse werkcolleges verzorgd. Ik vond dit erg leerzaam en buitengewoon leuk om dit met hen te doen.

Verder wil ik de overige leden van het secretariaat, de (voormalige) technische en wetenschappelijke staf, promovendi, postdocs en studenten bedanken voor hun bijdrage aan de goede sfeer in de groep. Ik wil van het dankwoord geen namenspel maken, maar ik wil toch graag noemen: Ad voor het oplossen van hardnekkige computer problemen, Petra voor de gezellige theepauzes en Bert, Jort en Mar-

lies vanwege hun initiatief om het dispuut “Alles Stroomt” weer nieuw leven in te blazen. Verder wil ik iedereen bedanken voor de gezellige koffiepauzes bij “Het Ei”.

Van mijn familie en vrienden heb ik hun onvoorwaardelijke steun gehad op een aantal moeilijke momenten in de periode waarin het onderzoek heeft plaatsgevonden. Mijn proefschrift wil ik opdragen aan mijn grootouders die mij ook altijd deze steun hebben gegeven, maar dat vandaag helaas niet meer kunnen doen. Ze hebben erg veel voor mij betekend.

Curriculum Vitae

June 3, 1977

Born in Waalwijk, The Netherlands.

1990–1997

Dr Mollercollege, Waalwijk.

1997–2003

MSc Meteorology, *cum laude*,
Wageningen University.

Graduation project,
Vortex Dynamics and Turbulence,
Department of Applied Physics,
Eindhoven University of Technology.

2003–2008

PhD candidate,
Vortex Dynamics and Turbulence,
Department of Applied Physics,
Eindhoven University of Technology.

Central Works Council (2005-2006),
Dutch Foundation for Fundamental Research on Matter.

